2011-12

Using x-ray diffraction to assess residual stresses in laser peened and welded aluminum

Banazwski, Brian J.

Monterey, California. Naval Postgraduate School

NAVAL POSTGRADUATE SCHOOL

MONTEREY, CALIFORNIA

THESIS

USING X-RAY DIFFRACTION TO ASSESS RESIDUAL STRESSES IN LASER PEENED AND WELDED ALUMINUM

by

Brian J. Banazwski

December 2011

Thesis Advisor:	Luke N. Brewer
Second Reader:	Sarath K. Menon

Approved for public release; distribution is unlimited

THIS PAGE INTENTIONALLY LEFT BLANK

REPORT DOCUMENTATION PAGE			Form Approved OMB No. 0704-0188
Public reporting burden for this collection of information is estimated to average 1 hour per response, including the time for reviewing instruction, searching existing data sources, gathering and maintaining the data needed, and completing and reviewing the collection of information. Send comments regarding this burden estimate or any other aspect of this collection of information, including suggestions for reducing this burden, to Washington headquarters Services, Directorate for Information Operations and Reports, 1215 Jefferson Davis Highway, Suite 1204, Arlington, VA 22202-4302, and to the Office of Management and Budget, Paperwork Reduction Project (0704-0188) Washington DC 20503.			
1. AGENCY USE ONLY ***(Leave blank)***	**2. REPORT DATE** December 2011	**3. REPORT TYPE AND DATES COVERED** Master's Thesis	
4. TITLE AND SUBTITLE Using X-ray Diffraction to Assess Residual Stresses in Laser Peened and Welded Aluminum		**5. FUNDING NUMBERS**	
6. AUTHOR(S) Brian J. Banazwski			
7. PERFORMING ORGANIZATION NAME(S) AND ADDRESS(ES) Naval Postgraduate School Monterey, CA 93943-5000		**8. PERFORMING ORGANIZATION REPORT NUMBER**	
9. SPONSORING /MONITORING AGENCY NAME(S) AND ADDRESS(ES) N/A		**10. SPONSORING/MONITORING AGENCY REPORT NUMBER**	
11. SUPPLEMENTARY NOTES The views expressed in this thesis are those of the author and do not reflect the official policy or position of the Department of Defense or the U.S. Government. IRB Protocol number _____N/A_____.			
12a. DISTRIBUTION / AVAILABILITY STATEMENT Approved for public release; distribution is unlimited		**12b. DISTRIBUTION CODE** A	

13. ABSTRACT (maximum 200 words)

This thesis examines the interplay of residual stress distributions caused by welding and laser peening of marine aluminum alloy 5083. Residual stresses at welds in this alloy can cause fatigue and stress corrosion cracking in ship superstructures. X-ray diffraction was used to measure the residual stress distributions across welded and laser peened areas of welded aluminum plate. Full strain and stress tensors were measured and calculated in order to develop a fuller picture of the residual stress distribution in this complex geometry. Electropolishing was used to take residual stresses from specified depth below the surface. The tensor analysis was found to be extremely sensitive to the exact choice of diffraction angles used in the experiment, and an algorithm was developed to optimize the design of the diffraction experiment. Bi-axial stress analysis did show an increase in compressive stress from the laser peening after a couple tenths of a millimeter followed by a gradual decrease in compressive stress as depth increases.

14. SUBJECT TERMS X-ray Diffraction, Residual Stresses, Laser Peening, AA5083			**15. NUMBER OF PAGES** 109
			16. PRICE CODE
17. SECURITY CLASSIFICATION OF REPORT Unclassified	**18. SECURITY CLASSIFICATION OF THIS PAGE** Unclassified	**19. SECURITY CLASSIFICATION OF ABSTRACT** Unclassified	**20. LIMITATION OF ABSTRACT** UU

NSN 7540-01-280-5500 Standard Form 298 (Rev. 2-89)
Prescribed by ANSI Std. 239-18

THIS PAGE INTENTIONALLY LEFT BLANK

Approved for public release; distribution is unlimited

USING X-RAY DIFFRACTION TO ASSESS RESIDUAL STRESSES IN LASER PEENED AND WELDED ALUMINUM

Brian J. Banazwski
Lieutenant, United States Navy
B.S., Rochester Institute of Technology, 2004

Submitted in partial fulfillment of the
requirements for the degree of

MASTER OF SCIENCE IN MECHANICAL ENGINEERING

from the

NAVAL POSTGRADUATE SCHOOL
December 2011

Author: Brian J. Banazwski

Approved by: Luke N. Brewer
Thesis Advisor

Sarath K. Menon
Second Reader

Knox Millsaps
Chair, Department of Mechanical and Aerospace Engineering

THIS PAGE INTENTIONALLY LEFT BLANK

ABSTRACT

This thesis examines the interplay of residual stress distributions caused by welding and laser peening of marine aluminum alloy 5083. Residual stresses at welds in this alloy can cause fatigue and stress corrosion cracking in ship superstructures. X-ray diffraction was used to measure the residual stress distributions across welded and laser peened areas of welded aluminum plate. Full strain and stress tensors were measured and calculated in order to develop a fuller picture of the residual stress distribution in this complex geometry. Electropolishing was used to take residual stresses from specified depth below the surface. The tensor analysis was found to be extremely sensitive to the exact choice of diffraction angles used in the experiment, and an algorithm was developed to optimize the design of the diffraction experiment. Bi-axial stress analysis did show an increase in compressive stress from the laser peening after a couple tenths of a millimeter followed by a gradual decrease in compressive stress as depth increases.

THIS PAGE INTENTIONALLY LEFT BLANK

TABLE OF CONTENTS

I. INTRODUCTION AND BACKGROUND 1
A. MOTIVATION 1
1. Causes and Control of Residual Stresses 6
B. INTRODUCTION 10
1. Reduction of Residual Stresses from Peening Processes 10
C. METHODS FOR MEASURING RESIDUAL STRESS 15
1. Laboratory X-ray Diffraction 16
a. General Background 16
b. "d vs. $\sin^2\psi$" Technique 24
D. THESIS OBJECTIVES 26

II. EXPERIMENTAL PROCEDURE 27
A. MATERIAL PROCESSING 27
1. Plate Fabrication 27
2. Welding 27
B. LASER PEENING 29
1. Process 29
C. ELECTRO-POLISHING 31
1. Process 31
D. X-RAY DIFFRACTION 34
1. X-ray Diffraction Equipment Overview 34
2. Specimen Set-up and Orientation 35
3. X-ray Tube Selection 36
4. Reflection Selection 37
5. ψ Angle Selection 38
6. Additional XRD Set-up Parameters 41
E. EXPERIMENTAL MEASUREMENTS 42
1. "d vs. $\sin^2\psi$" Stress Measurement Process 42
2. Tensor Measurement Process 45

III. RESULTS AND DISCUSSION 47
A. CALIBRATION RESULTS FOR "d vs. $\sin^2\psi$" ANALYSIS 47
B. RESIDUAL STRESSES USING "d vs. $\sin^2\psi$" ANALYSIS 50
1. Control Weld Results 50
2. Residual Stress Distribution after Laser Peening 55
3. Accounting for Crystallographic Texture 64
C. RESIDUAL STRESS TENSOR MEASUREMENTS 66
1. High Stress Standard Tensor Results 66
2. Control and Laser Peened Tensor Results 70
D. FUTURE WORK 71

IV. CONCLUSIONS 73

LIST OF REFERENCES 75

APPENDIX **79**
INITIAL DISTRIBUTION LIST **89**

LIST OF FIGURES

Figure 1. Comparison of fuel, range, and speed with a 15% reduction in weight. Note that all three axises have the same 2% interval.(From [1])....1
Figure 2. Schematic showing how cracking occurs in sensitized material.(From [1]) 2
Figure 3. Venn diagram showing the mutual importance of sensitization, corrosive environment, and a tensile stress. 3
Figure 4. Cracks in the deck-plate from IGSCC mechanism.(From [2]) 4
Figure 5. Stress amplitude (S) verses logarithm of the number of cycles to fatigue failure (N) for a material that does not have fatigue limit.(From [6]) 5
Figure 6. Typical distributions of (a) longitudinal, σ_x, and (b) transverse, σ_y, residual stresses in butt welds.(From [9]) 7
Figure 7. Measured and calculated residual stresses in butt weld of AA5083.(From [9]) 8
Figure 8. (a) Comparison between longitudinal stresses in AA5083-H321 MIG weld at depths of 1, 4, and 7mm (b) Comparison between transverse stresses in AA5083-H321 MIG weld at depths of 1, 4, and 7mm.(From [10]) 9
Figure 9. SN-curve and fatigue limits for AA5083 with a stress ratio of 0.1 of welded and un-welded samples tested in air and in seawater.(From [11]) 10
Figure 10. An S-N curve comparing the fatigue limit increases of 7075-T7351 aluminum alloy from shot peening and laser peening.(From [12]) 11
Figure 11. Residual stress distribution prior to and after the *Esonix* UIT on lightly (AFL-2), moderately (BFM-3), and severly (AFS-6) exfoliated 7075-T6511 specimens.(From [14]) 12
Figure 12. Illustration of the laser peening process.(From [17]) 13
Figure 13. Fatigue crack growth rates for friction stir welded AA2195 at a stress ratio, R, of 0.1 for various peening conditions.(From [17]) 14
Figure 14. Principle of diffraction based on the relationship between λ, the diffracted beam angle, 2θ, and d' gives rise to Bragg's law, $n\lambda=2d'\sin\theta$.(From [20]) 18
Figure 15. Description of the Bragg angle in regards to the principles behind x-ray diffraction stress measurements. (a) $\psi=0$. (b) $\psi=\psi$ (sample rotated at a known ψ angle).(From [19]) 20
Figure 16. Diffraction peaks from 5083 aluminum alloy showing how the 2θ values shift based on different elastic strains. Here the peak centroid of $\psi=1$ degrees is shifted to the left of the other two peaks at $\psi=\pm45$ degrees. 20
Figure 17. Relationship of the laboratory coordinate system L_i, specimen coordinate system S_i, and ϕ,ψ angles.(From [21]) 21
Figure 18. Three basic types of d vs. $\sin^2\psi$ plots commonly encountered in residual stress analysis. (a) "regular," linear behavior, (b) branched behavior, and (c) oscillatory behavior.(From [21]) 25
Figure 19. Welded Plate (a) side view (b) top face (c) bottom face (weld root).(From [1]) 28
Figure 20. Typical laser peened specimen. Provided by MIC. 30

Figure 21. Laser peeing process layout: Group 1 in the middle along the weld nugget, Group 2 on the left side of the weld starting at the toe of the weld, and Group 3 on the right side of the weld starting at the toe of the weld. Provided by MIC.....31
Figure 22. Proto Electrolytic Polisher Model 8818.....32
Figure 23. This picture shows the location and the size of electro-polishing done in this work. This is Specimen 3-27-2 after electro-polishing to a depth of 508μm (20mil) on the bottom side of the weld line. 33
Figure 24. Mitutoyo height gauge measuring the depth of how much material was removed during an electro-polish on specimen 3-27-2.....34
Figure 25. LXRD model used in this work with Specimen 3-27-2 being measured. 35
Figure 26. Specimen orientation with respect to the XRD goniometer. ϕ=0 degrees is when the goniometer axis of the XRD goniometer is parallel to the x-axis of the specimen. Positive ϕ and ψ rotations are in the counterclockwise direction about the z-axis and goniometer axis, respectively. 36
Figure 27. Absorption of x-rays as a function of depth for common x-ray tube types. 37
Figure 28. Specimen and detector layout used for determining β, ψ_1, and ψ_2 angles, and for visualizing how the different lattice planes of the specimen are being measured. 39
Figure 29. d vs. $\sin^2\psi$ plot of specimen 3-27-2 at 25mm distance from the weld toe at ϕ=0 degrees for the {331} reflection highlighting how the combination of detector values are plotted. 41
Figure 30. Locations of experimental test points on the one inch control, 1-18-1, and 3-27-2 specimens. 45
Figure 31. Average of five measurements on the high stress standard results for data set #2. Error bars represent ± one standard deviation. 48
Figure 32. Transverse residual stresses as a function of distance from the weld toe in the control specimen at the surface. 51
Figure 33. Longitudinal residual stresses as a function of distance from the weld toe in the control specimen at the surface. 52
Figure 34. Transverse residual stresses as a function of depth in the control specimen at the 6mm test point. 53
Figure 35. Longitudinal residual stresses as a function of depth in the control specimen at the 6mm test point. 54
Figure 36. Transverse residual stresses as a function of depth in the control specimen at the 25mm test point. 54
Figure 37. Longitudinal residual stresses as a function of depth in the control specimen at the 25mm test point. 55
Figure 38. Transverse residual stresses as a function of distance from the weld toe in the 1-18-1 and 3-27-2 specimens at the surface. 56
Figure 39. Longitudinal residual stresses as a function of distance from the weld toe in the 1-18-1 and 3-27-2 specimens at the surface. 57
Figure 40. Residual stresses for comparing no peening to shot peening and to laser peening in both the transverse and longitudinal directions from the weld centerline at the surface.(From [32]) 58

Figure 41. Transverse residual stresses as a function of depth in the 1-18-1 and 3-27-2 specimens at the 6mm test point. 59
Figure 42. Longitudinal residual stresses as a function of depth in the 1-18-1 and 3-27-2 specimens at the 6mm test point. 60
Figure 43. Transverse residual stresses as a function of depth in the 1-18-1 and 3-27-2 specimens at the 25mm test point. 61
Figure 44. Longitudinal residual stresses as a function of depth in the 1-18-1 and 3-27-2 specimens at the 25mm test point. 62
Figure 45. A plot of the FWHM at a depth of 0.0254mm. The upper plot is for the transverse direction at ϕ=0 degrees and the lower plot is for the longitudinal direction at ϕ=90 degrees....63
Figure 46. Pole figures generated by electron backscattered diffraction for AA5083 plate material. 64
Figure 47. Example of the oscillatory nature of the data across the measured specimens at ϕ=0 degrees and at a depth of 0.254mm. 66
Figure 48. This is an example of the screenshot of the peak fitting constants used for experimental and calibration measurements per this work. Provided by MIC. 82
Figure 49. This is an example of a screenshot of the β and ϕ angles used for experimental measurements. Provided by MIC. 83

THIS PAGE INTENTIONALLY LEFT BLANK

LIST OF TABLES

Table 1. Relationship between 2θ angles and their associated reflection planes aluminum. The n/a in the table means that the corresponding 2θ angle for that reflection for that radiation wavelength is beyond 180 degrees. 17

Table 2. Weld procedure from Carderock Division, Naval Surface Warfare Center (CDNSWC).(From [1]).....29

Table 3. Laser peening conditions for experimental specimens. Provided by MIC. 30

Table 4. Electro-polishing times to achieve a certain depth. 31

Table 5. Typical experimental β and ψ angles for detector 1 and detector 2 for the {331} reflection used for the collection of residual strain data. The highlighted rows from each detector were combined together to form the data point along the x-axis on a single d vs. $\sin^2\psi$ plot, see Figure 29.....40

Table 6. β and ψ angles of detector 1 and detector 2 used for calibrating the XRD with the high and low stress standards.....44

Table 7. ψ and ϕ angles used for tensor data sets one and two.....46

Table 8. Calibration data for the low and high stress standards for data sets #2, #3, and #4.....49

Table 9. Strain and stress tensor results for the high stress standard where (a) has an extremely high condition number resulting in implausible stresses, (b) has a much better (i.e. lower) condition number, but a non bi-axial stress, and (c) has an even lower condition number and a revised d_0 value resulting in a more believable bi-axial stress. 69

Table 10. Strain and stress tensor results for 1-18-1 at 6mm test point z=0.254mm.....71

Table 11. Relationship of β to ψ angles for detector 1 and detector 2 for the {331} reflection using a cobalt tube. 80

Table 12. Relationship of ψ to β angles for detector 1 and detector 2 for the {331} reflection using a cobalt tube. 81

Table 13. β and ψ angles of detector 1 and detector 2 used for data set one. 84

Table 14. β and ψ angles of detector 1 and detector 2 used for data set two.....85

Table 15. β and ψ angles of detector 1 and detector 2 used for data sets three and four. 86

Table 16. Results of measured stresses transverse to the weld centerline at ϕ=0 degrees for various test locations and at various depths of (a) surface, (b) 0.0254mm, (c) 0.254mm, and (d) 0.508mm. 87

Table 17. Results of measured stresses longitudinal to the weld centerline at ϕ=90 degrees for various test locations and at various depths of (a) surface, (b) 0.0254mm, (c) 0.254mm, and (d) 0.508mm. 88

THIS PAGE INTENTIONALLY LEFT BLANK

LIST OF ACRONYMS AND ABBREVIATIONS

SCC	Stress Corrosion Cracking
LP	Laser Peening
AA5083	Aluminum Alloy 5083 H116
MIG	Metal Inert Gas Welding
MIC	Metal Improvement Company
IGC	Intergranular Corrosion
IGSCC	Intergranular Stress Corrosion Cracking
HAZ	Heat-Affected Zone
UIT	Ultrasonic Impact Technique
XRD	X-ray Diffraction
FWHM	Full Width at Half Maximum

THIS PAGE INTENTIONALLY LEFT BLANK

ACKNOWLEDGMENTS

I would like to thank Professor Brewer for his endless, positive council and outlook when things did not make sense. I have learned a lot about x-ray diffraction and about myself through his tutelage. NPS is extremely blessed to have him and for all that he does for the Mechanical Engineering Department and for his students. I am confident that he will make us all better officers.

Professor Menon was a constant source for materials knowledge. His classes and labs paved the way for getting through this thesis, and for that I say thank you.

My thesis could not have been accomplished without the generous support of Dr. L. Hackel from Metal Improvement Company in Livermore, CA and the use of his laboratory equipment. Lab technicians Serena Marley and Tracy Heidenberger provided endless help and technical knowledge in collecting data used in this thesis. I thank the both of them for all their hard work and long hours.

I would like to thank all the professors and staff at NPS who furthered my academic knowledge and personal growth during my classes and thesis work.

Finally, to my wife, Michelle, who I am forever grateful for. Her support, encouragement, and understanding helped me through all the countless hours and mental exhaustion spent on this thesis. I could not have done this without her.

THIS PAGE INTENTIONALLY LEFT BLANK

I. INTRODUCTION AND BACKGROUND

A. MOTIVATION

Recent trends in shipbuilding have been focused on reducing the overall weight of the ship to increase fuel economy because of higher fuel prices. One way to do this is to use lightweight materials such as aluminum in the construction of the superstructure or even the whole ship, as is the case with the new Littoral Combat Ships (LCS). Aluminum is about one-third the density of steel, and possesses good general corrosion resistance. These attributes allow ships to go faster, travel farther, and carry larger payloads given the same amount of fuel load. Mattern estimates that if a ship's weight were reduced by 15%, its fuel consumption would decrease by 10%, its range given the same amount of fuel would increase by 11.4%, and its speed would also increase by 5.6% (Figure 1).[1]

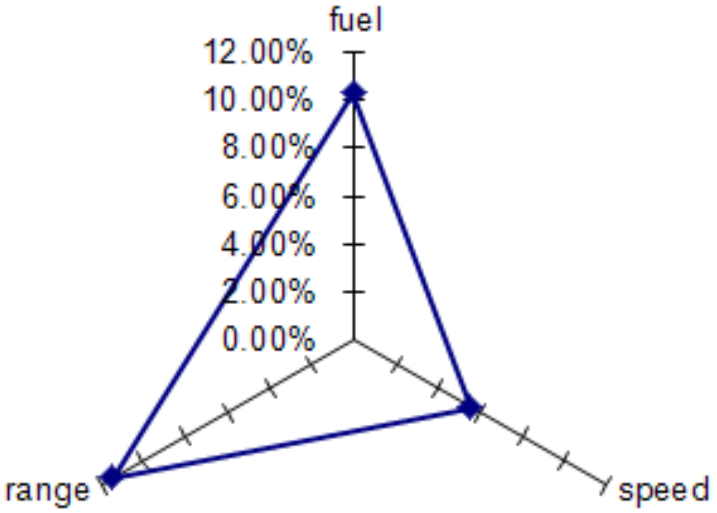

Figure 1. Comparison of fuel, range, and speed with a 15% reduction in weight. Note that all three axises have the same 2% interval.(From [1])

Despite these benefits based on weight savings, aluminum alloys can show a great vulnerability to stress corrosion cracking (SCC) and intergranular corrosion (IGC) when placed in a marine environment. This problem goes against the rationale for choosing a 5xxx series aluminum alloy because it is supposed to be one of the more resistant

aluminum alloys to SCC.[2] The reason for this vulnerability to SCC is because of the alloy's high magnesium (Mg) content, which is used as a solid-solution strengthening element. Typical 5xxx series aluminum alloys used in marine construction have between 4.5 (AA5083) and 5.7 (AA5456) wt% Mg.[2] When the aluminum alloy is exposed to temperatures above 50°C for a prolonged period of time, the magnesium comes out of solid solution and forms □ precipitates (Al_3Mg_2) along the grain boundaries. This process is known as sensitization and is responsible for intergranular corrosion. Any aluminum alloy with magnesium content greater than 3wt% is potentially susceptible to SCC and IGC when exposed to temperatures greater than 50°C over long time periods.[3] Figure 2 illustrates the sensitization process and the intergranular SCC (IGSCC) that follows when a tensile stress is applied after sensitization.[1]

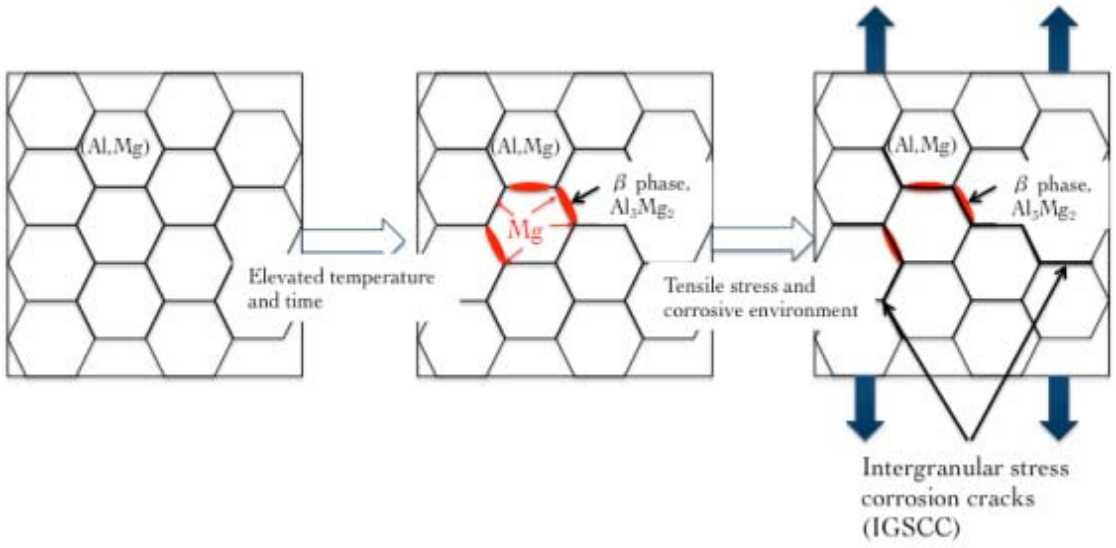

Figure 2. Schematic showing how cracking occurs in sensitized material.(From [1])

There are three conditions that need to occur simultaneously for SCC to take place: 1) a susceptible metallurgy; 2) a corrosive environment; and 3) a tensile stress as shown in Figure 3. If any one of the three conditions is removed, then SCC will not occur. Obviously, the corrosive environment cannot be eliminated from the scope of the working environment of aluminum ships. Once the aluminum alloy 5083 is sensitized, it can be difficult or even impossible to mitigate IGSCC. Controlling the stress state is a more realistic option for SCC control in existing ship structures. The goal is to reduce

tensile stress from areas with sensitized material. Tensile stresses arise from two main sources: applied stresses and residual stresses. Applied stresses come from a number of sources including the hogging and sagging because of the ship's motion through the water. Additional applied stresses from the waves and wind coupled with the ship's machinery and payload create a state of dynamic compressive and tensile stresses. Sources of residual stress include welds, rivets, and bolts.[1,2]

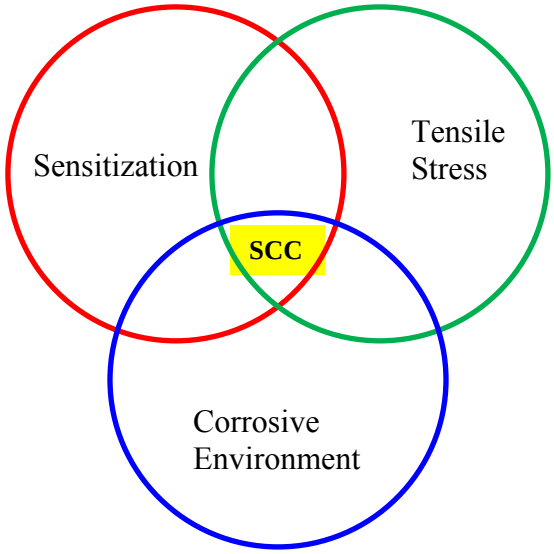

Figure 3. Venn diagram showing the mutual importance of sensitization, corrosive environment, and a tensile stress.

This issue of inter-granular stress corrosion cracking has been observed in both commercial and military vessels. Between 2001 and 2002 over 400 commercial vessels constructed of aluminum alloy 5083-H321 began to experience severe pitting and extensive SCC making the vessels unfit for traveling at sea.[4] The Navy is also experiencing SCC in the aluminum superstructure onboard its Ticonderoga class cruisers (CG-47) where cracks up to multiple feet long have been reported.[2] Cracks have appeared in unusually low stress areas, such as deck plating and bulkheads, where no stress concentrations were present, see Figure 4.[2] Fourteen million dollars were spent to repair SCC-related issues on the USS PORT ROYAL alone, and across the CG-47 class there have been over 3,000 reported cracks on aluminum superstructures.[2,5]

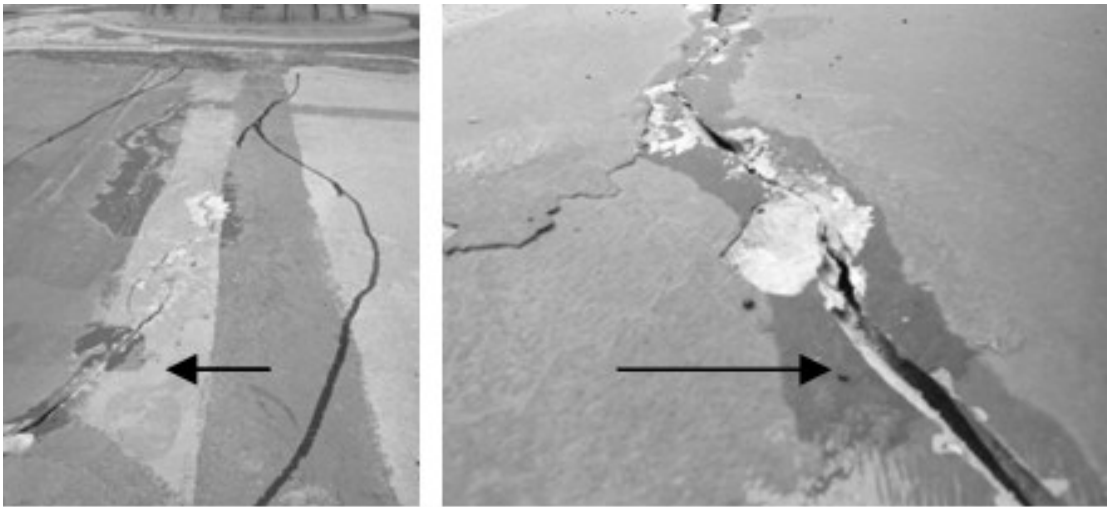

Figure 4. Cracks in the deck-plate from IGSCC mechanism.(From [2])

While many of the cracks in aluminum ship structures are caused by stress corrosion cracking, fatigue loading drives the majority of cracks observed in aluminum ship structures. Fatigue is characterized as the failure of a material after being subjected to cyclic loading. Failure occurs at stress levels much below the ultimate or yield strength of the material and is the single most common cause of failures in metals at around 90% of all failures.[6] Crack nucleation almost always initiates at stress concentration points like surface scratches, notches, sharp fillets, and weld toes.[6] The repeated nature of the hogging and sagging of the ship at sea and the effects of the residual stresses from welding create a favorable environment for fatigue to initiate and propagate a crack.

The prevalence of fatigue cracks is particularly common in aluminum, as most aluminum alloys do not have a clear fatigue endurance limit, or threshold. The fatigue endurance limit is the amount of stress that can be repeatedly applied to a metal, typically beyond 10 million cycles, below which no cracking will occur. Figure 5 shows that for aluminum alloys, the stress required for failure continues to decrease as the number of cycles increases, but there is no stress below which the material clearly will not fail.[6]

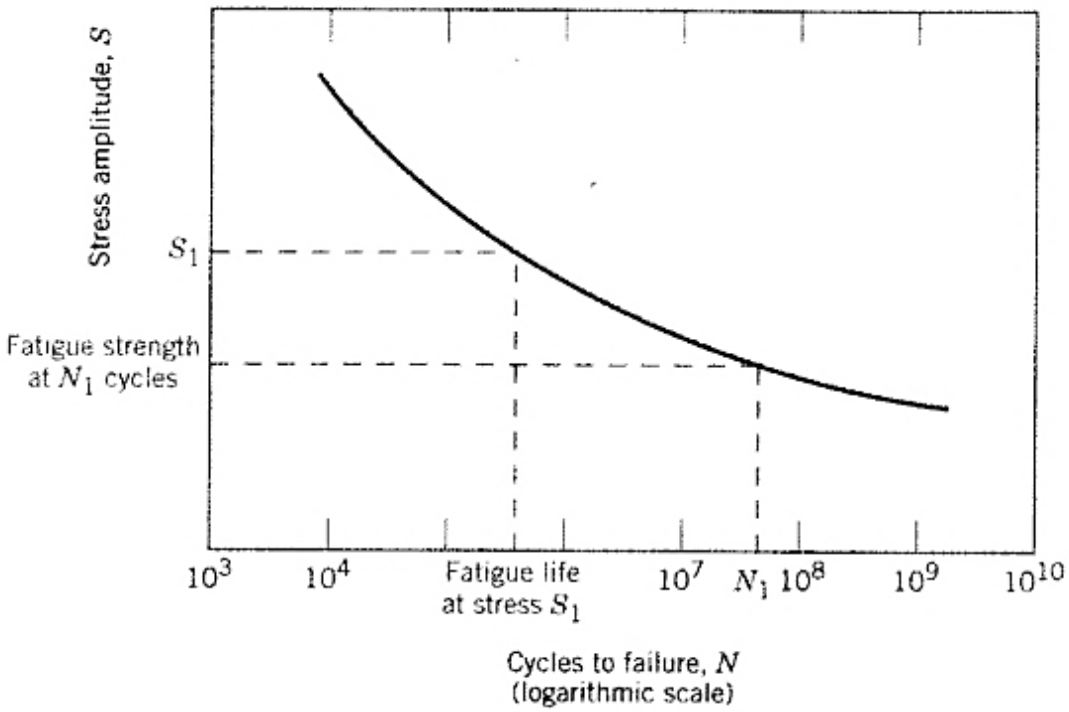

Figure 5. Stress amplitude (S) verses logarithm of the number of cycles to fatigue failure (N) for a material that does not have fatigue limit.(From [6])

Hogging and sagging represents the clearest example of fatigue loading on aluminum ship structures. A hogging and sagging cycle each represent the minimum stress, σ_{min}, and the maximum stress, σ_{max}, applied to the ship, respectively. The mean stress, $\sigma_{m,}$ is found through Equation 1 while the stress ratio, R, can be calculated from Equation 2. The stress range, σ_r, and the stress amplitude, σ_a, are solved through Equation 3.

$$\sigma_m = \frac{\left(\sigma_{\max} + \sigma_{\min}\right)}{2} \tag{1}$$

$$R = \frac{\sigma_{\min}}{\sigma_{\max}} \tag{2}$$

$$\sigma_a = \frac{\left(\sigma_{\max} - \sigma_{\min}\right)}{2} = \frac{\sigma_r}{2} \tag{3}$$

The stress amplitude (σ_a) is the stress seen on the ordinate of Figure 5. Based on the ultimate strength, σ_{ut}, and the fatigue limit, σ_{fat}, a larger mean stress or larger stress amplitude will greatly reduce the number of cycles to failure at a given stress value. The relationship between the mean stress and the stress amplitude required for a given fatigue life can be estimated by using constant-life relationships such as the Goodman equation, Equation 4.

$$\sigma_a = \sigma_{fat}\left[1 - \frac{\sigma_m}{\sigma_{ut}}\right] \tag{4}$$

The Goodman relationship demonstrates that as the mean stress increases positively, the stress amplitude that is permissible for a given fatigue life decreases.[7] It is important to note that a negative mean stress would actually increase the allowed stress amplitude over what is predicted for a zero mean stress. Residual stresses from processes such as welding or shot-peening directly impact the mean stress; and therefore, the fatigue life of the ship structure.

1. Causes and Control of Residual Stresses

Residual stresses can cause SCC by themselves or can combine with applied stresses to cause SCC. In addition, residual stresses can lower the fatigue life for a given stress amplitude. Residual stresses are, as the name implies, stresses that are left over from some other process and that exist *without any applied load* on the material. Common sources of residual stresses on ships are from welding, riveting, and from the torqueing of bolts. Fusion welding, in particular, can generate large, tensile residual stresses in aluminum ship structures. Ganguly et al. states that the unequal expansion and contraction of the weld metal in conjunction with the surrounding heat affected zone (HAZ) creates both tensile and compressive residual stresses in welded plate.[8] According to Kou, the longitudinal residual stress, σ_x, (stress in the x-direction long the weld line), can be calculated as a function of the distance from the weld centerline, y, by

Equation 5 if the maximum residual stress, $\square_m$, which can be as high as the yield strength, and the width of the tension zone, b, are known (Figure 6).[9]

$$\sigma_x(y) = \sigma_m \left[1 - \left(\frac{y}{b}\right)^2\right] \exp\left[-\frac{1}{2}\left(\frac{y}{b}\right)^2\right] \tag{5}$$

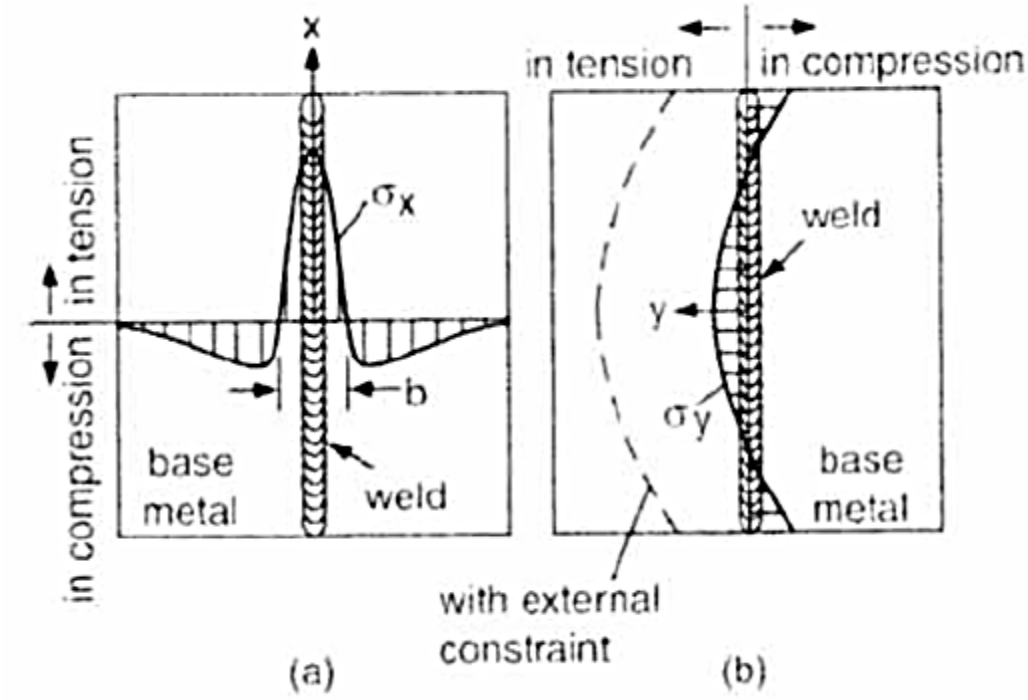

Figure 6. Typical distributions of (a) longitudinal, $\square_x$, and (b) transverse, $\square_y$, residual stresses in butt welds.(From [9])

Figure 7 shows a comparison of measured residual stresses, S_y, normalized to the yield strength, S_{ys} in the x-direction, as seen in Figure 6, to a finite element analysis model as a function of moving in the transverse direction from the weld centerline where W is half of the width of the welded plate.[9] In this case, the residual stress exceeded the nominally reported yield strength by about 10% near the weld nugget. Stresses of this magnitude, would actually result in the plastic deformation of the material in the weld nugget.

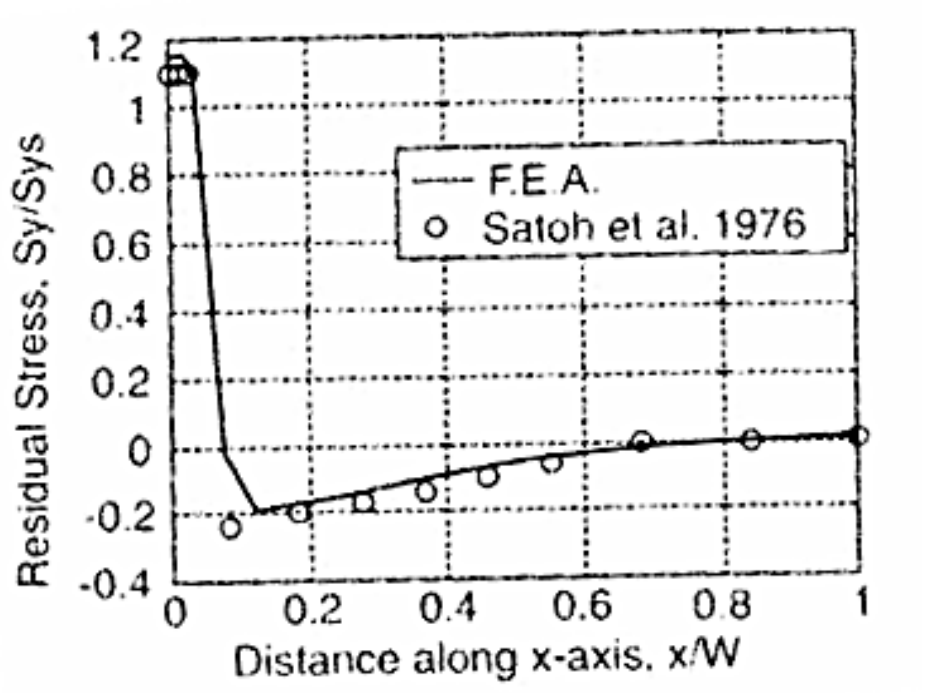

Figure 7. Measured and calculated residual stresses in butt weld of AA5083.(From [9])

James et al. reports several stress profiles of gas metal arc/metal-inert-gas (MIG) welds on 8mm thick 5083-H321 aluminum plate as shown in Figure 8. This work utilizes synchrotron diffraction, which is more accurate than laboratory x-ray diffraction, to measure the residual stresses. The intense high energy electromagnetic radiation can penetrate deeper into the test material and can measure larger-scale areas very rapidly in one scan. Peak stresses of +80 to 90MPa parallel to the weld line were measured through the cross-section of the plate. These stresses were located at 22mm from the weld centerline and 15mm from the weld toe placing it outside the heat affected zone (HAZ) by 10mm. The microstructural HAZ boundary was measured to be 12mm from the centerline of the weld. Stresses transverse to the weld center line were nearly all tensile through the cross-section of the plate.[10] Thus, the presence of large tensile stresses means a greater probability of cracking the passive oxide layer on the aluminum surface leading to a crack initiation site and a higher susceptibility to SCC.

The fact that the tensile stresses continue into the material's depth for several millimeters, points to the role of tensile stress in propagating a stress corrosion crack into the interior of the material.

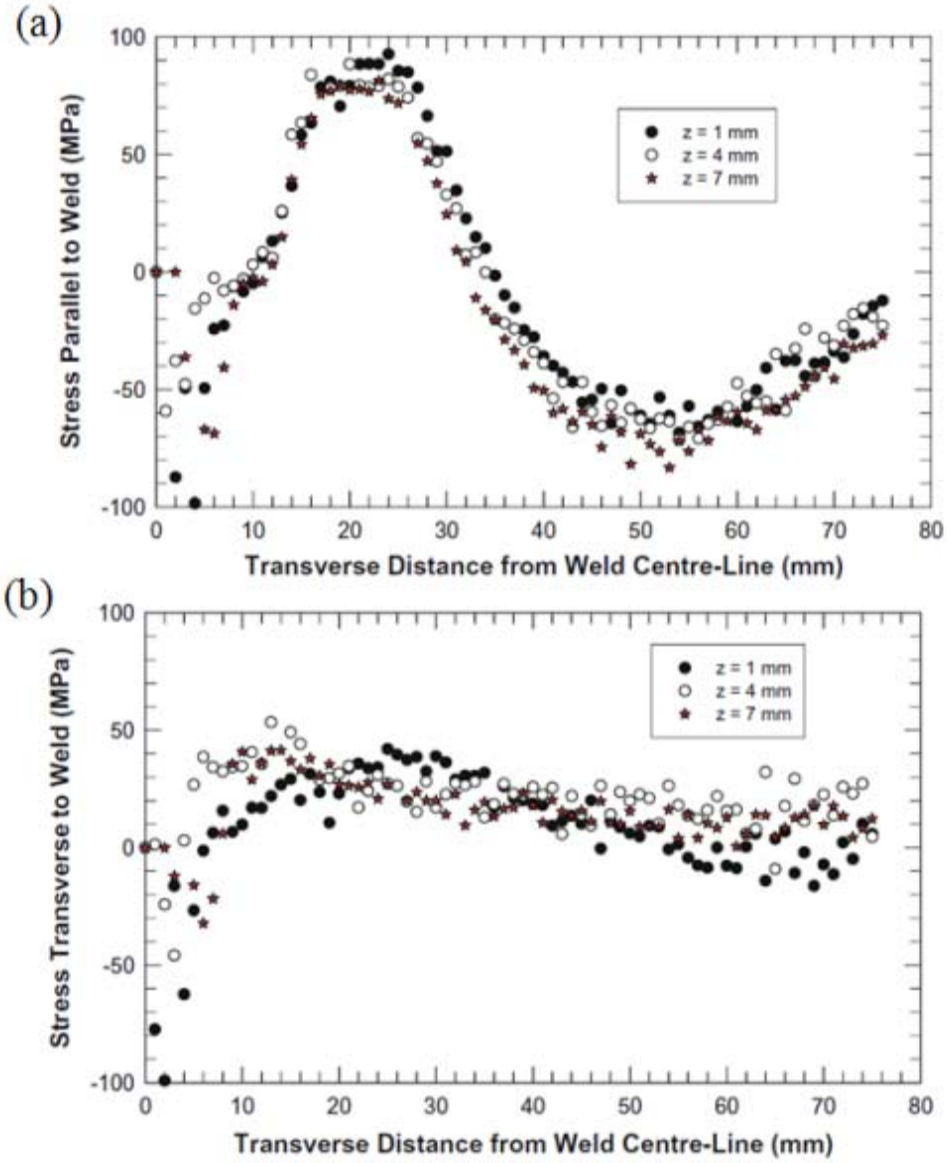

Figure 8. (a) Comparison between longitudinal stresses in AA5083-H321 MIG weld at depths of 1, 4, and 7mm (b) Comparison between transverse stresses in AA5083-H321 MIG weld at depths of 1, 4, and 7mm.(From [10])

Residual stresses can also adversely affect the fatigue properties of welded material. Figure 9 shows the importance of welding in the fatigue performance of marine

aluminum. Here AA5083 is tested in four different conditions: 1) bulk material in air; 2) bulk material in seawater; 3) welded material in air; and 4) welded material in seawater. These results illustrate over a 300% drop in the fatigue limit from a bulk air condition at 192MPa to an as-welded condition in air at 64MPa.[11] It is important to note that while residual stresses from the welding can affect the fatigue performance, it was also a change in microstructure from the base plate that drove some of the dramatic changes in fatigue life observed by Benedictus-deVries.[11]

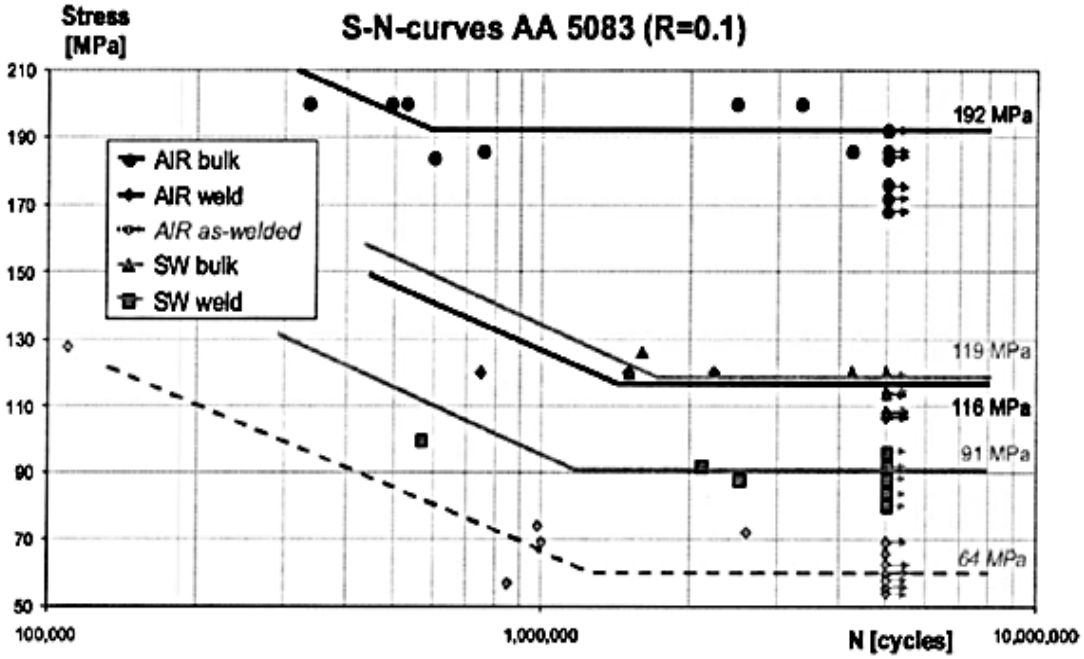

Figure 9. SN-curve and fatigue limits for AA5083 with a stress ratio of 0.1 of welded and un-welded samples tested in air and in seawater.(From [11])

B. INTRODUCTION

1. Reduction of Residual Stresses from Peening Processes

One of the most effective ways to mitigate SCC and fatigue crack growth is to reduce the tensile stresses of the material by imposing a compressive stress on the surface of the effected material. Cracks propagate because of the elastic energy release provided by tensile stresses applied to the material; therefore, introducing a compressive stress into the material will reduce the driving force for crack formation and crack propagation.

Three of the most common ways to create compressive stresses on surfaces are by shot peening, ultrasonic impact treatment (UIT), and laser peening.

Shot peening is a process in which small, hard spherical particles with diameters ranging from 0.1 to 1.0mm are propelled at high velocities and impinge on the surface being treated. The depth of the compressive layer is typically between one-quarter to one-half the ball diameter and up to about 250□m, which is rather shallow for most structures.[6,12] Shot-peening has been shown to increase the fatigue life as seen in Figure 10. Here shot peeing increases the fatigue limit, but only half as much compared to that of laser peening. Another limitation of shot peening is the non-uniformity of the imposed compressive stresses across the surface as there is no certainty of complete coverage. A third drawback of shot peening is the resulting roughened surface. This layer of material needs to be removed in order to restore the initial surface qualities, and in doing so some of the compressive layer is also removed.[12]

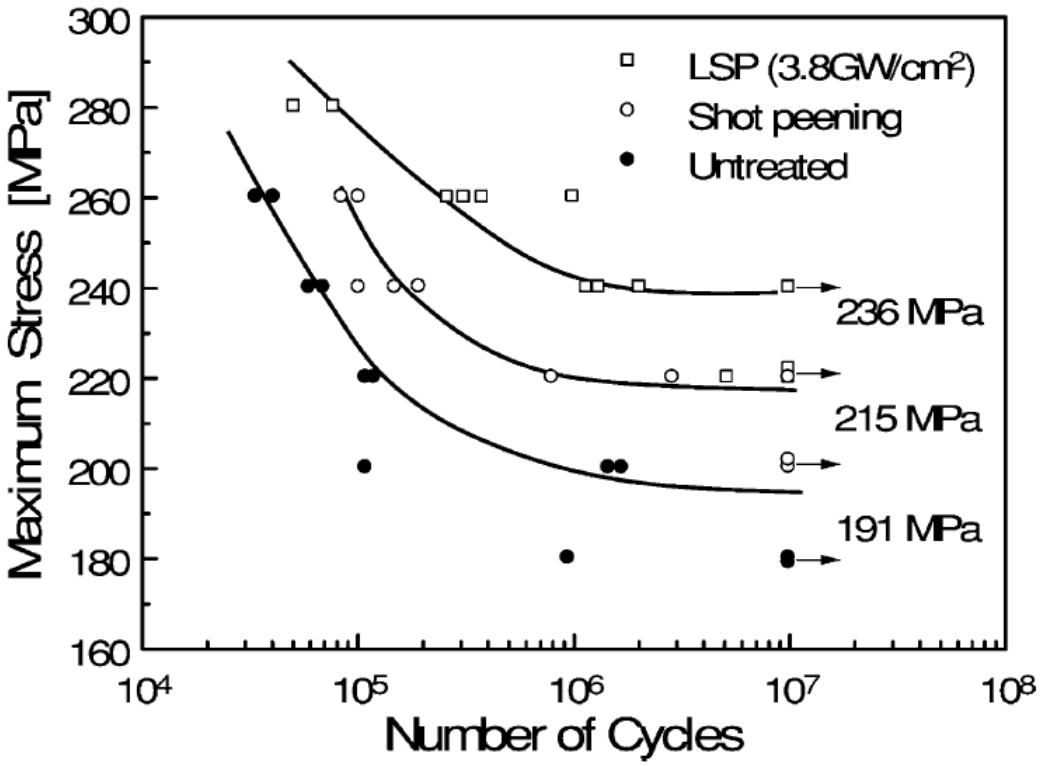

Figure 10. An S-N curve comparing the fatigue limit increases of 7075-T7351 aluminum alloy from shot peening and laser peening.(From [12])

UIT is based on converting ultrasonic oscillations into controlled impulses of ultrasonic impacts.[13,14] It employs continuous ultrasonic vibrations from a hardened material tip in continuous contact with the work piece to impose a compressive residual stress.[13] Much like shot peening, UIT provides a stable and controlled compressive residual stress at the near surface. The surface also experiences a high rate of plastic straining and some heating during impact.[14] X-ray diffraction-based residual stress measurements (Figure 11) demonstrates how UIT can impose larger compressive residual stresses ranging from -150 to -200MPa at the surface to around -70MPa one millimeter into the 7075-T6511 (aluminum alloy) work piece.[14]

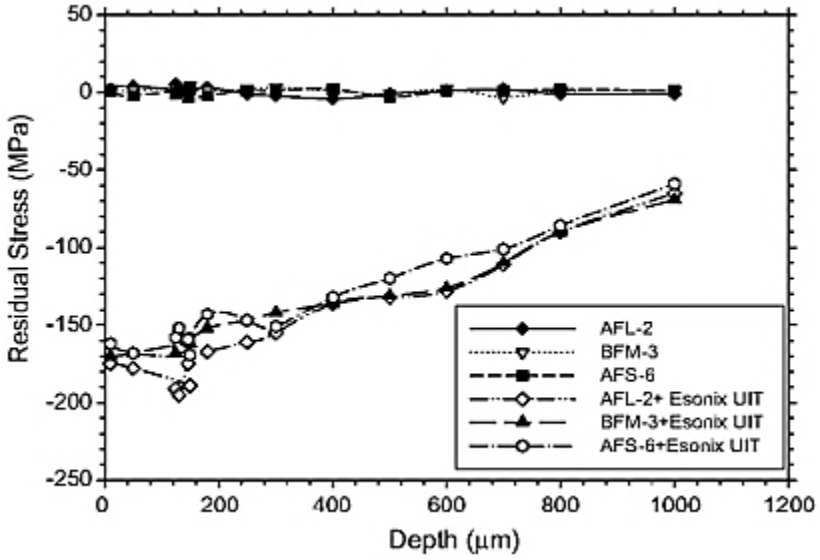

Figure 11. Residual stress distribution prior to and after the *Esonix* UIT on lightly (AFL-2), moderately (BFM-3), and severly (AFS-6) exfoliated 7075-T6511 specimens.(From [14])

Laser peening is a relatively new surface treatment technology that greatly improves the material performance beyond the results of shot peening and UIT.[15] Laser peening can induce compressive residual stresses to a depth typically around 1 to 2 mm, which is a full order of magnitude greater than shot peening.[15] The peening process starts out by a high energy laser pulses, often a neodymium (Nd) glass laser, being focused on the surface of the sample (Figure 12). The ablative surface layer absorbs the laser pulses and vaporizes, forming a plasma. The thin water-tamping layer,

which is transparent in order to allow the laser pluses to go through, confines the plasma in the horizontal plane, thus re-directing a shock wave back into the material. This shock wave, which can be several gigapascals of pressure, results in plastic deformation of the material at the surface, thus imposing the large compressive residual stresses. The thermal loading on the material during this process is quite limited.[1,12,16,17] Even though a plasma forms at the surface of the work piece, the temperature of the work piece only rises to around 149°C for a short period of time.[18] Early in the development of laser peening, an ablative layer was necessary to absorb the laser and create the plasma to create the shock wave, but as the technology has progressed the ablative layer, which could be tape or paint, has become optional. Unlike shot peening, laser peening leaves a relatively smooth surface finish. If tape were used in the laser peening process, a quick brushing of the surface may be necessary to remove any debris that is leftover after it is removed.

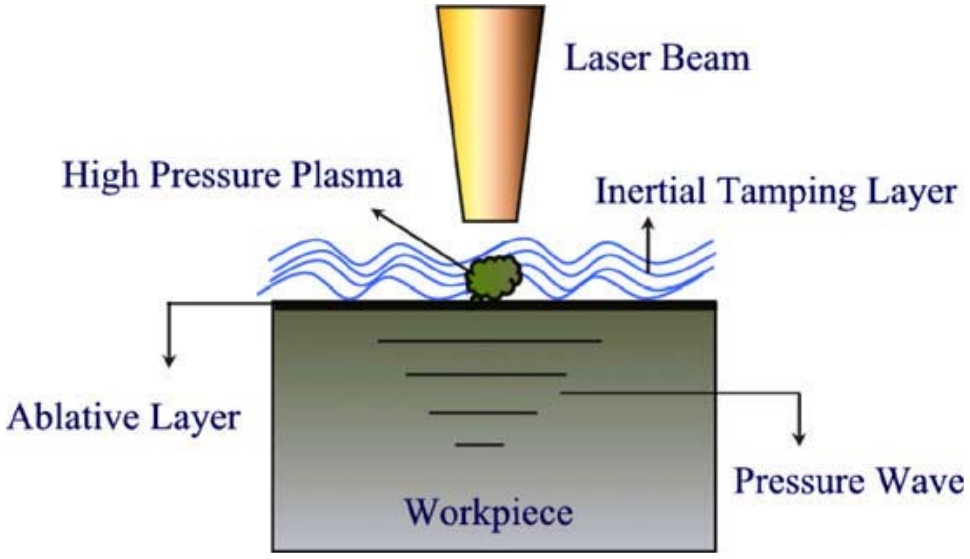

Figure 12. Illustration of the laser peening process.(From [17])

Parameters such as power of the laser, target spot size, duration of the pulse, type of confining medium, and number of passes will determine the amount of induced stress in the material of the work piece. Laser peening can impose a compressive residual stress up to ten times deeper than traditional shot peening methods and enhance the fatigue strength as seen in Figure 13.[17,18] Here the fatigue crack growth rates on friction stir

welded 2195 aluminum alloy were plotted for three different conditions: 1) un-peened; 2) shot peened; and 3) laser peened under a stress ratio of 0.1. The laser peening improved the fatigue crack growth rate, but the shot peening did not when compared against an un-peened specimen. In this case a steeper slope means a shorter fatigue life.

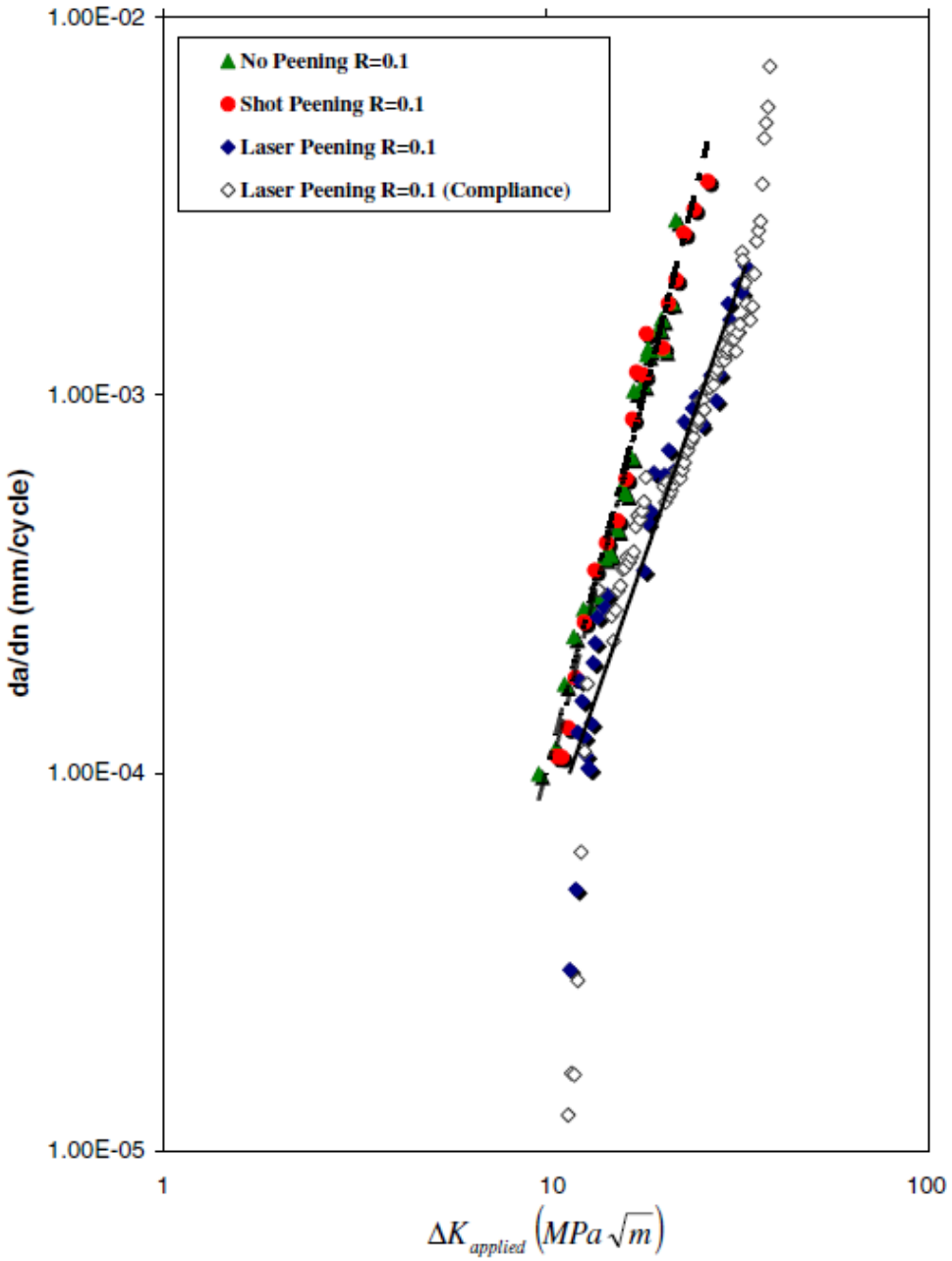

Figure 13. Fatigue crack growth rates for friction stir welded AA2195 at a stress ratio, R, of 0.1 for various peening conditions.(From [17])

These examples make clear the importance of residual stresses to fatigue life and stress corrosion cracking. Because mitigation strategies such as shot peening, UIT and laser peening depend upon the control of residual stresses in the surface of the material, accurate measurement of residual stresses is key to the application of these mechanical property enhancing approaches.

C. METHODS FOR MEASURING RESIDUAL STRESS

There is an array of different residual stress measurement techniques. Most notable are diffraction (neutron, synchrotron, and tube based laboratory x-ray), hole-drilling, slitting method, and contour method.[8,10,15–17,19–26] In the contour method, as discussed by Hill et al., a specimen containing residual stresses is cut in half along a straight line and will deform as a result of the traction free boundary condition of the new free surface.[15] Measuring the deformed free surface (i.e. the displacements normal to the free surface) and the tractions required to displace these points back to their pre-cut locations are equivalent to the original residual stress acting normal to the plane of free surface of the cut.[15] Hill et al. goes on to describe the slitting method, which is also known as the crack compliance method. The strain verses depth is measured by metallic foil strain gauges as incremental cuts into the test specimen, which will be used to solve for the residual stresses normal to the plane of the cut assuming elastic deformation and elastic inverse methods.[15] Hole drilling is another method for determining in-plane (i.e. bi-axial) residual stresses. A strain gage rosette records the strain relaxations as a hole is drilled through it into the test material. The strains are then converted into stress by assuming that the stresses are uniform with distance as per ASTM E837–08.[27,28]

Neutron diffraction involves the use of pulses of high-energy protons which strike a heavy-nucleus target. The target then produces a different set of neutrons at the same pulse rate, but with a defined energy distributions.[8] These secondary neutrons travel to a test specimen where diffraction occurs at Bragg angles (Bragg angles are discussed below). Because of the time it takes for the neutrons to reach the test specimen (i.e. time-of-flight) and depending on the wavelength of the neutrons a diffraction spectrum containing many reflecting planes are probed on one measurement.[8] This technique

allows the simultaneous detection of all diffraction peaks referring to different lattice planes at different orders of diffraction. Strain values can be determined and eventually converted into stresses. Synchrotron x-ray diffraction uses x-rays instead of neutrons as the incident energy particle striking the test specimen and causing diffraction. Synchrotron x-ray diffraction use higher powered x-rays compared to laboratory x-ray diffraction, but both work on the same principles as described below.

1. Laboratory X-ray Diffraction

a. General Background

X-ray diffraction has become the one of the standard methods for measuring residual stress in the past few decades.[16,17,19–26] The phrase "measuring a stress" is somewhat misleading because stress is an extrinsic property and cannot be measured directly, but what can be measured is strain.[19] X-ray diffraction measures the strain or the changes in strain, from an unstressed state, by measuring the shifts in the diffraction peak due to an external or residual stress. The measured strains are then converted into a stresses through Hooke's law.[16,19] These calculations assume a linear elastic deformation of the material.[16] Prevey states that residual stresses determined using x-ray diffraction assume an arithmetic average of the stress in the volume of the material defined by the irradiated area. This volume may vary from square millimeters to square centimeters and is based on the depth of penetration of the x-ray beam, which is governed by the linear absorption coefficient of the material based on the type of radiation used.[19] In aluminum based alloys, more than 70% of the diffracted radiation comes from the top 100 microns of the material for all the most commonly used laboratory x-ray sources.[19] Because of this shallow depth of penetration, the spatial resolution of the residual stresses will be approximately 10 to 100 times more than other stress determining stress measuring techniques such as dissection, ultrasonic, and magnetic.[19] The depth of penetration is dependent on the type of radiation, and in practice there are limited types of useful radiation. For example Cu-Kα radiation, Co-Kα radiation and Cr-Kα radiation are some of the common types of radiation used in laboratory settings. The limited selection of laboratory x-ray tubes leads to a limited

choice of crystallographic planes that can be used for the residual strain measurement. For instance, Table 1 shows the possible {hkl} reflection planes available for aluminum using these different types of radiation where {111), {200}, etc. are the Miller indices of the reflection planes for the material, 2θ is the Bragg angle, and Cu, Co, and Cr are the types of K-α radiation.

d (h k l)	2□	2□	2□
	Cu	Co	Cr
{111}	38.50	45.02	58.67
{200}	44.76	52.47	68.90
{220}	65.15	77.39	106.27
{311}	78.30	94.29	139.48
{222}	82.51	99.94	156.96
{400}	99.19	124.29	n/a
{331}	112.15	148.93	n/a
{420}	116.71	162.61	n/a
{422}	137.68	n/a	n/a
{333},{511}	163.11	n/a	n/a

Table 1. Relationship between 2□ angles and their associated reflection planes aluminum. The n/a in the table means that the corresponding 2□ angle for that reflection for that radiation wavelength is beyond 180 degrees.

Measuring the strain in a material by x-ray diffraction starts by utilizing Bragg's law. Bragg's law uses the geometry from Figure 14 and relates the 2θ angle to the d_0 value. This relationship comes from the physics of diffraction. Cullity describes diffraction as a single beam of energy composed of mutually reinforcing rays (i.e. rays that have the same phase and wavelength) resulting from the scattering effect when an atom is struck by x-rays.[20] In Figure 14, an incident beam with a given wavelength, λ, enters from the left (1, 1a, 2, etc.) and strikes the atoms of the lattice. The incident beam is scattered in all directions by all the atoms in every plane that the incident beam reaches.

Both constructive and destructive interference occurs resulting in a diffracted beam, which exits to the right in direction of rays 1', 1a', 2', etc. Some diffracted rays will be in the same direction and have the same phase, thus resulting in a diffracted beam with a strong intensity.[20]

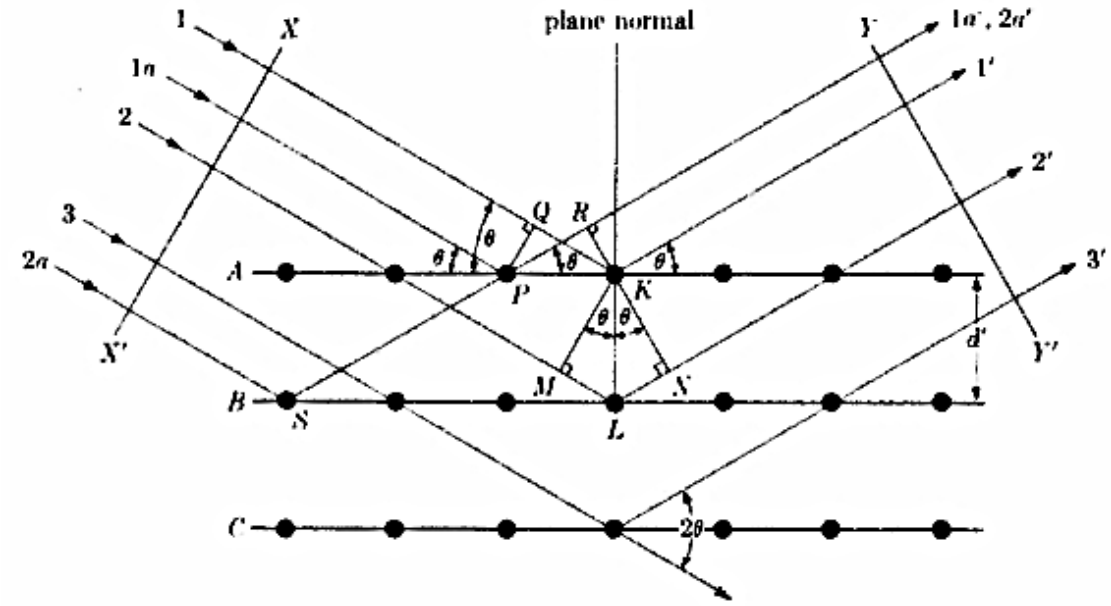

Figure 14. Principle of diffraction based on the relationship between □, the diffracted beam angle, 2□, and d' gives rise to Bragg's law, n□=2d'sin□.(From [20])

The relationship between the wavelength, □, the diffracted beam angle, 2□, and the interplanar distance of the lattice, d', gives rise to Bragg's law (Equation 6) where n is the order of the diffraction.

$$n\lambda = 2d' \sin\theta \tag{6}$$

Based on the fact that sinθ cannot be greater than unity, the limitations of λ, (cannot be too large or too small) and using a first-order reflection (i.e. n=1) Equation 6 becomes Equation 7.[20]

$$\lambda = 2d \sin\theta \tag{7}$$

Knowing the incident radiation wavelength, □, and the 2□ value from the centroid of the diffraction peak profile, the interplanar lattice spacing (i.e. d spacing), d, can be calculated. From the d spacing for a given {hkl} reflection, the unit cell parameter, a, for cubic materials can be calculated using Equation 8.

$$d = \frac{a}{\sqrt{h^2 + k^2 + l^2}} \tag{8}$$

The choice of the diffraction peak, 2θ, greatly impacts the precision of the stress measurement. The larger the Bragg angle (2θ angle) the greater the sensitivity of the x-ray residual strain measurement and the greater the precision of the stress calculation, so in general, one should use the largest Bragg angle for a given radiation as possible. In practice, 2θ should be greater than 120 degrees.[19] The Bragg angle as described in Figure 15 comes from the fact that the incident beam, S, the normal to the reflecting plane, N, and the diffracted beam, D, are always coplanar, and the angle between the diffracted beam and the transmitted beam is always 2θ.[20] Note that d_0 in Figure 15 is the interplanar spacing of the lattice, also known as the d spacing, when ψ=0 degrees. The stress, σ, is the applied or residual stress acting on the lattice. The term d_ψ in Figure 15 (b) is the interplanar spacing of the lattice when the sample is rotated by some ψ angle off of the sample's normal. If there is a change in the d spacing of the lattice, then there will be a change in the 2θ value as the sample is rotated from ψ=0 in Figure 15 (a) to ψ=ψ in Figure 15 (b). Measuring this change in the d spacing is the basic principle by which strain is measured using x-ray diffraction. As shown in Figure 16, the shifts in the 2θ values result in a change of the measured d spacing, which is used to determine the strain of the material.

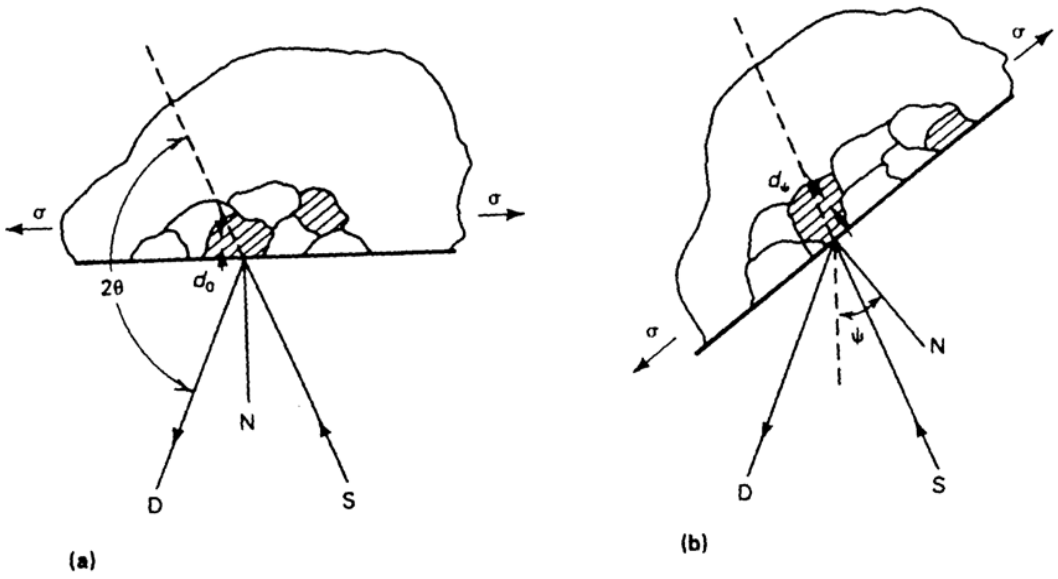

Figure 15. Description of the Bragg angle in regards to the principles behind x-ray diffraction stress measurements. (a) ☐=0. (b) ☐=☐ (sample rotated at a known ☐ angle).(From [19])

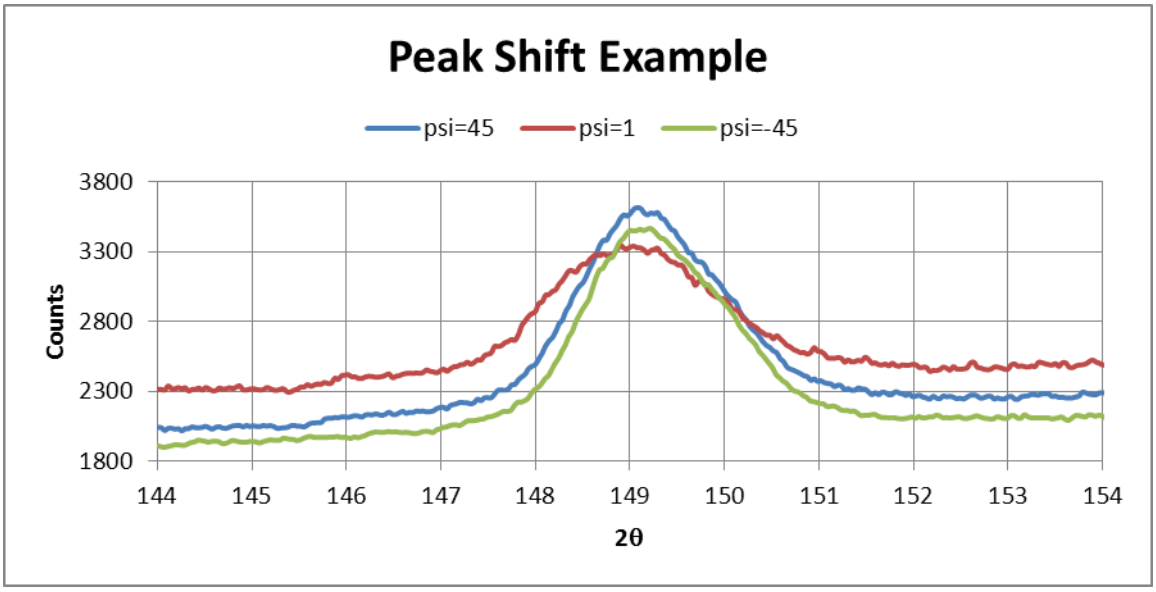

Figure 16. Diffraction peaks from 5083 aluminum alloy showing how the 2☐ values shift based on different elastic strains. Here the peak centroid of ☐=1 degrees is shifted to the left of the other two peaks at ☐=±45 degrees.

Once the d spacing is measured from the centroid of the 2θ angle, the measured strain can be determined. Using a known d_0 value (the unstressed lattice spacing) and a measured $d_{\phi\psi}$ (d spacing for a given ψ and ϕ angle), the strain in the direction of the incident beam, ε'_{33}, can be obtained using Equation 9.[21]

$$\left(\varepsilon'_{33}\right)_{\phi\psi} = \frac{d_{\phi\psi} - d_0}{d_0} \tag{9}$$

□ represents the angle between the direction of the incident beam and the normal of the sample (Figure 17). L_1, L_2, and L_3 in Figure 17 represent the laboratory coordinate system of the x-ray diffraction goniometer, and S_1, S_2, and S_3 represent the test sample's coordinate system. □ is the angle of rotation in the 1–2 plane.

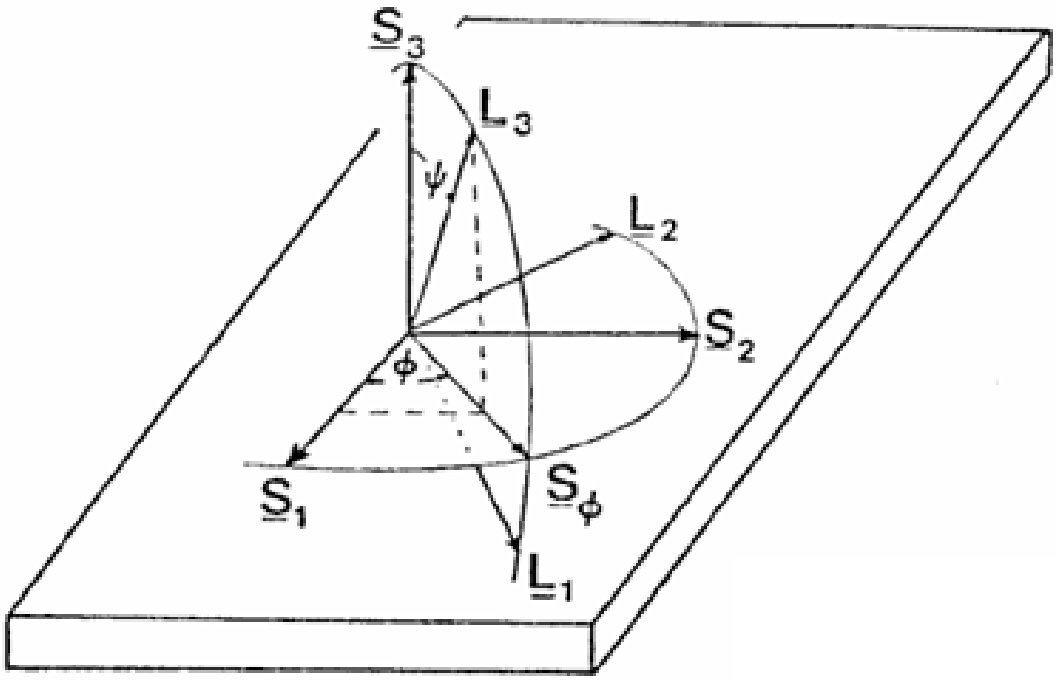

Figure 17. Relationship of the laboratory coordinate system L_i, specimen coordinate system S_i, and □□□ angles.(From [21])

The full, three-dimensional, strain tensor can be measured by repeating the measurement described in Equation 9 for a series of ☐ and ☐ angles. At a minimum, the strain tensor measurement requires six, independent measurements to account for the six unknowns in Equation 10, where ☐$_{ij}$ are the components of the strain tensor for a given ☐ and ☐ angle.[21]

$$\left(\varepsilon_{33}^{'}\right)_{\phi\psi} = \frac{d_{\phi\psi} - d_0}{d_0} = \varepsilon_{11}\cos^2\phi\sin^2\psi + \varepsilon_{12}\sin 2\phi\sin^2\psi + \varepsilon_{22}\sin^2\phi\sin^2\psi + \varepsilon_{33}\cos^2\psi + \varepsilon_{13}\cos\phi\sin 2\psi + \varepsilon_{23}\sin\phi\sin 2\psi \tag{10}$$

Once enough angle-independent strain measurements have been collected, the strain tensor can be determined through the classic linear system of equations as represented by Equation 11.

$$A\cdot\vec{x} = \vec{b} \tag{11}$$

In Equation 11, $\vec{x}$ (the strain tensor) can be found by inverting A (the coefficient matrix) and pre-multiplying each side of the equation as long as A is invertible. $\vec{b}$ represents the ☐'$_{33}$ terms. If more than six independent sets of ☐ and ☐ angles are used, then the accuracy of the strain calculation using linear least squares regression will improve; however, QR factorization will be required instead of simply inverting the A matrix.[29,30] Equation 12 is a deconstruction of Equation 10 in the form of Equation 11 used in this work for the tensor calculations. Here the trigonometric functions are combined into the A matrix, and the strain tensor is solved as discussed above.

$$\begin{pmatrix} \left(\varepsilon_{33}^{'}\right)_{\phi_1\psi_1} \\ \left(\varepsilon_{33}^{'}\right)_{\phi_2\psi_2} \\ \left(\varepsilon_{33}^{'}\right)_{\phi_3\psi_3} \\ \left(\varepsilon_{33}^{'}\right)_{\phi_4\psi_4} \\ \left(\varepsilon_{33}^{'}\right)_{\phi_5\psi_5} \\ \left(\varepsilon_{33}^{'}\right)_{\phi_6\psi_6} \end{pmatrix} = \begin{bmatrix} a_1 & b_1 & c_1 & d_1 & e_1 & f_1 \\ a_2 & b_2 & c_2 & d_2 & e_2 & f_2 \\ a_3 & b_3 & c_3 & d_3 & e_3 & f_3 \\ a_4 & b_4 & c_4 & d_4 & e_4 & f_4 \\ a_5 & b_5 & c_5 & d_5 & e_5 & f_5 \\ a_6 & b_6 & c_6 & d_6 & e_6 & f_6 \end{bmatrix} \begin{pmatrix} \varepsilon_{11} \\ \varepsilon_{12} \\ \varepsilon_{13} \\ \varepsilon_{22} \\ \varepsilon_{23} \\ \varepsilon_{33} \end{pmatrix} \tag{12}$$

where

$$a_i = \cos^2\phi \sin^2\psi, b_i = \sin 2\phi \sin^2\psi, c_i = \sin^2\phi \sin^2\psi, d_i = \cos^2\psi,$$
$$e_i = \cos\phi \sin 2\psi,\ f_i = \sin\phi \sin 2\psi \quad and \quad i = 1:6$$

Once the strains are found, the stresses can be calculated from the general form of Hooke's law, Equation 13, in the S_i coordinate system as represented in Figure 17. σ_{ij} represents the stress tensor, C_{ijkl} is the elastic stiffness tensor, and ε_{kl} is the strain tensor.[21]

$$\sigma_{ij} = C_{ijkl}\varepsilon_{kl} \tag{13}$$

For an isotopic material the general form of Hooke's law becomes Equation 14 where E is the elastic modulus, □ is Poisson's ratio, □$_{ij}$ is the delta function (i.e. i≠j), and i, j, and k represent the different direction planes.[21]

$$\varepsilon_{ij} = \frac{1+\nu}{E}\sigma_{ij} - \delta_{ij}\frac{\nu}{E}\sigma_{kk} \tag{14}$$

Substituting Equation 14 into Equation 10 the general form of the stress tensor for an isotropic material becomes Equation 15.[21]

$$\begin{aligned}\left(\varepsilon_{33}^{'}\right)_{\phi\psi} = \frac{d_{\phi\psi} - d_0}{d_0} = \frac{1+\nu}{E}\left\{\sigma_{11}\cos^2\phi + \sigma_{12}\sin 2\phi + \sigma_{22}\sin^2\phi - \sigma_{33}\right\}\sin^2\psi \\ + \frac{1+\nu}{E}\sigma_{33} - \frac{\nu}{E}\left(\sigma_{11} + \sigma_{22} + \sigma_{33}\right) \\ + \frac{1+\nu}{E}\left\{\sigma_{13}\cos\phi + \sigma_{23}\sin\phi\right\}\sin 2\psi\end{aligned} \tag{15}$$

The stress tensor can be found by either pre-multiplying the strain tensor by the stiffness matrix as in Equation 16, or by solving Equation 15 through the classical linear system of equations as described above. The elastic stiffness matrix in Equation 16 is for an isotropic material. Note that AA5083-H116 is a face centered cubic material. G in Equation 16b is the shear modulus, and λ in Equation 16a is just a re-arrangement and collection of other elastic constants.[31]

$$\begin{pmatrix}\sigma_{11}\\ \sigma_{22}\\ \sigma_{33}\\ \sigma_{23}\\ \sigma_{13}\\ \sigma_{12}\end{pmatrix}=\begin{bmatrix}2*G+\lambda & \lambda & \lambda & 0 & 0 & 0\\ \lambda & 2*G+\lambda & \lambda & 0 & 0 & 0\\ \lambda & \lambda & 2*G+\lambda & 0 & 0 & 0\\ 0 & 0 & 0 & G & 0 & 0\\ 0 & 0 & 0 & 0 & G & 0\\ 0 & 0 & 0 & 0 & 0 & G\end{bmatrix}\begin{pmatrix}\varepsilon_{11}\\ \varepsilon_{22}\\ \varepsilon_{33}\\ \varepsilon_{23}\\ \varepsilon_{13}\\ \varepsilon_{12}\end{pmatrix} \tag{16}$$

$$\lambda=\frac{E+\nu}{(1+\nu)*(1-2\nu)} \tag{16a}$$

$$G=\frac{E}{2(1+\nu)} \tag{16b}$$

It should be of note that the terms in the strain tensor from Equation 12 need to be in the proper order before using them in Equation 16 to find the stress tensor in order to comply with proper matrix multiplication. Given Equations 10 and 15 the strains and stresses can be calculated by using any of the previously mentioned techniques, respectively.

b. "d vs. $\sin^2\psi$" Technique

Important increases in measurement speed and simplicity can be gained by making a few key assumptions about the nature of the stresses in the surface of crystalline materials. Assuming a plane stress distribution with zero components of strain in the z-direction, leads to the simplification of Equation 17. This approach is known as the "d vs. $\sin^2\psi$ technique," and it has been instrumental in determining bi-axial stresses for over 60 years.[21] It can be seen that if these assumptions are true, then Equation 10 predicts a linear relationship between measured d-spacing and $\sin^2\psi$. Equation 17a is used when there is zero in-plane shear stress. Equation 17b accounts for any in-plane shear stress.

$$\frac{d_{\phi\psi}-d_0}{d_0}=\frac{1+\nu}{E}\sigma_\phi\sin^2\psi-\frac{\nu}{E}(\sigma_{11}-\sigma_{22}) \tag{17}$$

$$\sigma_\phi=\sigma_{11}\cos^2\phi+\sigma_{22}\sin^2\phi \tag{17a}$$

$$\sigma_\phi = \sigma_{11}\cos^2\phi + \sigma_{12}\sin 2\phi + \sigma_{22}\sin^2\phi \qquad (17b)$$

□□ is the stress in a given S□ direction calculated from the slope of a least-squares line fitted to experimental data measured at various □ angles when the elastic constants E, □, and the unstressed plane spacing, d_0, are known.[21] $\square_{11}$ and $\square_{22}$ are the principle stresses from the stress tensor. In most situations d_0 is not known, but can be replaced by the lattice spacing (i.e. d spacing) measured at □=0.

The total error introduced by this substitution is less than 0.1% of the final stress value and is negligible when compared to other sources of error.[21]

In reality, there are three basic types of d vs. $\sin^2\psi$ behavior as shown in Figure 18. Equation 10 predicts "regular" behavior as seen in curves "a" and "b" of Figure 18.[21] Curve "a" occurs when there is no out of plane shear strain, i.e. when ε_{13} and ε_{23} are both zero, while the branching observed in curve "b" occurs when either or both of these terms are non-zero. The slope of the linear least squares fit on curves "a" and "b" is the value of the residual stress at that test location. Note that a positive slope is produced by a tensile stress and a negative slope is produced by a compressive stress. The "ψ-splitting" in curve "b" comes about because of the sin(2ψ) term in Equation 10, which indicates that the out-of-plane shear strains are non-zero. The greater the ψ-splitting on curve "b", the more out of plane shear. Curve "c" exhibits oscillatory behavior, which cannot be explained by Equation 10.

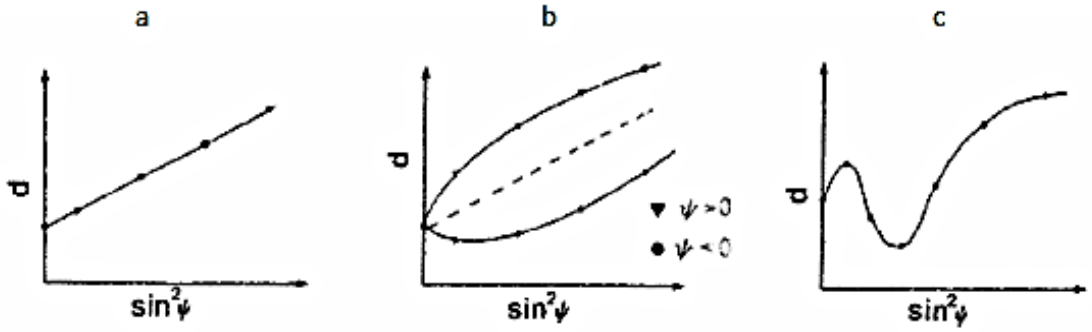

Figure 18. Three basic types of d vs. $\sin^2\psi$ plots commonly encountered in residual stress

analysis. (a) "regular," linear behavior, (b) branched behavior, and (c) oscillatory behavior.(From [21])

D. THESIS OBJECTIVES

The work in this thesis seeks to understand and examine the influence of laser peening on IG-SCC of marine-grade, welded aluminum alloys. While research has been performed on the measuring the residual stresses in MIG welded AA5083-H321 aluminum for fatigue analysis, the effects of different peening conditions was not considered.[10] The effects of laser peening have been considered on Alloy 22 (a nickel-based alloy) by Hill et al.[15], 2xxx series aluminum alloys by Hatamleh[17], and on a series of different materials in the review by Montross et al.[12], but not on a 5xxx series aluminum alloy. Therefore, the main objectives addressed in this thesis are:

1. *Use XRD techniques to evaluate residual stresses in MIG welded AA5083.*

The objective is to use standard XRD techniques to measure residual stresses in MIG welded samples to compare against data in literature and to establish a stress baseline prior to laser peening.

2. *Use XRD techniques to evaluate residual stresses after laser peening.*

This objective is to use standard XRD techniques to measure the extent of intentionally imposed compressive residual stresses from laser peening on MIG welded AA5083. Longer and more intense peening conditions should impose larger compressive residual stresses deeper into the material. Test points in the HAZ and in the base metal and at different depths will be measured to understand how the stresses develop in the material.

3. *Develop a full tensor stress measurement approach based on x-ray diffraction.*

Because of the complexities of the weld, anisotropy from rolling, and laser peening a full tensor state of residual stress will be measured for a better understanding the full mechanical state at any given location.

II. EXPERIMENTAL PROCEDURE

A. MATERIAL PROCESSING

1. Plate Fabrication

This work dealt solely with aluminum alloy 5083 with a H116 heat treatment (AA5083-H116). The AA5083-H116 material was in the form of a 36x24inch rolled plate and was ¼inch thick. The chemical composition of this plate material is: magnesium 4.7, manganese 0.9, iron 0.20, silicon 0.10, chromium 0.08, zinc 0.03, copper 0.03, titanium 0.01, and the remainder aluminum. Note that all the individual compositions are of weight percent (wt%). The American Bureau of Shipping certified the composition of this AA5083-H116 plate.[1]

2. Welding

Two plates of AA5083-H116 were cut in half parallel to the rolling direction of the plate material. The cut was made by a band saw with flowing lubricant to minimize any heat generation. The half sheets for each plate were then welded back together using a metal inert gas (MIG) weld at Carderock Division, Naval Surface Warfare Center (NSWCCD), see Table 2 for welding parameters. Each welded plate consisted of four passes, three on the top face of the plate and one along the root of the plate, see Figure 19. The plates were clamped to the welding table using L-shaped clamps. The welded areas were surface ground to remove any slag and debris.[1]

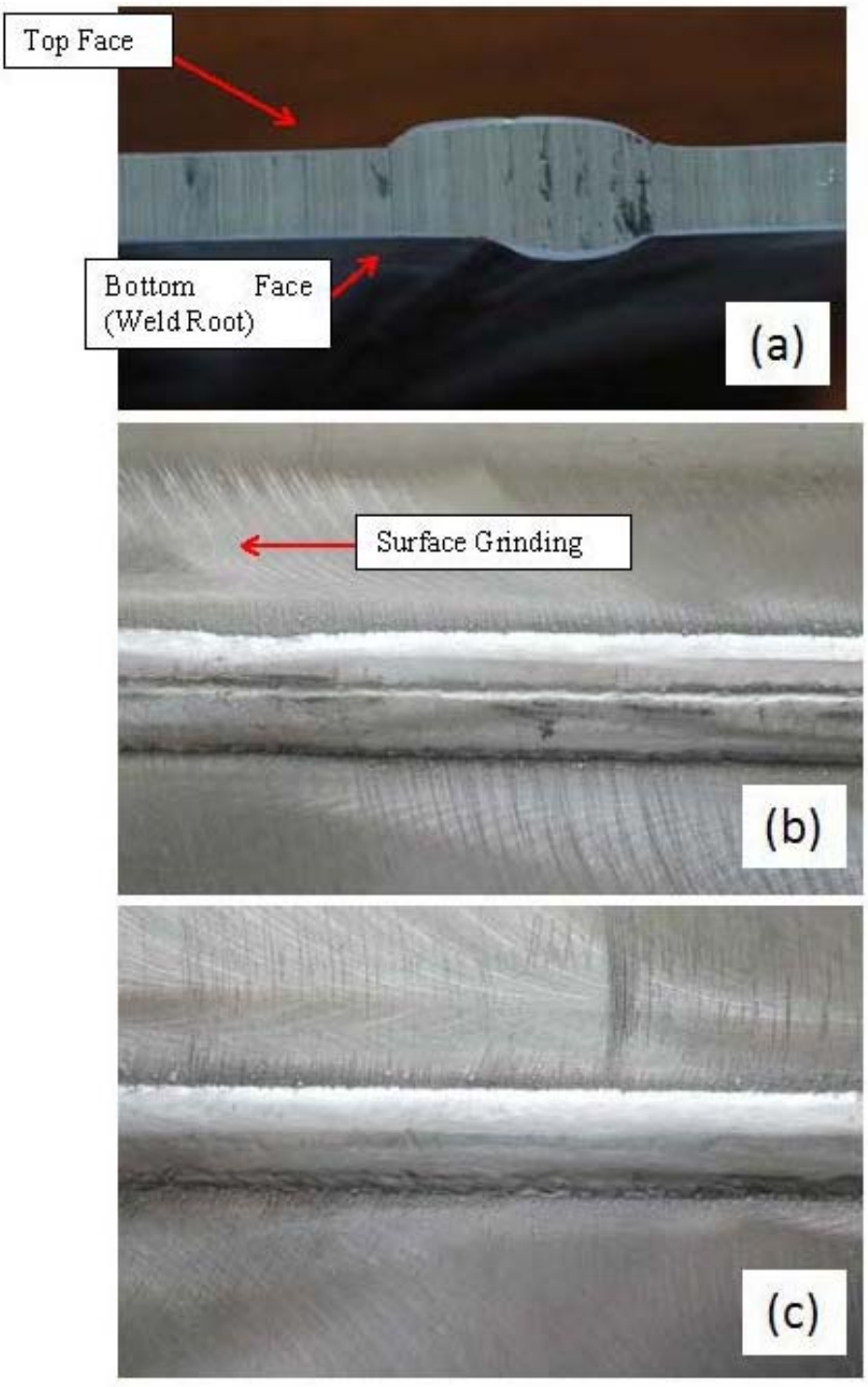

Figure 19. Welded Plate (a) side view (b) top face (c) bottom face (weld root).(From [1])

Pass	Volts	Wire Feed	Amps	Travel Speed (ipm)	Weld Time	Inter-pass Temp (F)	Remarks
1	23.9	273	121	17.4	1:16	69.6	Plate 1
2	25.1	336	136	17.4	1:15	118.3	
3	25.5	336	134	17.4	1:15	138	
4	25.1	336	138	17.4	1:14	72.9	Pass on the back of plate
1	23.7	273	122	17.4	1:15	69.8	Plate 2
2	25.4	336	134	17.4	1:15	120.8	
3	25.5	336	133	17.4	1:14	170.5	
4	24.9	336	139	17.4	1:16	72.3	Pass on the back of the plate

Table 2. Weld procedure from Carderock Division, Naval Surface Warfare Center (CDNSWC).(From [1])

B. LASER PEENING

1. Process

All laser peening (LP) was performed by the Metal Improvement Company (MIC) in Livermore, CA using a high-energy pulsed neodymium (Nd) glass laser. A typical laser peened specimen is shown in Figure 20. The welded plates were cut down into 2in wide strips, 6in long, centered off of the centerline of the weld. Two LP conditions were chosen for residual stress analysis: a "light" peening at condition 1-18-1, and a "heavy" peening at condition 3-27-2, as described in Table 3. The peening conditions were chosen to reflect different magnitudes of applied compressive stress. The layout of the peening process is shown in Figure 21. The laser beam that impacts the plate surface had a square cross section. The square laser footprint was translated along the plate surface. Percent overlap is the amount that one square overlaps the next square. For instance, Square 1 overlapped Square 2 by 10% for the 1-18-1 specimen and by 3% for the 3-27-2 specimen. LP was done on both faces of each specimen to keep the plate flat. The layout grouping shown in Figure 21 was chosen so that the weld nugget had

adequate coverage (i.e. the edge of the peening square lined up with the edge of the weld nugget so that there was not half a square on the weld nugget and half off of it) and was peened first before peening either side of the weld nugget; however, it is perfectly acceptable to peen continuously from one side of the specimen across the weld nugget and on to the other side (back-and-forth). While LP can be performed with or without tape, no tape was used on the specimens in this work. Using tape results in only a slight improvement in the surface finish for the laser peened material, but would not be practical for the future application to aluminum ship structures.[1]

Specimen	Irradiance (GW/cm^2)	Pulse Width (ns)	Layers (full coverage)	Percent Overlap (%)
1-18-1 (Light Peening)	1	18	1	10
3-27-2 (Heavy Peening)	3	27	2	3

Table 3. Laser peening conditions for experimental specimens. Provided by MIC.

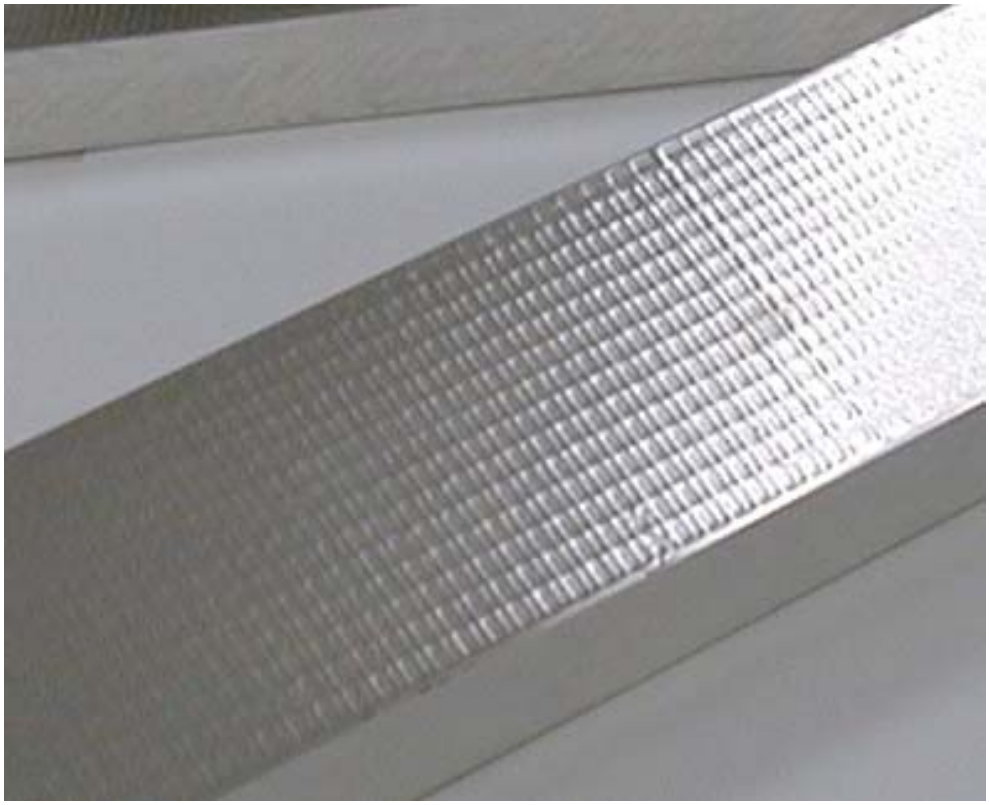

Figure 20. Typical laser peened specimen. Provided by MIC.

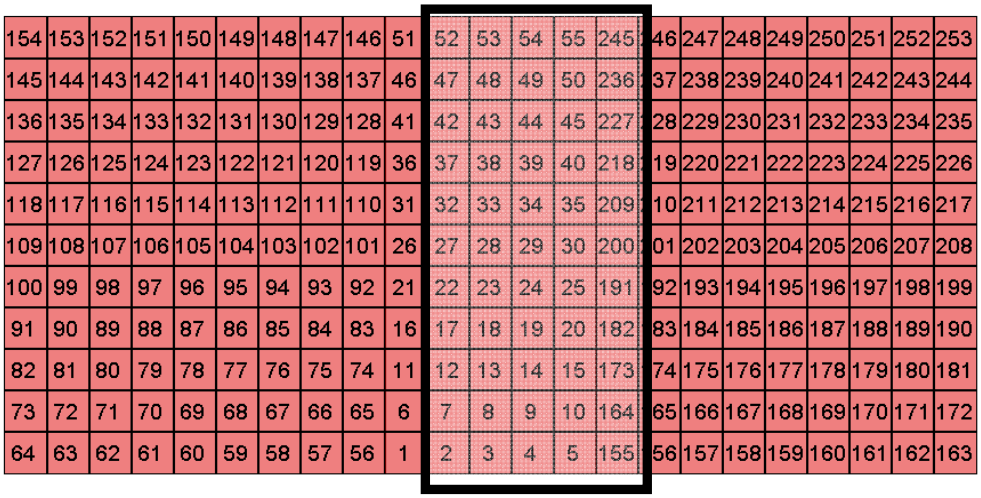

Figure 21. Laser peeing process layout: Group 1 in the middle along the weld nugget, Group 2 on the left side of the weld starting at the toe of the weld, and Group 3 on the right side of the weld starting at the toe of the weld. Provided by MIC.

C. ELECTRO-POLISHING

1. Process

Electro-polishing was used to measure residual stresses at various depths. A Proto Electrolytic Polisher Model 8818 (Figure 22) was used to electrolytically remove material to three different depths below the surface: 25.4□m (1mil), 254□m (10mil), and 508□m (20mil). This electro-polisher used a saltwater solution comprised of 81grams of salt (NaCl) per liter of distilled water. The machine was set to use 85volts and had a flow rate of 7 (arbitrary units). The depth of the polish depended on the amount of time the voltage was applied. The amount of time to depth removed had a linear relationship. The time to reach a particular depth is listed in Table 4.

Depth (□m)	Time (sec)
25.4	10
254	170
508	350

Table 4. Electro-polishing times to achieve a certain depth.

The specimen's surface was cleaned before electro-polishing because surface impurities can affect the quality of the electro-polished surface. Figure 23 shows the appearance of the plate surface after electro-polishing. The depth of the electro-polishing was found using a Mitutoyo height gauge (Model C112TB) holding a Mitutoyo deflector gauge (Figure 24). The gauge can measure to a precision of 2.54□m (0.1mil).

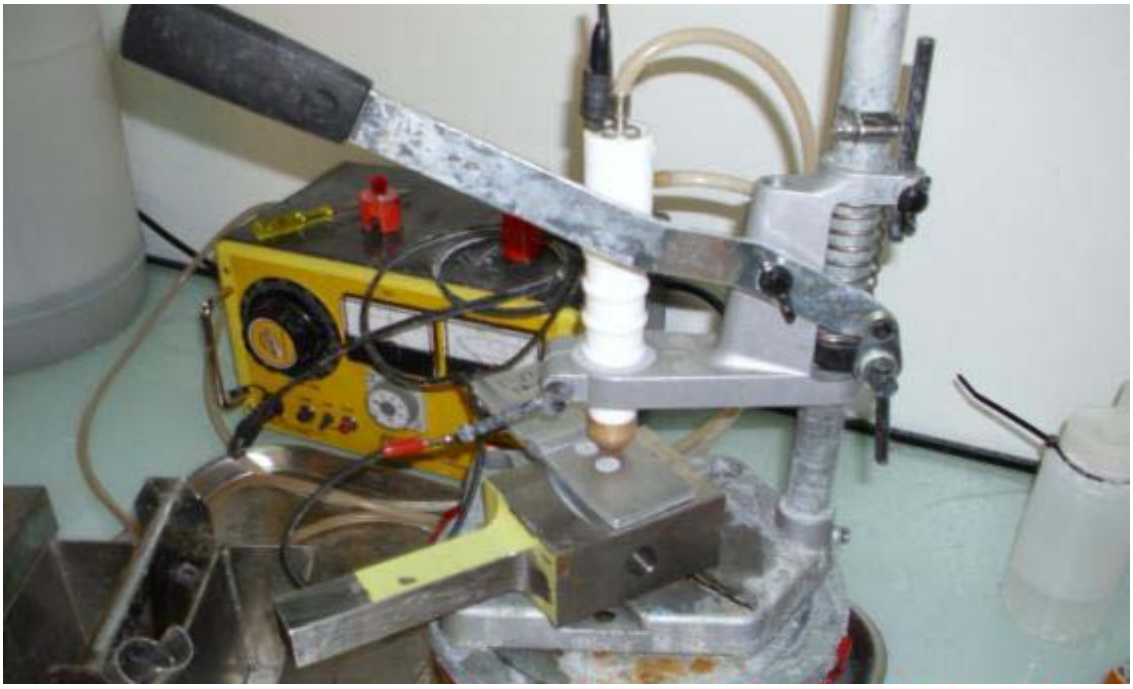

Figure 22. Proto Electrolytic Polisher Model 8818.

Figure 23. This picture shows the location and the size of electro-polishing done in this work. This is Specimen 3-27-2 after electro-polishing to a depth of 508□m (20mil) on the bottom side of the weld line.

Figure 24. Mitutoyo height gauge measuring the depth of how much material was removed during an electro-polish on specimen 3-27-2.

D. X-RAY DIFFRACTION

1. X-ray Diffraction Equipment Overview

Following the methods discussed in the introduction, x-ray diffraction (XRD) was used in this thesis to measure the elastic, residual strains and stresses as a function of welding and laser peening. The XRD equipment used in this work is a Proto Manufacturing Laboratory Non-Destructive Residual Stress Measurement System, LXRD model (Figure 25). It has a MG2000L goniometer that rotates the XRD goniometer in the ☐-direction. A separate mounting table rotates the specimen in the ☐-direction and can automatically move the specimen in the x and y directions through a mapping feature. The analysis software, XRDWin 2.0, is a windows based package that has the capability to analysis and display d vs. $\sin^2$☐ using a wide variety of curve fitting models for the peak profile analysis. An explanation for the experimental parameters used in this work will be covered in the following sections.

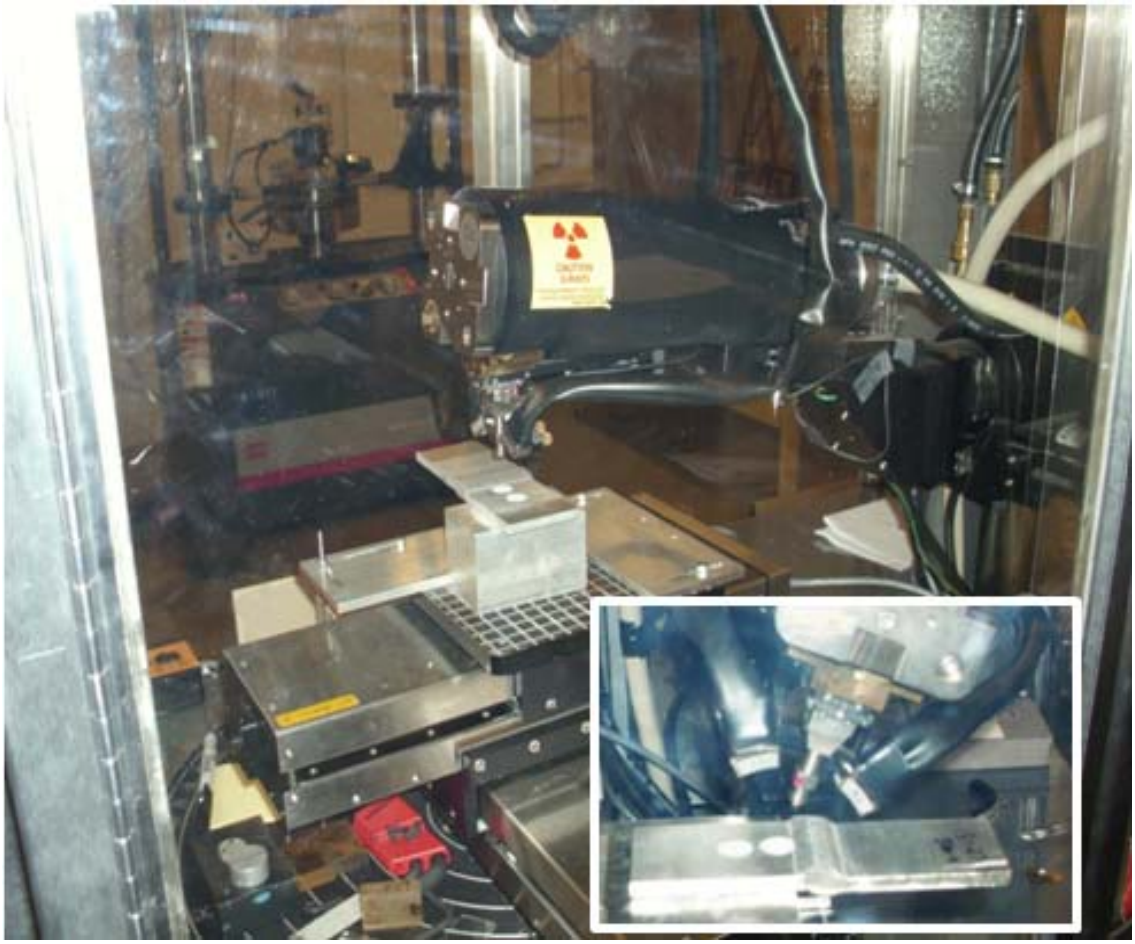

Figure 25. LXRD model used in this work with Specimen 3-27-2 being measured.

2. Specimen Set-up and Orientation

Each specimen was mounted on a metal block using a 2-part epoxy. This mounting arrangement was used to achieve a stable base for electro-polishing, to provide a stable reference height when measuring the depth of the electro-polish, and for placement in the XRD. The orientation of the mounted specimen was as follows: the x-axis was along (parallel to) the centerline of the weld, the y-axis was transverse (perpendicular to) the centerline of the weld, and ☐ rotated about the z-axis. A zero degree ☐ angle was specified when the goniometer axis of the XRD goniometer ran parallel to the x-axis of the specimen, see Figure 26. Positive ☐ and ☐ angels were in

the counterclockwise direction about the z-axis and about the goniometer axis (i.e. x-axis), respectively.

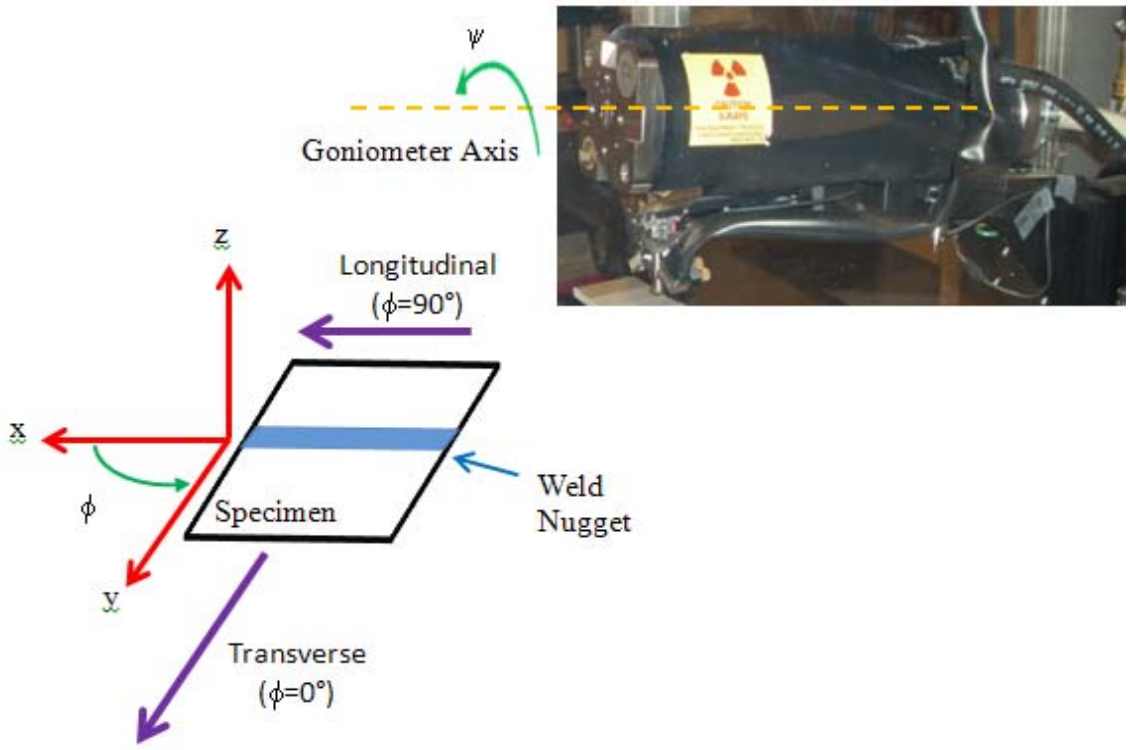

Figure 26. Specimen orientation with respect to the XRD goniometer. ☐=0 degrees is when the goniometer axis of the XRD goniometer is parallel to the x-axis of the specimen. Positive ☐ and ☐ rotations are in the counterclockwise direction about the z-axis and goniometer axis, respectively.

3. X-ray Tube Selection

The choice of the type of x-ray radiation to use is a balance between depth of penetration and availability of a sufficiently strong diffraction peak within the appropriate angular range for the x-ray diffractometer (Figure 27). The cobalt tube with Co-K☐ radiation was the best compromise between depth of penetration and Bragg angle (2☐ angle). This Co-K☐ radiation has a higher photon energy than Cr-K☐ radiation, thus achieving a deeper penetration. While Cu-K☐ radiation has an even greater depth of penetration, it does not have any Bragg angle reflections at appropriate angles for use

with the LXRD system. This work exclusively used the cobalt tube with Co-K□ radiation for all measurements.

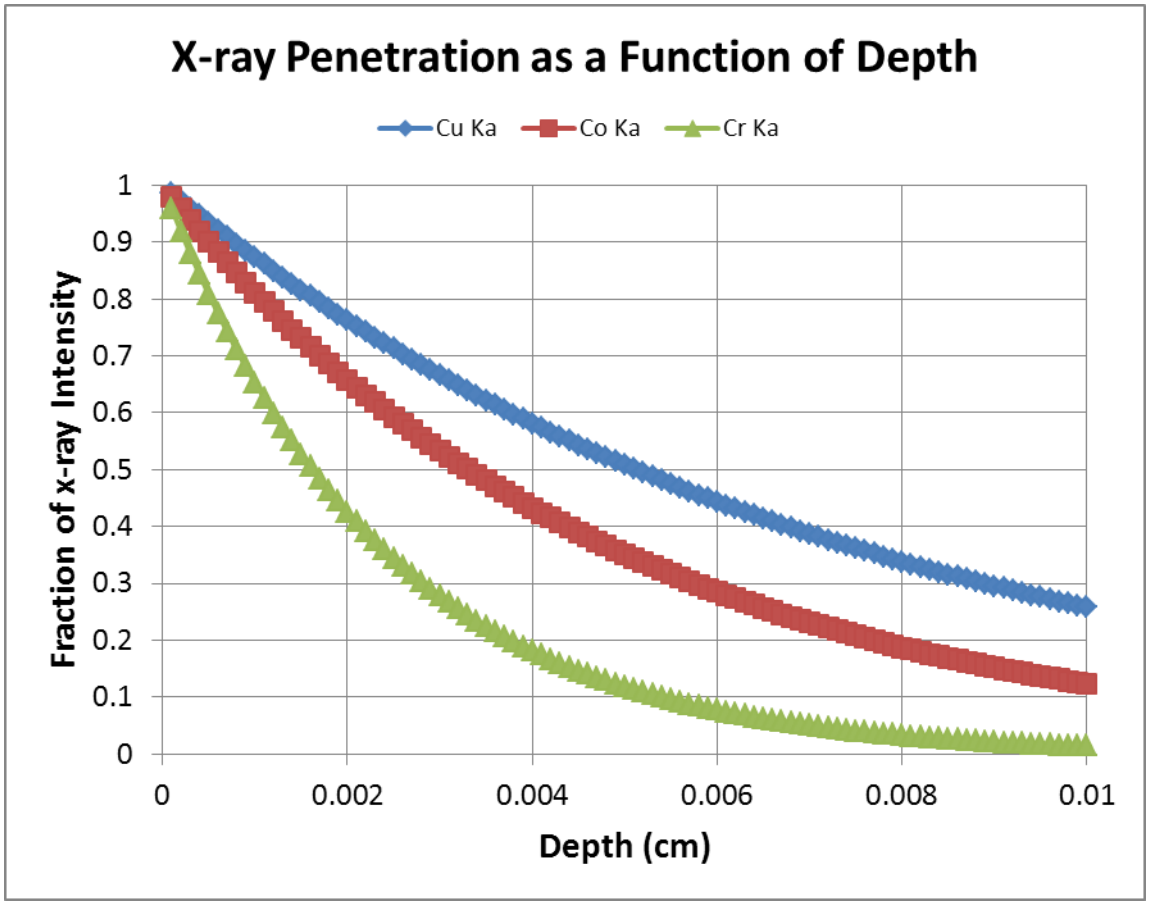

Figure 27. Absorption of x-rays as a function of depth for common x-ray tube types.

4. Reflection Selection

Based on the tube selection the diffraction plane can then be determined. Since the cobalt tube was used the {400} to {420} reflections would be acceptable for the diffraction measurement (see Table 1). It is of note that the higher the Bragg angle (2□ angle) means more accurate strain measurements. The {420} reflection would be the prime candidate to use for these measurements. The first data set utilized the {420} reflection to measure the as-peened surface of the specimens, but was not further pursued because it would not have a direct comparison to previous {331} reflection results. The {400} reflection was not supported by the XRDWin 2.0 software and could not be

measured because it had too low of a Bragg angle. The {331} reflection was ultimately chosen because it was one of two reflections that the software had available for analysis and corresponded to previous reported results.

5. ψ Angle Selection

Angles of □ were chosen to give a symmetric and wide range of $\sin^2$□ values when viewed on a d vs. $\sin^2$□ plot. The x-ray diffractometer used single-exposure technique at multiple □-tilts with two position sensitive detectors. Figure 28 shows how the position sensitive detectors capture the diffracted radiation per this experimental set up. This work selected values of $\sin^2$□ ranging from about 0.0 to 0.5. Angles of □ were calculated from Equations 18; however, the XRDWin 2.0 software only uses □ angles to position the XRD goniometer. The angle between the x-ray source and the normal to the specimen surface is the□□ angle, see Figure 28. Knowing the chosen □ values and the Bragg angle for the {331} reflection, □ angles were calculated by rearranging Equation 18. Note that Co-K□ radiation has a wavelength of 0.179026nm and using the {331} reflection of aluminum, which is faced-centered cubic, the lattice parameter, a, is 0.40497nm and the Miller indices of h=3, k=3, and l=1 resulting in a 2□ of 148.93 degrees.[20]

$$\psi_{1,2} = \beta \mp \left(\frac{\pi - 2\theta}{2} \right) \tag{18}$$

The 2□ value used for all specimen measurements was rounded up to 149 degrees. □ angles were calculated for each experiment based upon the desired □ range. The XRDWin 2.0 software needed a minimum of eleven □ angles per each position detector in order to calculate the stresses at a given location. □ angles cannot exceed +/-35

degrees. The effects from texturing can be reduced by oscillating in the ☐ direction, so proper caution needs to be taken in calculating ☐ and ☐ angles. An example of the ☐ and ☐ angles used in the d vs. $\sin^2$☐ stress analysis are listed in Table 5 for detector 1 and detector 2 of the {331} reflection. Note that the bottom seven rows of detector 1 and the top seven rows of detector 2 were combined to form a single d vs. $\sin^2$☐ plot as shown in Figure 29. Additional calculations of converting ☐ to ☐ and ☐ to ☐ angles are listed in the Appendix.

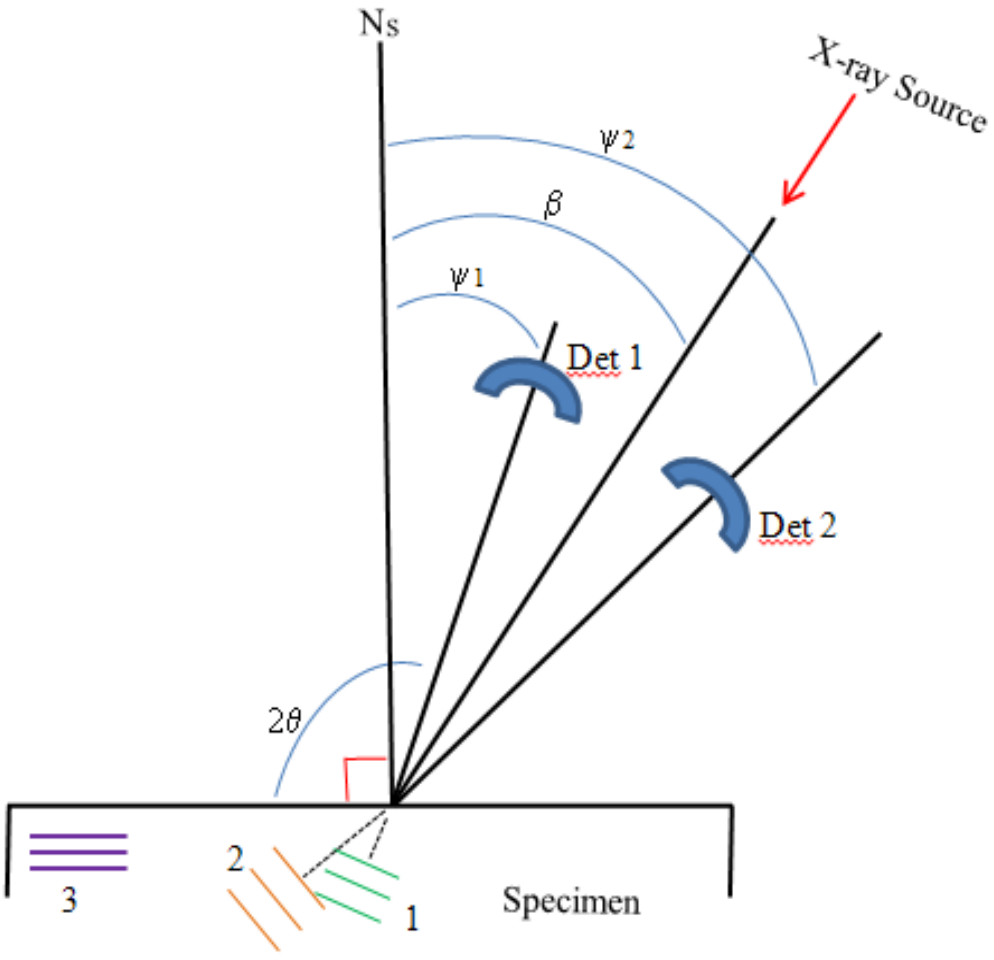

Figure 28. Specimen and detector layout used for determining ☐, $☐_1$, and $☐_2$ angles, and for visualizing how the different lattice planes of the specimen are being measured.

Detector 1	
☐	☐
29.5	14
24.5	9
22	6.5
19.5	4
14.5	-1
9.5	-6
-14.5	-30
-19.5	-35
-22	-37.5
-24.5	-40
-29.5	-45

Detector 2	
☐	☐
29.5	45
24.5	40
22	37.5
19.5	35
14.5	30
9.5	25
-14.5	1
-19.5	-4
-22	-6.5
-24.5	-9
-29.5	-14

Table 5. Typical experimental ☐ and ☐ angles for detector 1 and detector 2 for the {331} reflection used for the collection of residual strain data. The highlighted rows from each detector were combined together to form the data point along the x-axis on a single d vs. $\sin^2$☐ plot, see Figure 29.

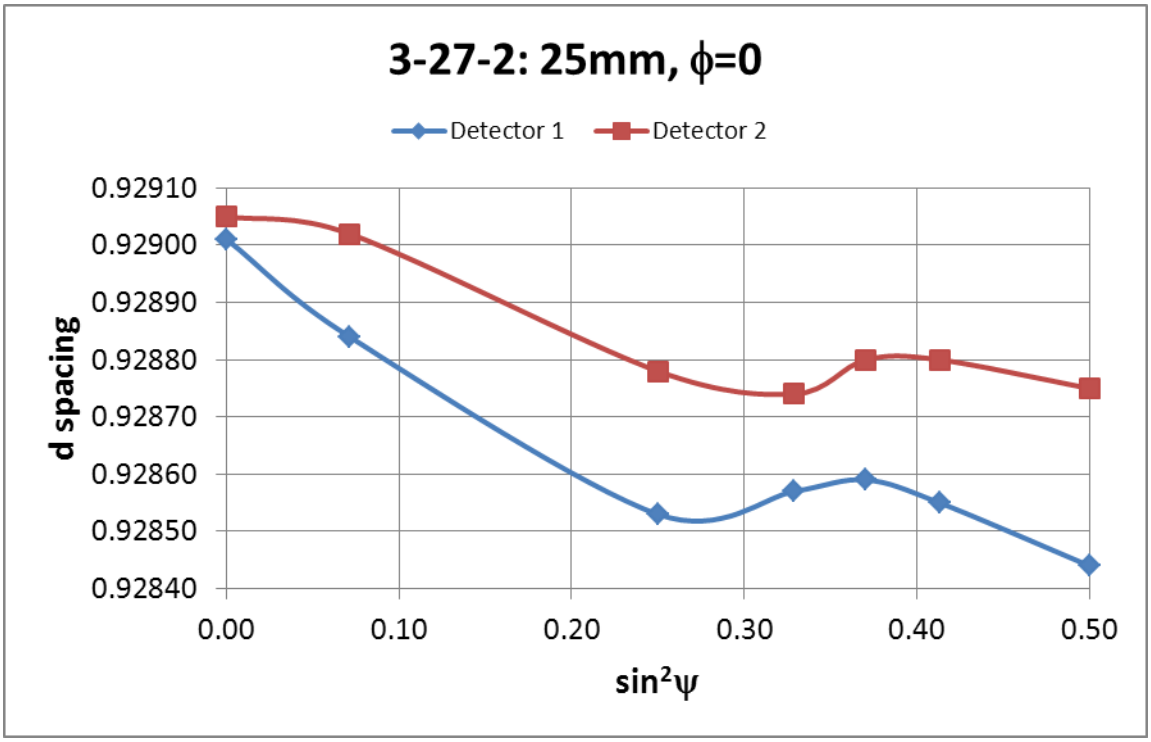

Figure 29. d vs. $\sin^2\square$ plot of specimen 3-27-2 at 25mm distance from the weld toe at $\square$=0 degrees for the {331} reflection highlighting how the combination of detector values are plotted.

6. Additional XRD Set-up Parameters

The following set-up parameters were used in all measurements except where noted. All experimental and calibration measurements used a 2mm aperture, no K-β filters, an 80% Gaussian fit for peak location, power of 25KV, and current of 20mA. An 80% Gaussian fit was chosen in order to coincide with the same parameters used in previously reported results. A Gaussian fit is a mathematical procedure to approximate the peak shape in order to find the centroid of the profile peak. It used the top 80% of the profile peak for its calculations. Note that the higher the voltage and current, the more x-rays are produced resulting in higher diffracted intensity and better signal to noise ratio. There were no oscillations in the x, y, and ϕ direction. In the "Peak Shift Methods" settings were set to an "Absolute Peak" with a "P/G Profile" and "LPA Corrections". The "Absolute Peak" measured the tallest peak profile while the "P/G Profile" setting

divided the raw data profile, P, by the background gain profile, G. The "LPA (Lorentz-Polarization-Absorption) Correction" adjusts the profile shape and intensity to correct for the Lorentz-polarization factor and absorption factor. The calibration process for both the high stress and low stress standards used five degrees of ψ oscillation, ten exposures per the eleven ψ angles, two seconds per exposure, and a 2θ=148.94 degrees. On the other hand, experimental measurements used three degrees of ψ oscillation, 20 exposures per the eleven ψ angles, two seconds per exposure, and a 2θ=149 degrees. Note that this work used a larger exposure number to increase accuracy of the measurements. All other set-up parameters were set to default values. The lab technician manually set the focusing length of the goniometer for each measurement, and adjusted the gain voltage as necessary to properly identify the background and divide it from the profile for each calculation of the measurement's profile peak.

E. EXPERIMENTAL MEASUREMENTS

1. "d vs. $\sin^2\psi$" Stress Measurement Process

Four data sets were taken using the d vs. $\sin^2$□ technique where each data set had slightly different experimental and set-up parameters. Before each data set was taken a machine calibration was conducted to ensure that any measurement errors generated were within specified tolerances. Two aluminum based standards were used to validate the precision and accuracy of the XRD. One was a low stress standard having zero stress (0.00 +/-13.8MPa), and the other was a high stress standard having a compressive stress of -232 +/-35MPa. The calibration process uses the default □ and □ angles as listed in Table 6. The residual stresses for each specimen (1"-wide control, 1-18-1 and 3-27-2) were measured using the following criteria: 1) at □=0 degrees stresses were measured perpendicular to the weld centerline; and 2) at □=90 degrees stresses were measured parallel to the weld centerline for all four data sets. Data set one measured the bi-axial residual stresses of the as-peened surface at locations at 2, 4, 6, and 8mm from the weld toe, see Figure 30. These data points were selected to measures the residual stresses of

the HAZ of specimens 1-18-1 and 3-27-2. The 1" control sample had an additional test location at 10mm from the weld toe to define the value of the residual stress in the base metal; however, this test point was moved to 25mm from the weld toe in future data sets because it could not be asserted that the material's structure at 10 mm was the base metal. This first data set utilized the {420} reflection. The second data set measured the bi-axial residual stresses at 2, 4, 6, 8, and 25mm distances from the weld toe at a depth of 25.4□m (1mil) on all specimens (1" control, 1-18-1 and 3-27-2). During this experimental run it was determined that there was too much over-lap of the test locations in the HAZ. Having a 2mm interval between test points and a 2mm aperture with three degrees of oscillation, there was extra coverage from one data point to the next, which resulted in too much redundancy; therefore, one data point (6mm) was selected to represent the HAZ in future measurements. The third and fourth data sets consisted of measuring the bi-axial residual stresses at 6 and 25mm distances from the weld toe at depths of 254□m (10mil) and 508□m (20mil), respectively, for all specimens (1" control, 1-18-1 and 3-27-2). The second, third, and fourth data sets utilized the {331} reflection, and the all the associated □ angles for each experimental run are listed in the Appendix.

	Detector 1	Detector 2
□	□	□
30.00	14.47	45.53
23.46	7.93	38.99
19.00	3.47	34.53
9.51	-6.02	25.04
0.73	-14.80	16.26
0.00	-15.53	15.53
-0.73	-16.26	14.80
-9.51	-25.04	6.02
-19.00	-34.53	-3.47
-23.46	-38.99	-7.93
-30.00	-45.53	-14.47

Table 6. □ and □ angles of detector 1 and detector 2 used for calibrating the XRD with the high and low stress standards.

A way of determining the amount of residual plastic *strain* in a material is by analyzing the full width at half maximum (FWHM) of the diffraction peak. The diffraction peak shape for a single crystal would look like a sharp line, having only the width of the resolution capability of the diffractometer. A polycrystalline structure that has been cold-worked displays a broader diffraction peak. Peak broadening analysis of several Bragg peaks can be used to calculate the crystallite size and strain.[20] Laser peening deforms the work piece much in the same manner as cold-working; therefore, the heavier the laser peening, the more plastic deformation, the more non-uniform strain that is introduced in the crystal lattice, and the broader the diffraction peak.

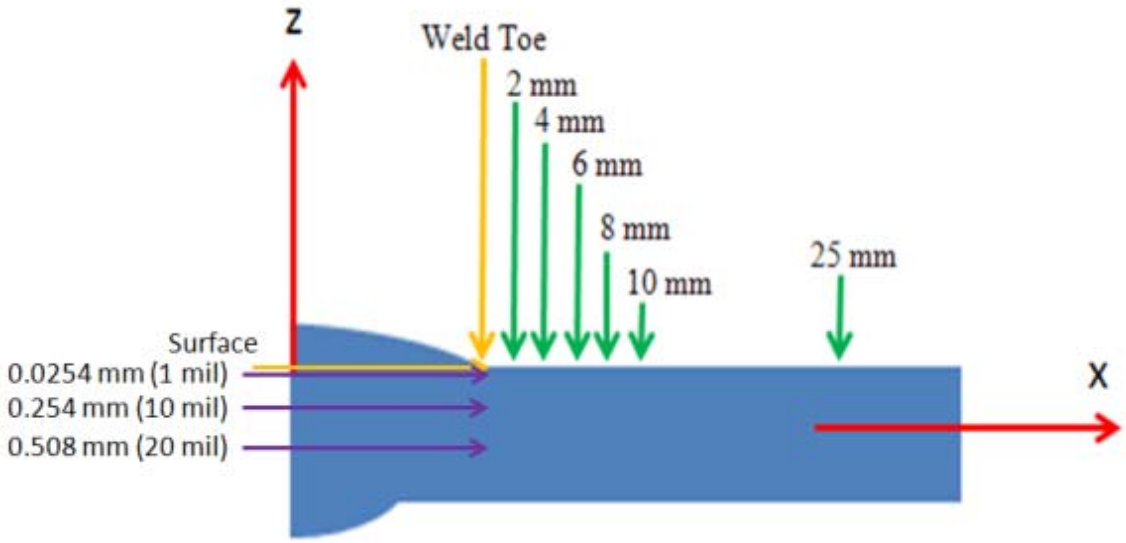

Figure 30. Locations of experimental test points on the one inch control, 1-18-1, and 3-27-2 specimens.

2. Tensor Measurement Process

Two different sets of tensor measurements were performed at 6mm and 25mm distances from the weld toe at three different depths, 25.4, 254, and 508μm (1, 10, and 20mil), respectively. The first tensor measurement set was conducted at depths of 25.4 and 254μm, and the second tensor measurement set occurred at depths of 254 and 508μm. Both tensor measurements sets used all the same set-up parameters as the second d vs. $\sin^2\psi$ method data set, only the ψ and ϕ angles were changed, see Table 7. Six independent sets of ψ and ϕ angles were taken at each test point at each depth, except for the 6mm test point at 508μm depth on specimens 1-18-1 and 3-27-2 where no data was collected. Additionally, the number of exposures was cut in half to ten on specimens 1-18-1 and 3-27-2 at the 25mm test point at a depth of 508μm. The following material constants, as quoted from the high stress standard, were used to solve for the stiffness matrix: 1) high stress standard: E=71.102GPa and ν=0.33; and 2) specimens (one inch control, 1-18-1, and 3-27-2): E=70.3GPa and ν=0.33.[6,21] The d_0 values were determined from the d spacing measurement at ψ=0 and ϕ=0 degrees, and resulted in the following: 1) 0.09289142nm for the AA5083 specimens; and 2) 0.09290492nm for the

aluminum high stress standard. Note that one tensor measurement was taken on the 1-18-1 specimen at 6mm from the weld toe at a depth of 25.4μm using ψ and ϕ angles of +/-45.00, +/-37.50, and +/-30.00 degrees.

First Tensor Data Set Angles	
□	□
-45	-15
-37.5	-10
-30	-5
30	9
37.5	13
45	17

Second Tensor Data Set Angles	
□	□
-45	-65
-40	-35
-30	-15
25	5
30	45
45	55

Table 7. □ and □ angles used for tensor data sets one and two.

III. RESULTS AND DISCUSSION

A. CALIBRATION RESULTS FOR "d vs. $\sin^2\psi$"ANALYSIS

Calibration of the XRD prior to each set of measurements demonstrated the accuracy and precision of the system. Following the d vs. $\sin^2\psi$ analysis approach, the stress determined by the system was found to be -245.35±4.30MPa compared with the known bi-axial stress of -232±35MPa for the high stress standard (Figure 31). The low stress value measured by the system was -2.58±3.89MPa compared with the low stress standard value 0.00±13.79MPa. The values for each calibration for the {331} reflection can be found in Table 8. Referring back to Equation 17, the stress in the ϕ-direction using the slope, m, from the d vs. $\sin^2\psi$ plot becomes Equation 19, which is used for isotropic materials.[20,21]

$$\sigma_\phi = \frac{mE}{(1+\nu)d_0} \qquad (19)$$

The stress of the high stress standard calculated in this manner is -247.42MPa, which is in good agreement with the known value and verifies the d vs. $\sin^2\psi$ technique. As discussed in the introduction, d_0 can be replaced by the lattice spacing measured at ψ=0 resulting in less than 0.1% of the final stress value.[20,21].

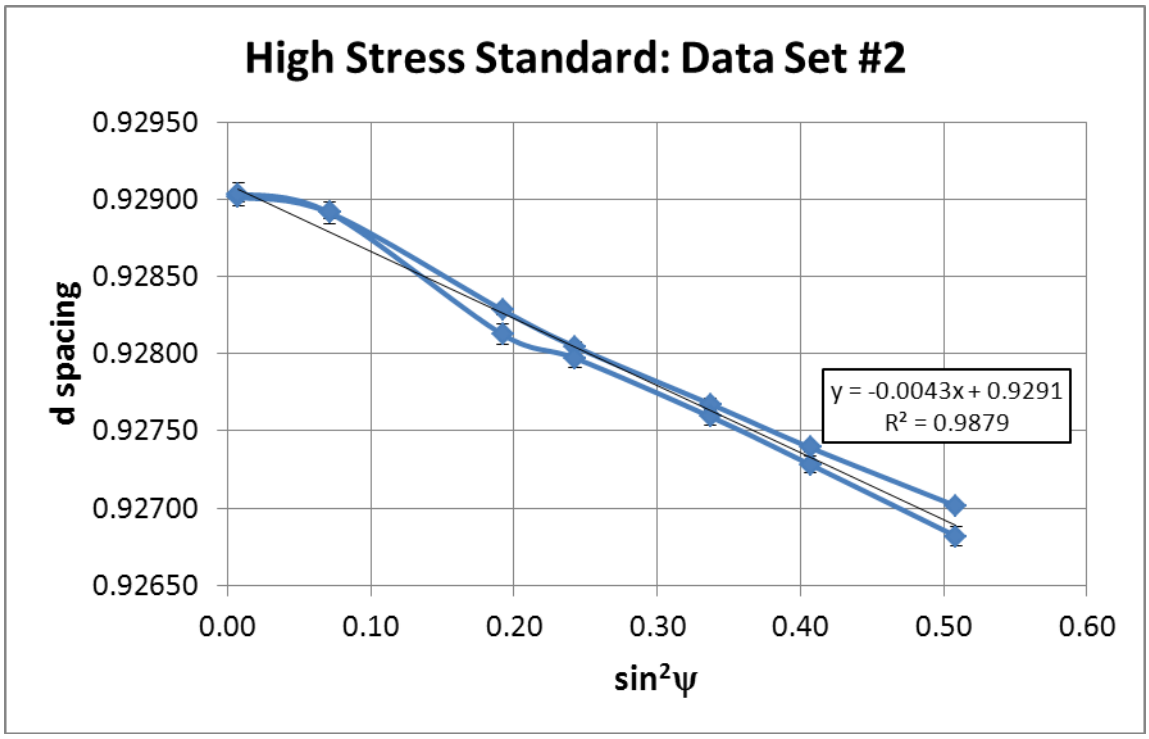

Figure 31. Average of five measurements on the high stress standard results for data set #2. Error bars represent ± one standard deviation.

(a) Data Set #2

Low Stress Calibration	Stress (MPa)	(+/-)
1	-4.14	3.79
2	-4.34	3.79
3	-3.86	4.34
4	1.17	3.31
5	-1.72	4.21
average	-2.58	3.89

High Stress Calibration	Stress (MPa)	(+/-)
1	-244.30	3.76
2	-244.29	4.19
3	-245.46	5.28
4	-246.50	4.30
5	-246.21	3.95
average	-245.35	4.30

(b) Data Set #3

Low Stress Calibration	Stress (MPa)	(+/-)
1	-6.14	4.34
2	-7.52	4.90
3	-5.17	4.41
4	-4.69	4.48
5	-5.10	4.41
average	-5.72	4.51

High Stress Calibration	Stress (MPa)	(+/-)
1	-260.57	4.17
2	-259.16	3.97
3	-257.88	3.96
4	-260.63	5.60
5	-258.06	4.12
6	-255.14	4.60
average	-258.57	4.40

(c) Data Set #4

Low Stress Calibration	Stress (MPa)	(+/-)
1	2.34	4.34
2	-1.52	4.27
3	-2.21	3.93
4	-4.34	3.24
5	-0.55	3.79
average	-1.25	3.92

High Stress Calibration	Stress (MPa)	(+/-)
1	-249.88	3.12
2	-240.83	3.36
3	-252.17	5.32
4	-250.95	3.01
5	-245.22	2.89
6	-244.17	4.25
average	-247.20	3.69

Table 8. Calibration data for the low and high stress standards for data sets #2, #3, and #4.

B. RESIDUAL STRESSES USING "d vs. $\sin^2\psi$"ANALYSIS

1. Control Weld Results

The residual stresses at the surface of the control specimen showed an increase in tensile stress up to 10mm away from the weld toe (Figure 32 and Figure 33). The error bars in the plots of this section and from here on out were determined by the error analysis embedded in the XRDWin 2.0 software. The residual stresses transverse to the weld line started out compressive and finished at approximately a zero stress state 25mm from the weld toe. The residual stresses longitudinal to the weld line started out slightly tensile, between 0 to 5MPa, and became more tensile at a value around 15MPa at 8mm from the weld toe before decreasing slightly at 10mm distance.

These stress profiles are consistent with what should be expected for this welding geometry. As was observed in the work of James et al.[10], the maximum in tensile stresses parallel to the weld line occurs several millimeters away from the weld toe. The stress maximum in the work by James et al. occurred between 10–12mm away from the weld toe (Figure 8). The magnitude of the stress in their work was about 4–5 times larger than the current results; however, they did not surface grind after welding. The welds in this thesis were surface ground before laser peening as can be seen in Figure 19. The surface grinding will impart a compressive stress into the surface. As stresses are additive, the compressive stress from the surface grinding will reduce the tensile stresses from the thermal contractions during welding, resulting in a smaller tensile stress along the weld line as observed in Figure 33.

The transverse stress profiles in the work of James et al. also agreed with the current results at the surface, but differed as a function of depth.[10] Their results for a depth of 1mm from the surface showed a profile which began at near zero stress at the weld toe and the increased to around 25MPa at 10mm from the weld toe. The transverse stresses at 4 and 7mm depth, started at around +40MPa and decreased to around +25MPa at 10mm from the weld toe. The trend in the current results shows a compressive stress of approximately -20MPa at the weld toe, rising to near zero stress 10mm away from the

weld toe. The difference between this result and that of James et al. (1mm depth) is likely due to the surface grinding use on the welds in this thesis.

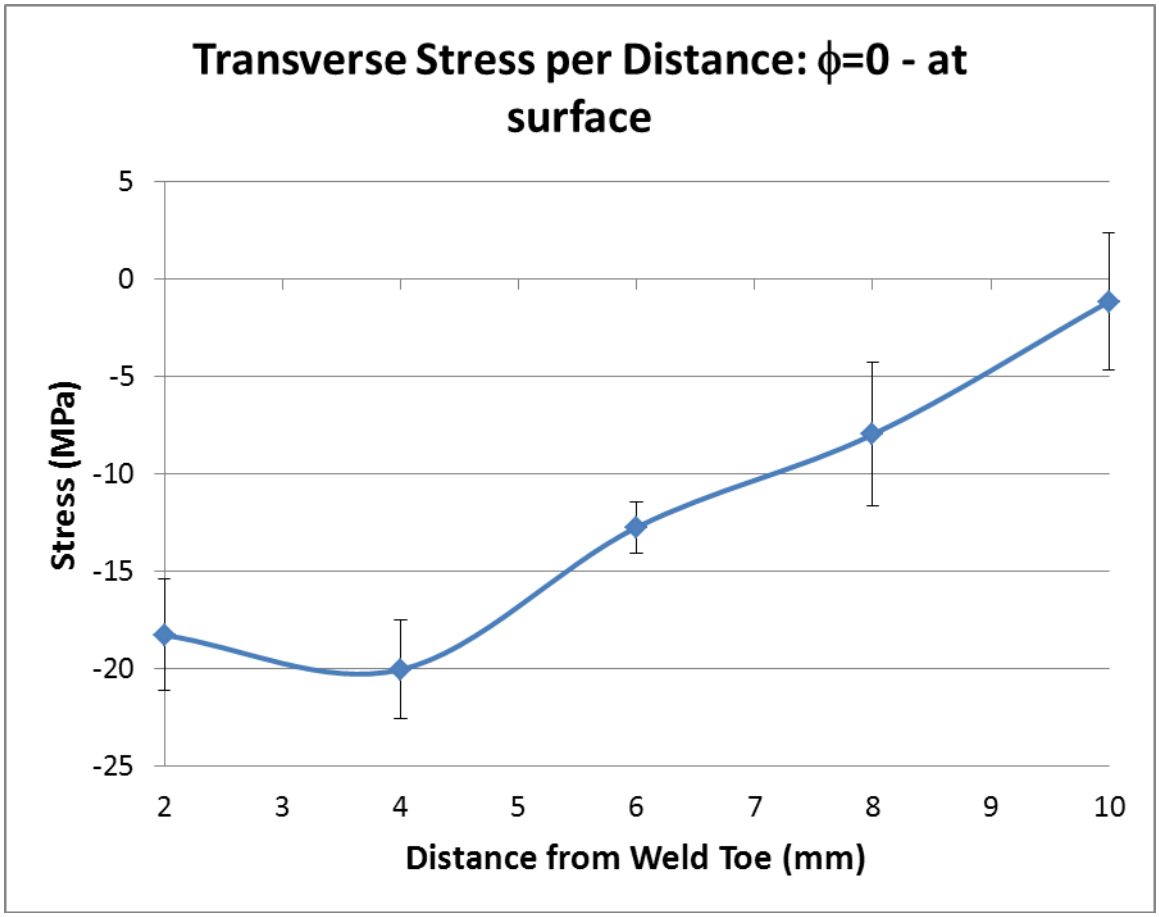

Figure 32. Transverse residual stresses as a function of distance from the weld toe in the control specimen at the surface.

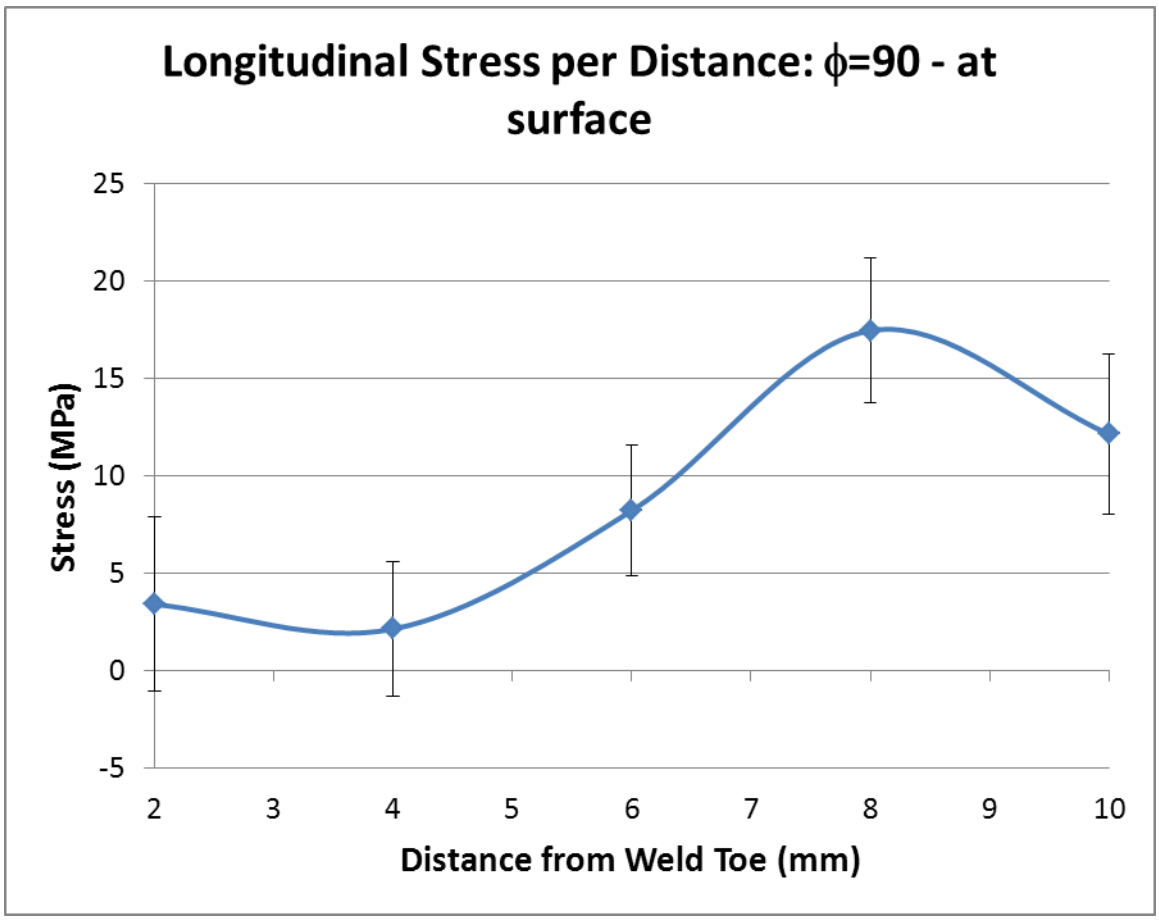

Figure 33. Longitudinal residual stresses as a function of distance from the weld toe in the control specimen at the surface.

The residual stresses on the control weld specimen showed little variation in stress value as a function of depth for either the transverse and longitudinal orientations (Figures 34 through Figure 37). In the work of James et al., the longitudinal stresses showed no measurable variation with depth, while the transverse stresses were measurably more tensile as depth increased.

Interestingly, the variation of residual stress with depth was notably different in the base-plate material (25mm away from the weld toe). The longitudinal stresses again did not meaningfully vary with depth (Figure 37), but the transverse stresses varied systematically with depth (Figure 36). The transverse stresses near the surface were much more compressive (-35MPa) than 0.5mm below the surface (nearly zero). Note that there were no actual surface measurements at the 25mm test point, but measurements

were taken at 0.0254mm (1mil) below the surface. This result compares with the work of Nakayama et al., which used x-ray diffraction to study the residual stress distributions present after cold-rolling of AA5083. In this work there was a definite difference between the longitudinal and transverse residual stresses. The comparison between this work and Nakayama et al. was that the longitudinal stresses were always larger than the transverse stresses, and that there was a stress gradient in the out-of-plane direction. Both studies demonstrate that the rolling direction does matter in evaluating residual stresses.[26]

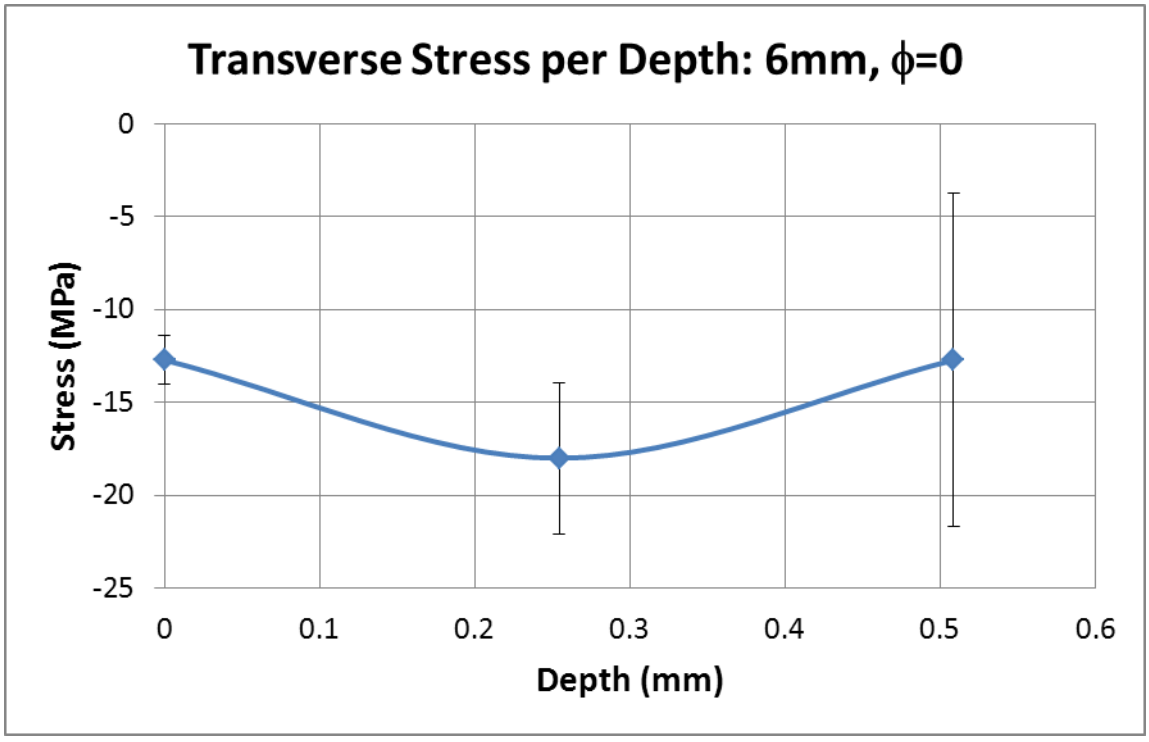

Figure 34. Transverse residual stresses as a function of depth in the control specimen at the 6mm test point.

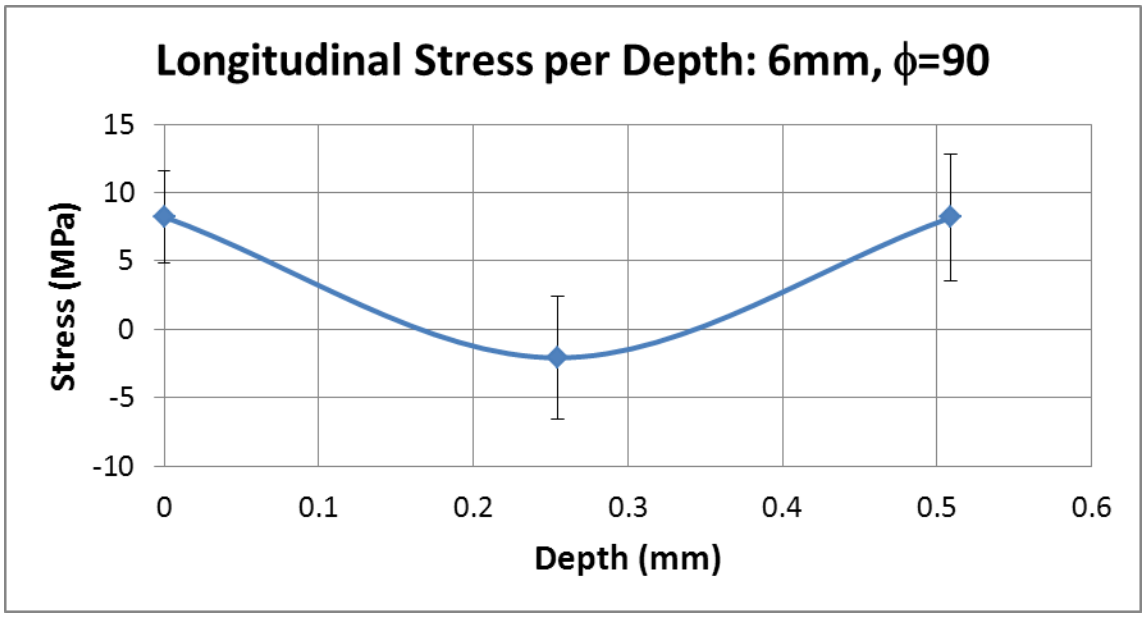

Figure 35. Longitudinal residual stresses as a function of depth in the control specimen at the 6mm test point.

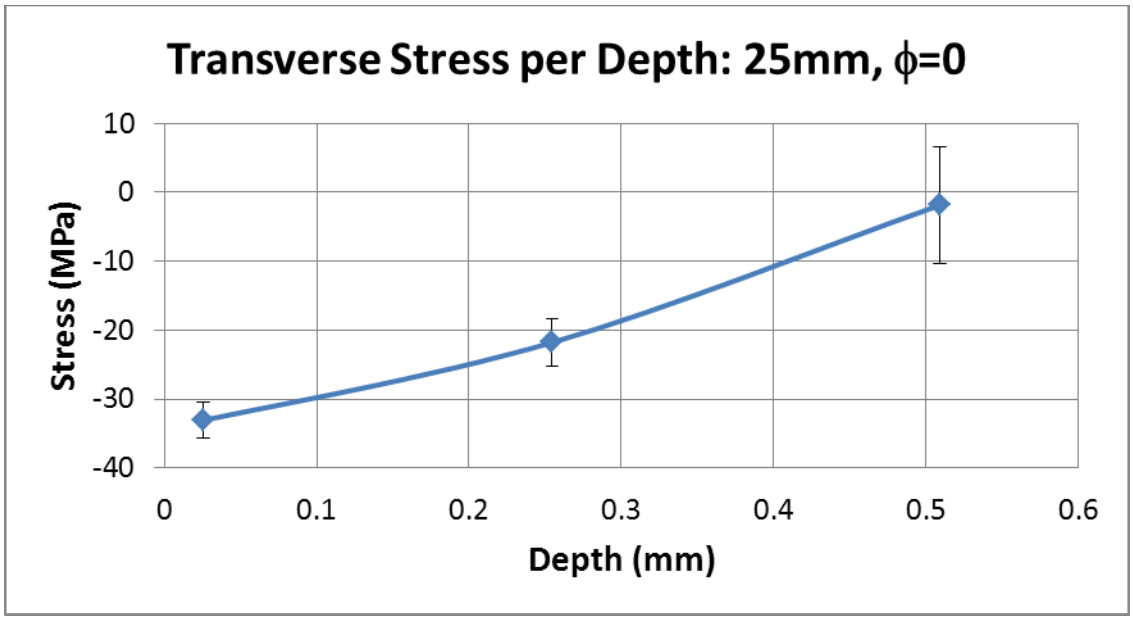

Figure 36. Transverse residual stresses as a function of depth in the control specimen at the 25mm test point.

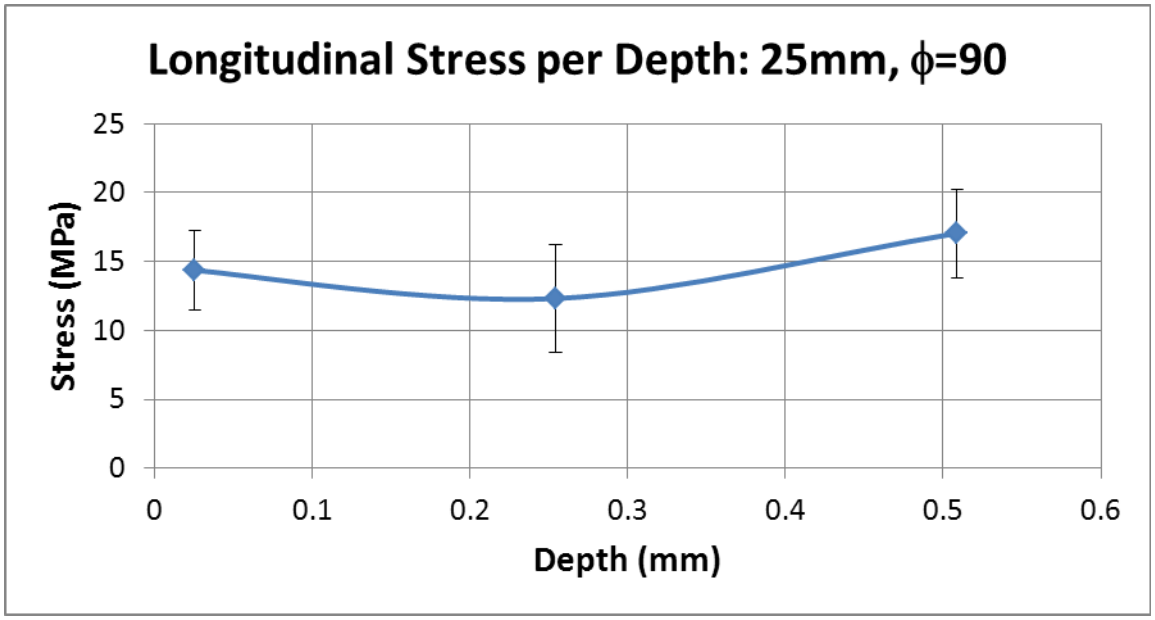

Figure 37. Longitudinal residual stresses as a function of depth in the control specimen at the 25mm test point.

2. Residual Stress Distribution after Laser Peening

The surface residual stresses as a function of distance from the weld toe after laser peening at the surface showed a noticeable compressive residual stress after 4mm from the weld toe in both the transverse and longitudinal directions for both the 1-18-1 and 3-27-2 conditions (Figure 38 and Figure 39). The tensile stresses on the laser peened specimens at the surface are most likely the remnants of a tensile crust leftover from the laser peeing because a sacrificial layer of tape was not used.

Both laser peening conditions produced a larger compressive stress than observed from the surface-ground weld alone. However, the detailed stress profiles for the two peening levels do not show a systematic trend. The heavier peened specimen, 3-27-2, produced a greater compressive residual stress at 6mm in both directions; however, at the 4mm and 8mm test points the lighter peened specimen, 1-18-1, had the larger compressive residual stress. The details of the microstructure orientation may be playing an important role in the relative level of the residual stresses. The stresses after laser peening were significantly larger in the transverse direction than in the longitudinal direction. Although some of this difference may be due to the difference in the stresses

from the welding itself, it is also quite likely that plastic anisotropy stemming from the rolled microstructure of the plate material may cause more plastic deformation in the transverse direction; and therefore, a larger degree of compressive residual stress.

The complexity in the surface residual stress profiles after laser peening does resemble results from the work of Hatamleh et al.[32] Figure 40 shows almost a parabolic increase in the compressive residual stress as a function of distance from the weld centerline in both the longitudinal and transverse directions. The single layer laser peening specimen, 1-18-1, follows this trend where there is a growing compressive residual stress as the distance from the weld toe increases in both the transverse and longitudinal directions.

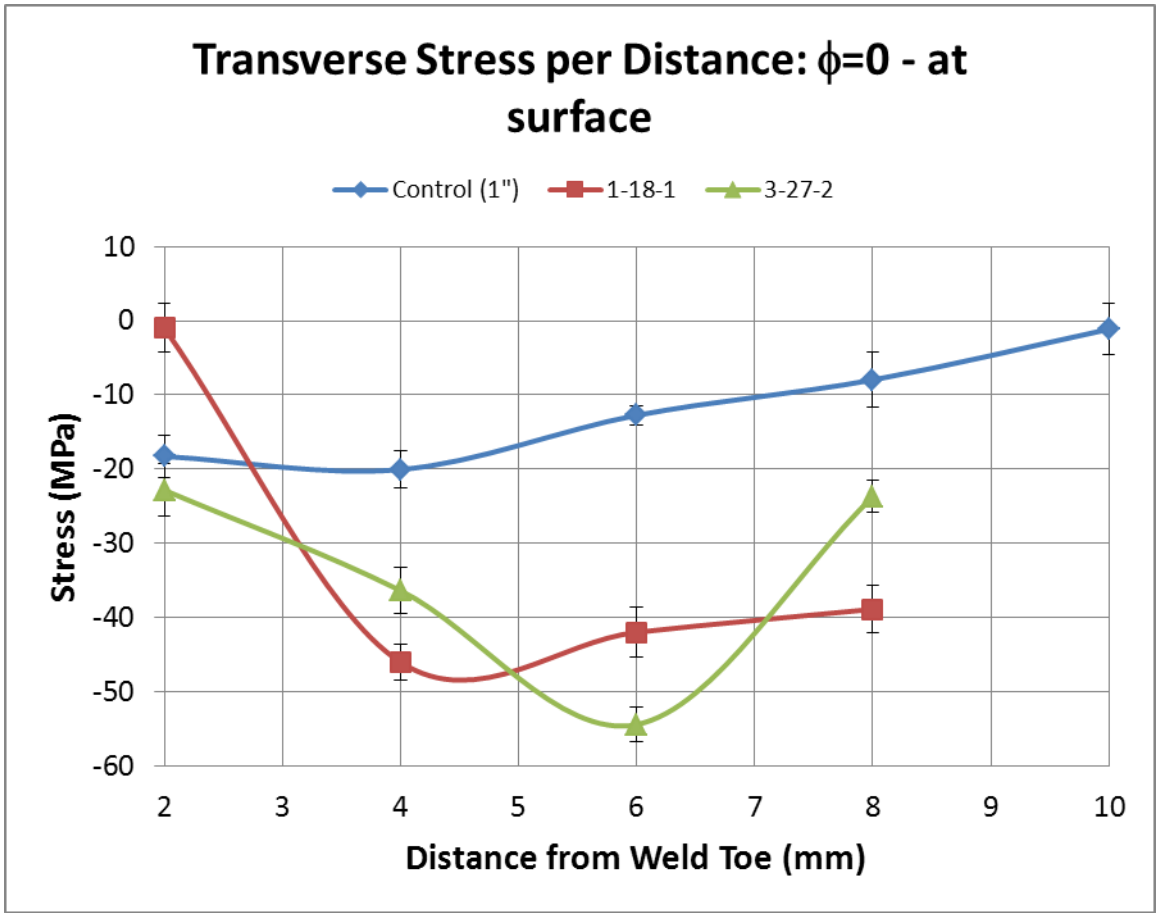

Figure 38. Transverse residual stresses as a function of distance from the weld toe in the 1-18-1 and 3-27-2 specimens at the surface.

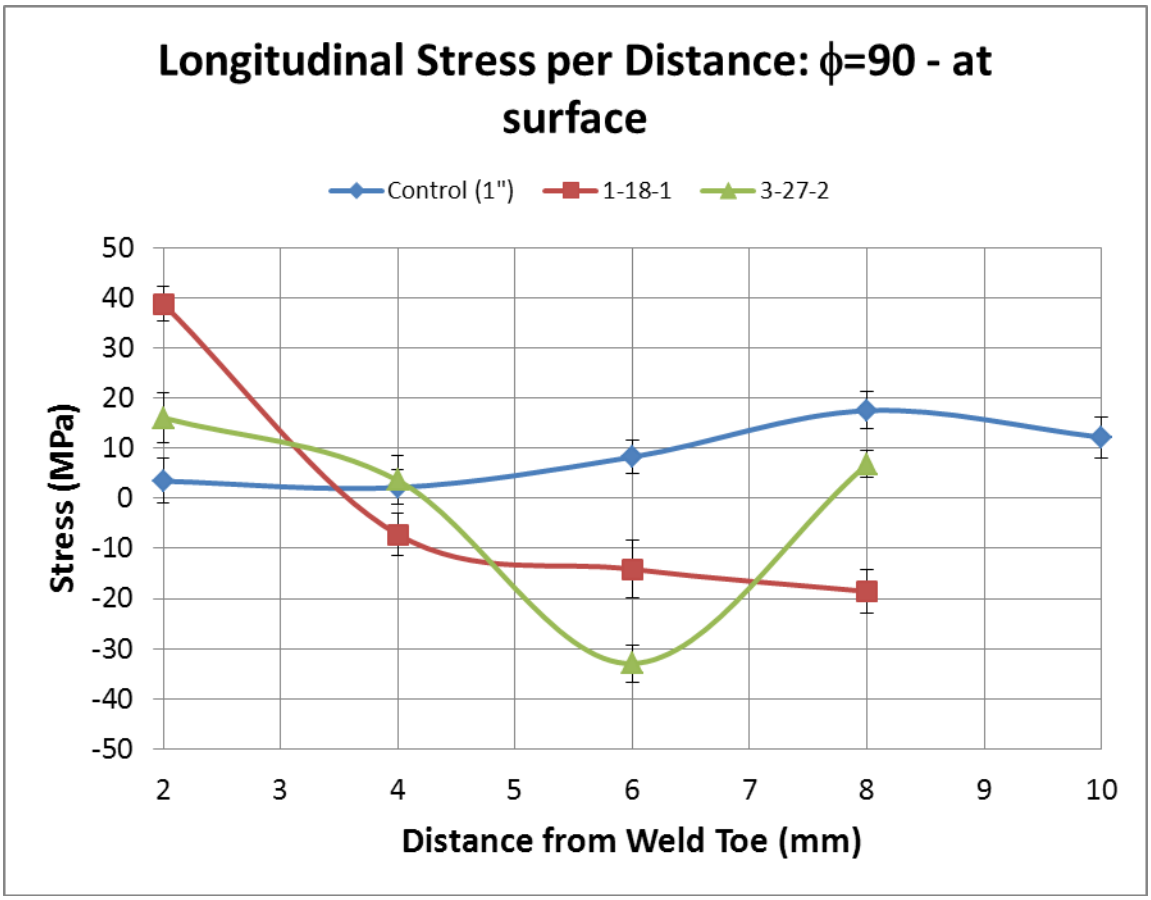

Figure 39. Longitudinal residual stresses as a function of distance from the weld toe in the 1-18-1 and 3-27-2 specimens at the surface.

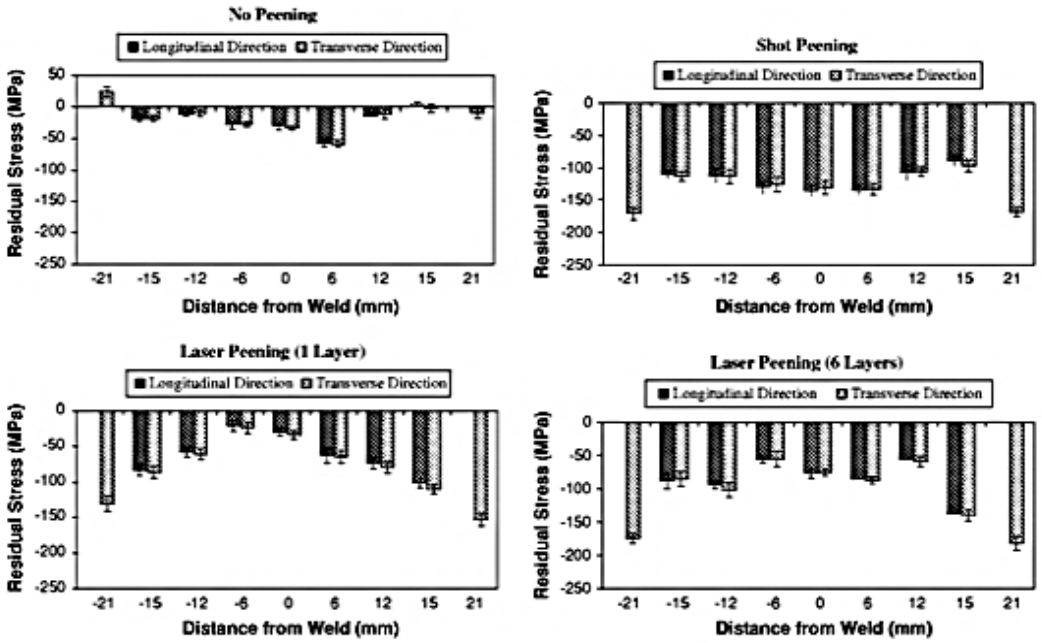

Figure 40. Residual stresses for comparing no peening to shot peening and to laser peening in both the transverse and longitudinal directions from the weld centerline at the surface.(From [32])

The residual stresses as a function of depth of specimens 1-18-1 and 3-27-2 showed that laser peening does impose a compressive residual stress (Figure 41 to Figure 44). Except at the 6mm test point for the longitudinal direction, the 1-18-1 consistently had a more compressive residual stress than the 3-27-2. At this point it is not clear as to why the lighter peening had a more compressive residual stress. In both laser peened specimens, there does appear to a stress gradient forming in the out-of-plane direction (z-direction), which would imply that a plane-stress assumption may not be appropriate and a full stress tensor analysis should be conducted.

Measurements of the residual plastic strain may indicate the source of the difference in stress profile between the two peening conditions. A measurement of the FWHM of the diffraction peak was made as a function of position after laser peening. An increase in FWHM indicated more residual plastic strain. Figure 45 clearly shows that the FWHM values for the 3-27-2 specimen are greater than the control and the 1-18-1 specimen meaning that it has received more plastic deformation that the other two

conditions; and therefore, should have more compressive residual stresses. This trend is clear for the transverse orientation, but for the longitudinal orientation, the FWHM profile actually crosses for the 1-18-1 and 3-27-2 laser peening conditions.

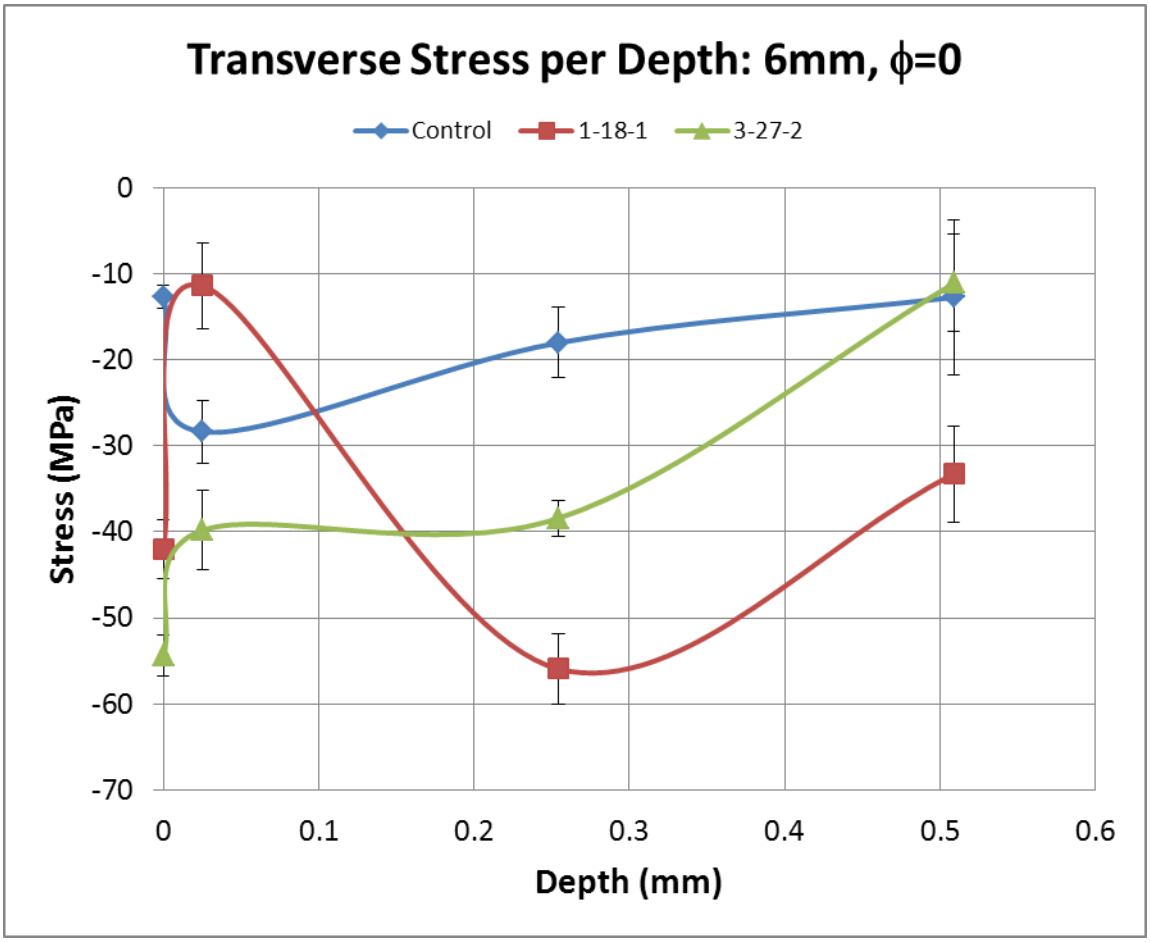

Figure 41. Transverse residual stresses as a function of depth in the 1-18-1 and 3-27-2 specimens at the 6mm test point.

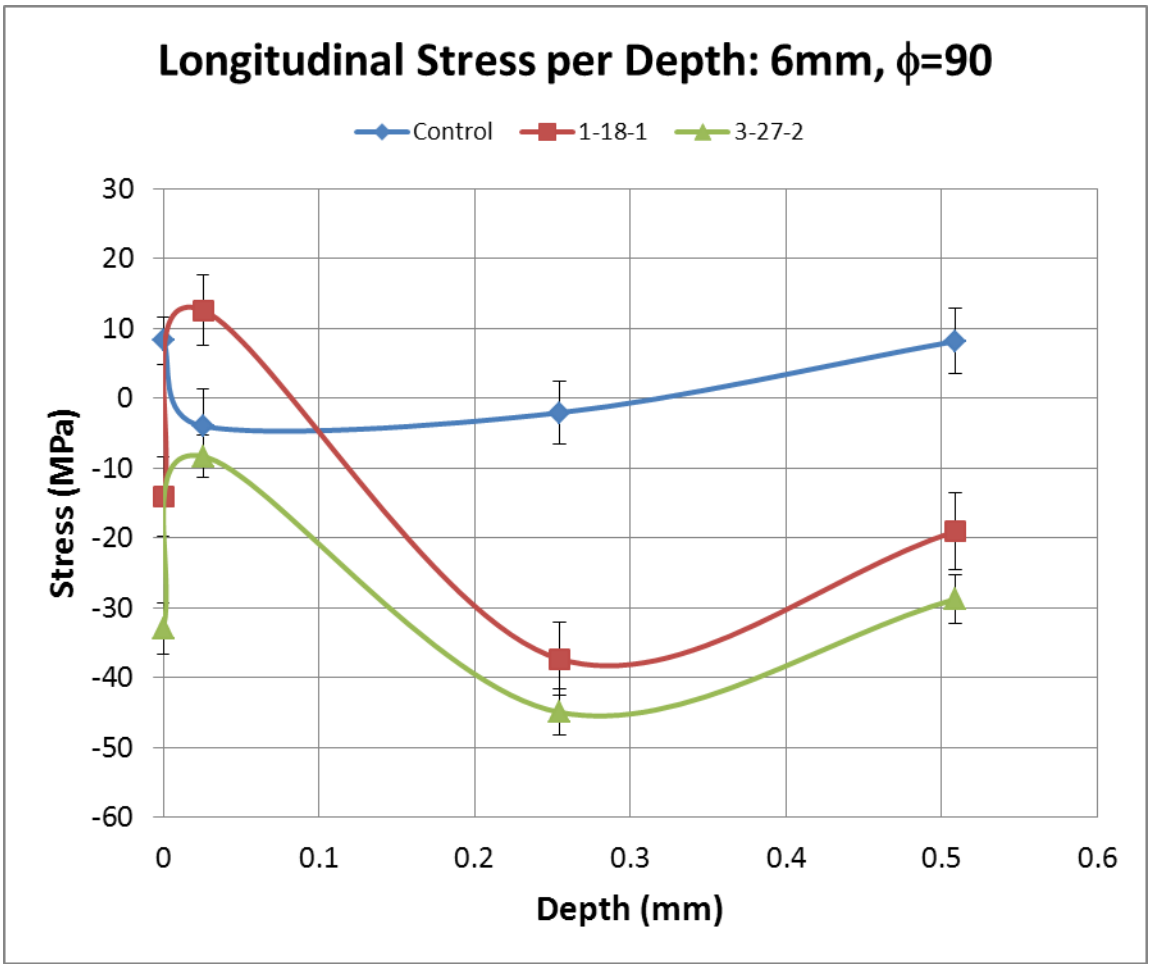

Figure 42. Longitudinal residual stresses as a function of depth in the 1-18-1 and 3-27-2 specimens at the 6mm test point.

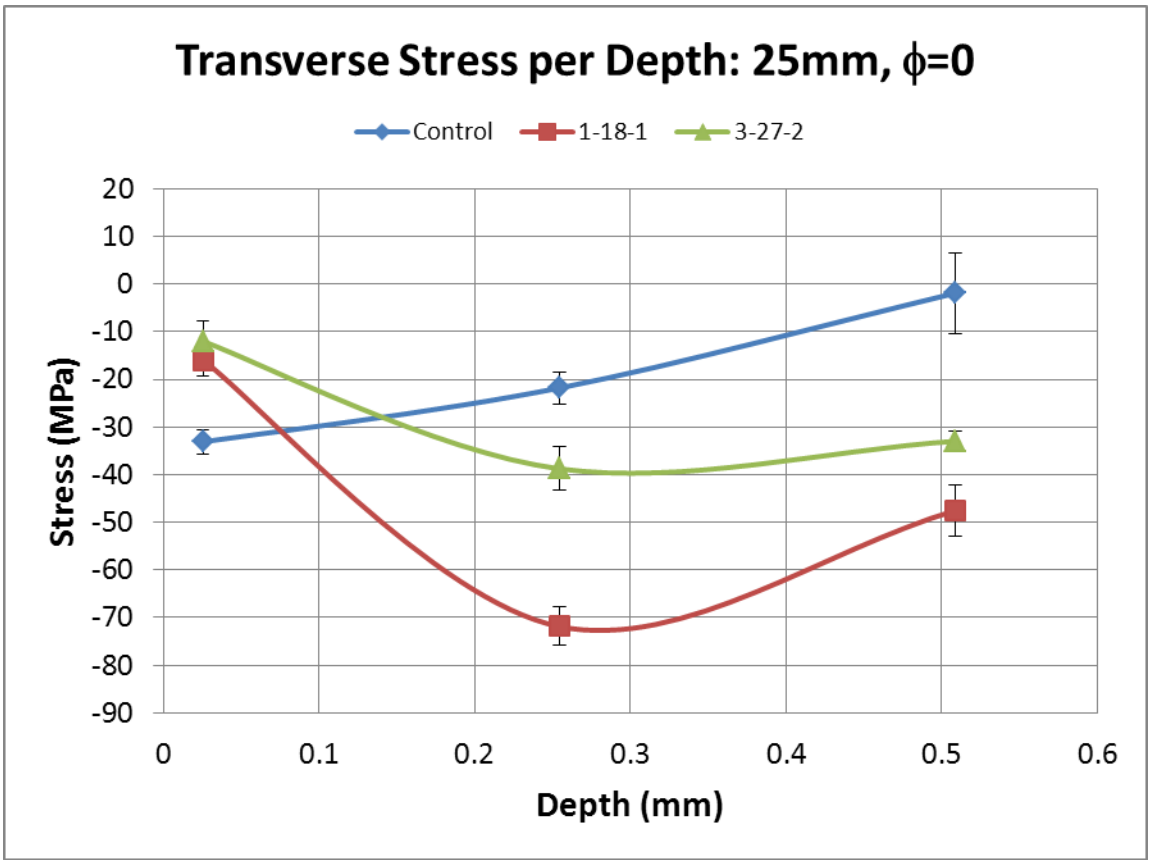

Figure 43. Transverse residual stresses as a function of depth in the 1-18-1 and 3-27-2 specimens at the 25mm test point.

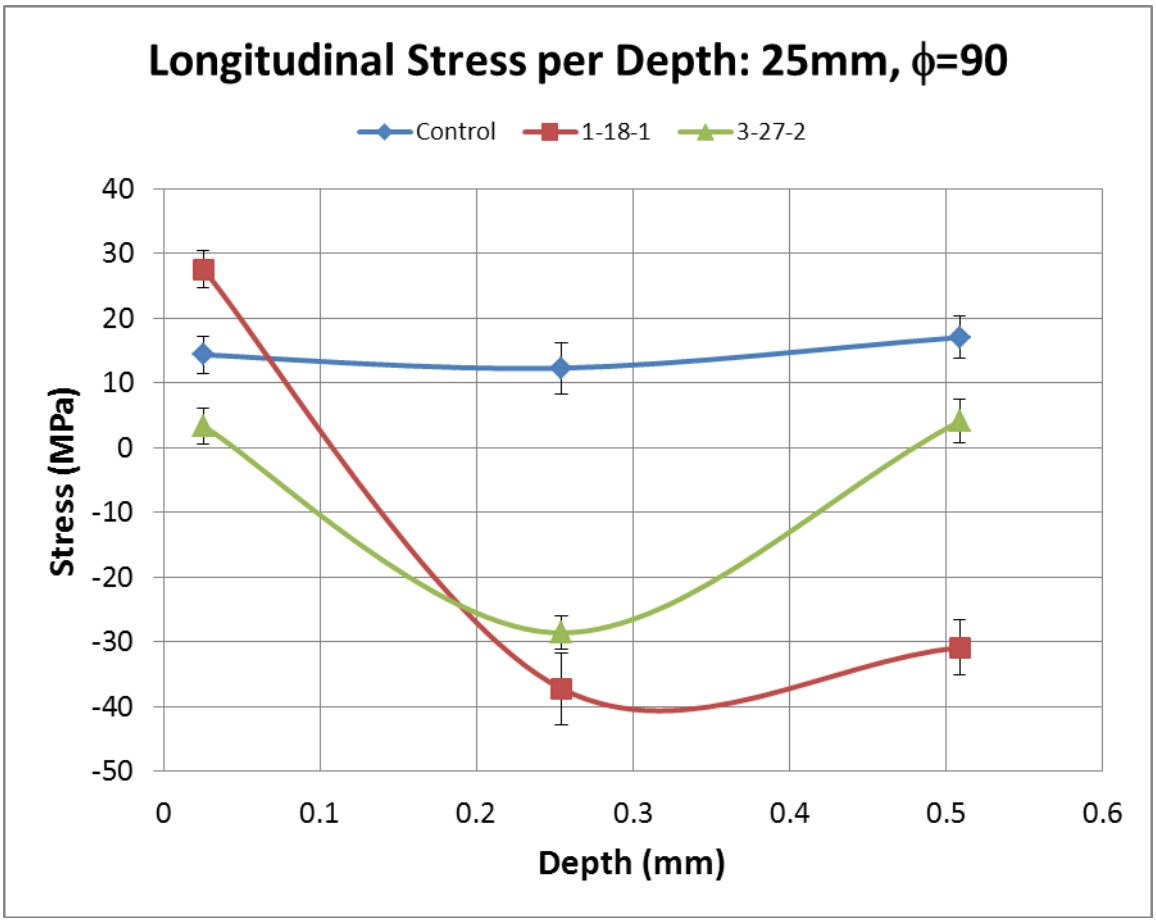

Figure 44. Longitudinal residual stresses as a function of depth in the 1-18-1 and 3-27-2 specimens at the 25mm test point.

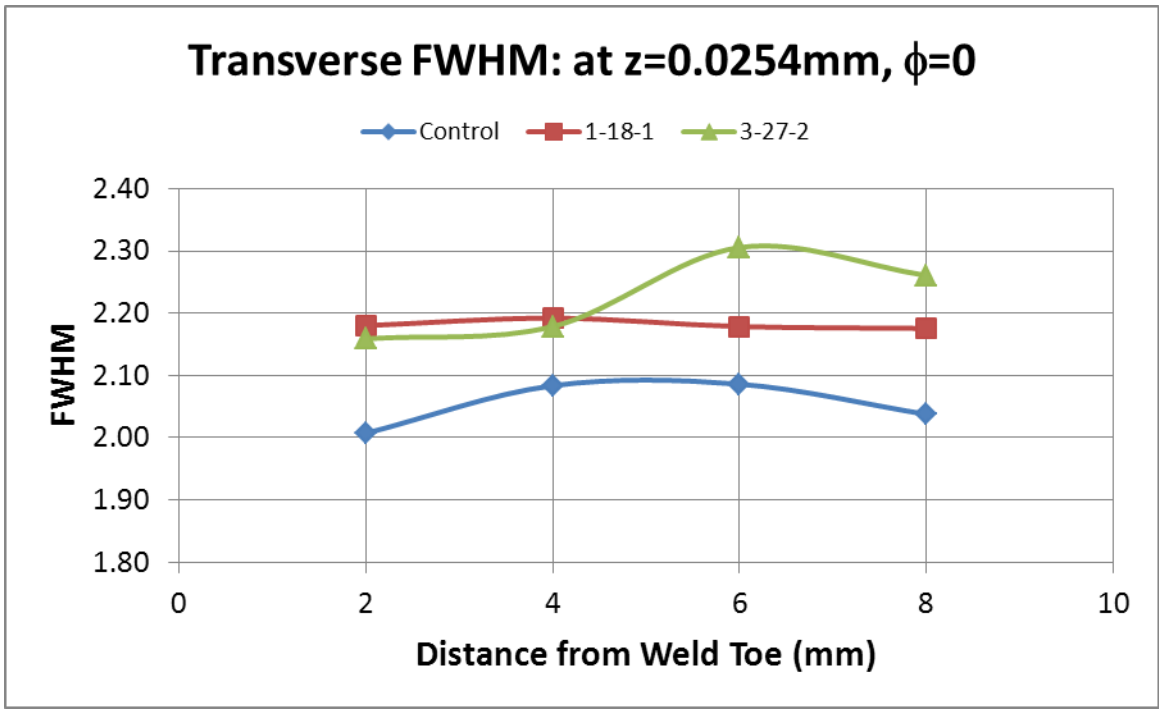

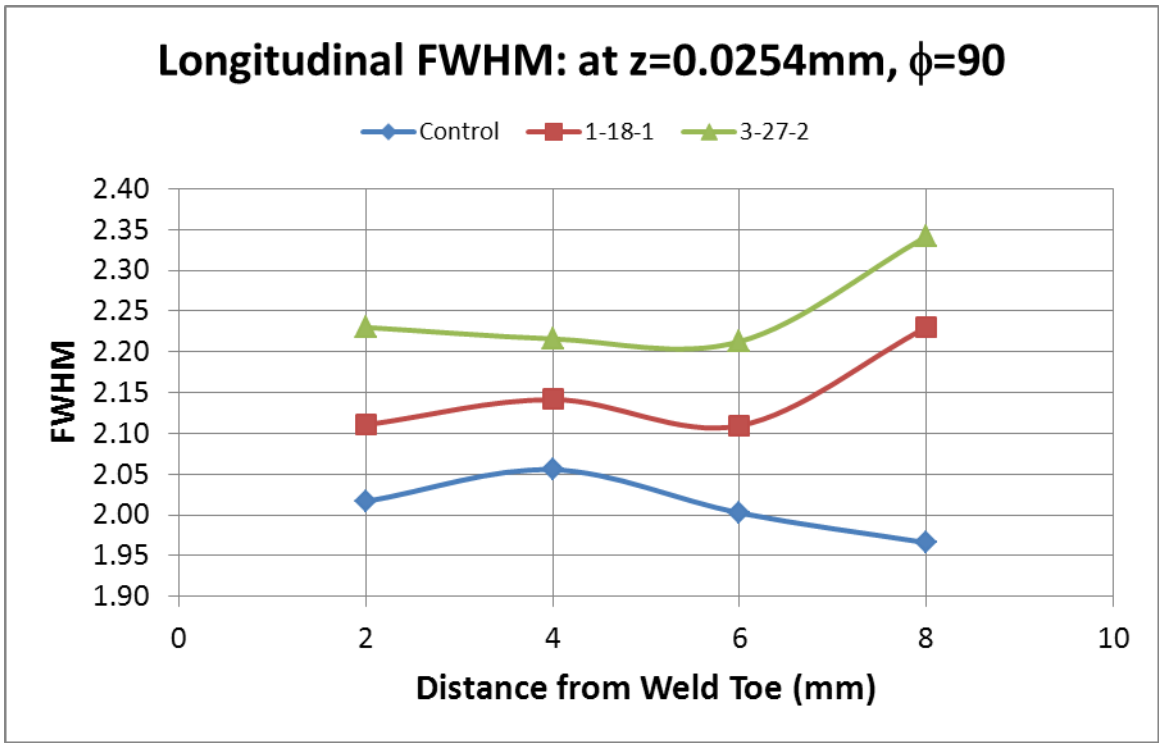

Figure 45. A plot of the FWHM at a depth of 0.0254mm. The upper plot is for the transverse direction at ☐=0 degrees and the lower plot is for the longitudinal direction at ☐=90 degrees.

3. Accounting for Crystallographic Texture

While the general trends of the residual stress profiles are reasonable, some of the confusing points in the data may stem from the difficulty in applying x-ray residual stress techniques to rolled, aluminum material. The material being studied in this thesis is AA5083 with a H116 heat treatment which consists primarily of hot-rolling. This hot-rolling process results in a material with a recrystallization texture. As can be seen in Figure 46, this material does have a weak, but measurable texture.

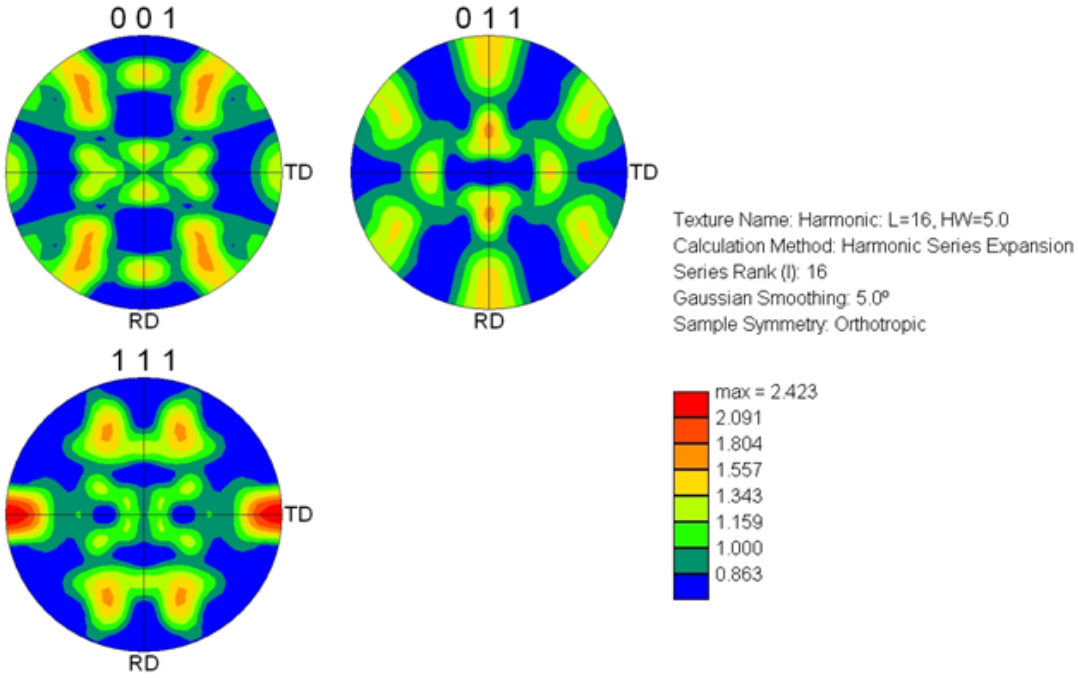

Figure 46. Pole figures generated by electron backscattered diffraction for AA5083 plate material.

Texturing of the material introduces non-linearities into the $\sin^2\psi$ relationship (Figure 18c), making the analysis of the stress from the slope of the line alone difficult, if not impossible. It was observed on many occasions that the d vs. $\sin^2\psi$ plots exhibited oscillatory characteristics. Figure 47 portrays this phenomenon across each of the measured specimens. The "bump" at around a $\sin^2\psi$ value of 0.37 in the plotted data appears to resemble part (c) of Figure 18. If this is the case, then Equation 10 and the whole d vs. $\sin^2\psi$ analysis cannot be reliably used to calculate the strains and the stresses.

There are approaches to deal with the oscillations of the d vs. $\sin^2\psi$ plots.[23–25] One way, proposed by the Dolle-Hauk, is to assume that the oscillations are due to elastic anisotropy.[21] This method addresses the fact that the elastic constants vary with ψ and ϕ tilts in heavily textured materials. Because the Reuss limit describes the stress state that all interactions between the strains and stresses are zero, and because the S'_{33ij} terms are equivalent to the isotropic elastic constants for cubic materials; using the {h00} and {hhh} reflections for diffraction (for cubic materials) should negate oscillations on the d vs. $\sin^2\psi$ plot. This theoretical prediction of linear {h00} and {hhh} reflections is not always satisfied in practice.[21] Based on this argument and the fact that the {400} could not be accessed on the XRD equipment, an attempt to find the stresses was made through the use of tensors. Another appropriate correction is the application of the proper x-ray elastic constants per each ψ and ϕ tilt angle.[23–25] If the material is textured, the x-ray elastic constants, S_1 and $S_2/2$, should be used instead of E and ν where $S_1=\nu/E$ and $S_2/2=(1+\nu)/E$. There were no substantial improvements in the calculated results when using this approach on the current data.[21].

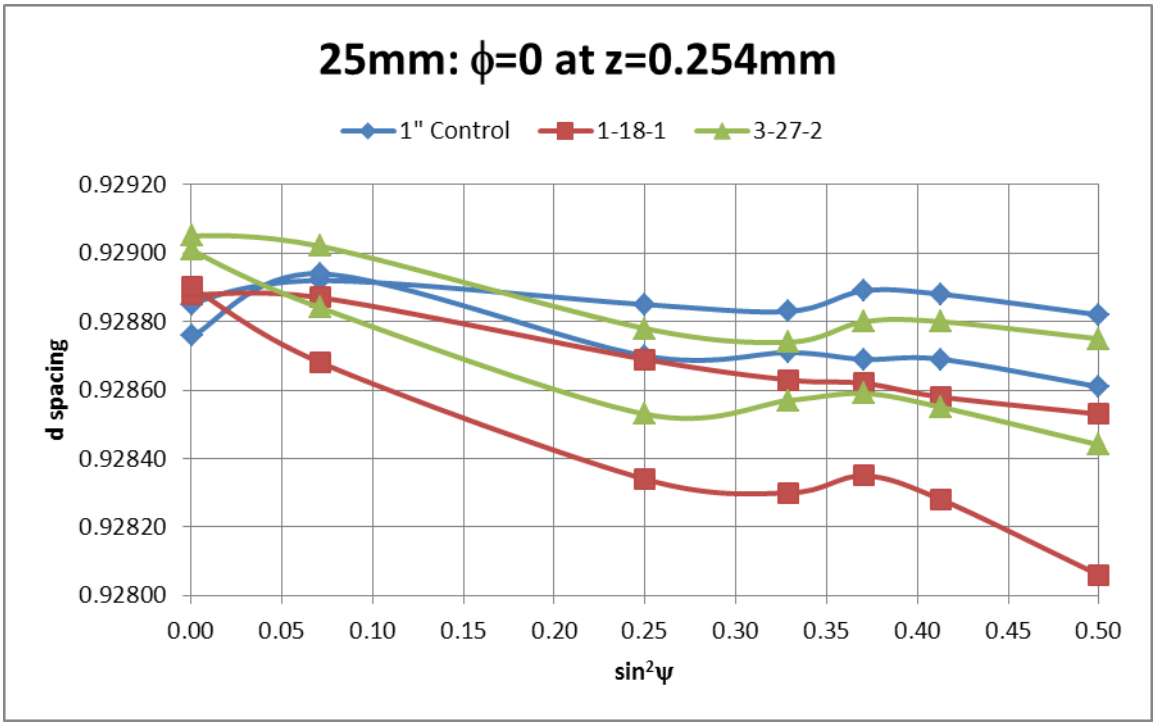

Figure 47. Example of the oscillatory nature of the data across the measured specimens at ☐=0 degrees and at a depth of 0.254mm.

C. RESIDUAL STRESS TENSOR MEASUREMENTS

1. High Stress Standard Tensor Results

Because of the crystallographic texture of the material and the possibility of stress gradients with depth, a full strain tensor measurement and analysis was conducted. A tensor analysis was performed on the high stress standard to verify this procedure. The high stress standard as mentioned above has a bi-axial stress of -232±35MPa; therefore, the intended results should correspond to this known value of stress.

The results in Table 9 display the initial set of tensor data collected and analyzed using a symmetric set of ☐ and ☐ angles. The stresses found in part (a) of Table 9 were implausible because they are many times greater than the yield strength of the material. The stresses in part (b) of Table 9 were collected by selecting an intentionally asymmetric set of ☐ and ☐ angles from the initial data set. The stresses reported in part (c) of Table

9 were collected using a new data set with optimized □ and □ angles and those results were in good approximation to the known stresses of the standard.

There are two main reasons for these extremely large changes in the stress tensor for the high stress standard. The first reason for the unrealistic stresses is because of the large condition number of the coefficient matrix, which is directly controlled by the choice of ψ and ϕ angles during the measurement. The condition number is a matrix property that indicates the bounds of accuracy and stability of a matrix. A "well-conditioned" (i.e. stable) matrix will have a low condition number while an "ill-conditioned" (i.e. unstable) matrix will have a large condition number. Generally a condition number above 100,000 is said to be ill-conditioned, but because of the sensitivities in residual stress analysis a condition number of less than one hundred is desired. The more stable the matrix is, the less error that propagates through each of the matrix calculations.[29,30] It is vital to understand and establish a proper set of ψ and ϕ angles to be used so as to avoid a large condition number of the coefficient matrix. A large condition number, e.g. greater than 100, can result in an unstable matrix inversion, which will result in wild, unpredictable swings in strain values for a small change in measured d spacings. For example, a ψ angle vector of (-45.53, -38.99, -34.53, 34.53, 38.99, 45.53) combined with a ϕ angle vector (-15, -10, -5, 9, 13, 17) results in a condition number of 7,286, in which any small error in measuring ε'_{33} will be magnified and will result in extremely large errors in the strain and stress tensors. The second tensor data set (data set #3) used an optimized ψ angle vector of (-45, -40, -30, 25, 30, 45) and combining it with a new ϕ angle vector of (-65, -35, -15, 5, 45, 55). This new set of angles resulted in a condition number of 21.74, which made the coefficient matrix more well-conditioned.

The second reason for the dramatic changes in the strain and stress tensors can be attributed to the value and source of d_0 (the unstressed lattice spacing). When calculating the stresses based on the full tensor approach, an absolute knowledge of d_0 is required.[19,21] The d_0 value that was measured and used in the d vs. $\sin^2\psi$ technique cannot be used for the determination of the ε'_{33} terms in Equation 10 for the tensor

analysis. The difference between part (b) and part (c) of Table 9 shows the extent of how the d_0 value can significantly change the make-up of the stress tensor. Part (b) of Table 9 uses the d vs. $\sin^2\psi$ technique measured d_0 value whereas part (c) uses a d_0 calculated from Equation 20. The $d_{\psi\phi}$ term is a measured d spacing (in this case at ψ=0 and ϕ=0 degrees, and is 0.9290492angstroms), S_{12} and S_{11} are elements of the compliance matrix and are based off of material constants (in this case S_{11}=1.41e-11Pa^{-1} and S_{12}=-4.64e-12Pa^{-1}), and σ_{11}, σ_{22}, and σ_{33} are the components of the stress tensor (in this case σ_{33}=0MPa because of the assumption of plane-stress and σ_{11}=σ_{22}=-232MPa from the known bi-axial stress of the high stress standard). Based off of these assumptions and rough calculation the d_0 value in part (c) of Table 9 becomes 0.9270536angstroms. It produces a reasonable, bi-axial stress tensor that is relative close to the given stress range of high stress standard, when adjusting the stress tensor to a zero out-of-plane stress condition, as opposed to using a d_0 value of 0.9290492angstroms, as in part (b) of Table 9, which calculates a non-bi-axial stress tensor.

$$d_0 = \frac{d_{\psi\phi}}{\left(S_{12}\sigma_{11} + S_{12}\sigma_{22} + S_{11}\sigma_{33} + 1\right)} \tag{20}$$

This same approach cannot be applied for the experimental, welded and laser-peened specimens, because the stresses are unknown. It is unlikely that the experimental results will have a purely bi-axial stress arrangement; therefore, a powder diffraction measurement of the fillings from the AA5083 material in its stress-free condition will need to be made and analyzed in order to determine the d_0 value to be used for further analysis of the stress tensor calculations of residual stresses in the specimens. It should be noted that the data from the tensor measurement when put through a d vs. $\sin^2\psi$ analysis produced stress values that were in good agreement with previous d vs. $\sin^2\psi$ results at ϕ=0 degrees. Those results actually fell close to the margin of error of the measured stress using the d vs. $\sin^2\psi$ technique.

For example in data set four, the average of the six measured high stress standard values from Table 8 was -247.2±3.7MPa and the stress calculated from the linear least squares slope of the measured tensor data was -241.7MPa. Both of these stresses correspond to the known value of the high stress standard.

(a)

Angles (Degrees)			Tensor Strains		Tensor Stresses (MPa)
□	□				
-45.53	-15	□□□	1.1933E-02	□□□	-2180.85
-38.99	-10	□□□	-6.0636E-02	□□□	-6060.43
-34.53	-5	□□□	-5.6212E-03	□□□	-3119.30
34.53	9	□□□	-1.0735E-02	□□□	-286.94
38.99	13	□□□	7.7914E-04	□□□	20.83
45.53	17	□□□	1.3640E-04	□□□	3.65

Condition Number: 7286 d_0 (angstroms): 0.9290492

(b)

Angles (Degrees)			Tensor Strains		Tensor Stresses (MPa)
□	□				
-45.53	-15	□□□	-2.2695E-03	□□□	-188.85
-38.99	-10	□□□	7.4532E-04	□□□	-27.67
-6.02	-5	□□□	2.2297E-04	□□□	-55.60
14.80	9	□□□	-5.4873E-03	□□□	-146.68
25.04	13	□□□	6.2219E-04	□□□	16.63
45.53	17	□□□	-9.5048E-04	□□□	-25.41

Condition Number: 166 d_0 (angstroms): 0.9290492

(c)

Angles (Degrees)			Tensor Strains		Tensor Stresses (MPa)
□	□				
-45	-65	□□□	-1.6297E-03	□□□	-169.39
-40	-35	□□□	-1.8699E-03	□□□	-182.23
-30	-15	□□□	1.9141E-03	□□□	20.06
25	5	□□□	-1.8586E-04	□□□	-4.97
30	45	□□□	2.6663E-04	□□□	7.13
45	55	□□□	6.5767E-05	□□□	1.76

Condition Number: 21.74 d_0 (angstroms): 0.9270536

Table 9. Strain and stress tensor results for the high stress standard where (a) has an extremely high condition number resulting in implausible stresses, (b) has a much better (i.e. lower) condition number, but a non bi-axial stress, and (c) has an even lower condition number and a revised d_0 value resulting in a more believable bi-axial stress.

2. Control and Laser Peened Tensor Results

There was no consistency in the tensor results for the control and laser peened specimens. The lowering the condition number of the coefficient matrix did seem to help, but not knowing the true d_0 value for the AA5083 material made the results unreliable. For all but one measurement (3-27-2 at the 25mm test point at z=0.508mm), the new set of □ and □ angles produced a full compressive stress tensor. The out-of-plane stress was equal to about 0.5–0.75 the in-plane stresses, which confirms that a bi-axial assumption is invalid. There was no correlation between the in-plane stresses for different data sets, but what was remarkable was that almost all measurements showed a very low amount of out-of-plane shear.

The stress tensor in Table 10 is reasonably close to the measured stresses using the d vs. $\sin^2\psi$ technique. Based on the specimen orientation (the x-axis, parallel to the weld centerline, is in the same direction as σ_{22}, and the y-axis, perpendicular to the weld centerline, is in the same direction as σ_{11}), the reported stress for σ_{11} from the d vs. $\sin^2\psi$ results is -55.95±4.10MPa and the accompanying tensor stress is -65.83MPa while the stress for σ_{22} from the d vs. $\sin^2\psi$ results is -37.33±5.26MPa and the accompanying tensor stress is -56.04MPa. Both of these pairings are in good standing with one another. Upon conducting a Mohr's circle analysis, the resulting θ value to rotate the stress element to the principle axis was about 46 degrees. This angle of rotation indicates that the measured stress tensor is at a max shear orientation with respect to the axes of the welded plate, which makes sense from the standpoint that the material is plastically deforming from the laser peening. Again lower condition numbers do help the data seem more reasonable, but without a true d_0 value the data is uncertain.

Angles (Degrees)			Tensor Strains		Tensor Stresses (MPa)
□	□				
-45	-65	□□□	-5.5970E-04	□□□	-65.83
-40	-35	□□□	-3.7447E-04	□□□	-56.04
-30	-15	□□□	2.2756E-04	□□□	-24.22
25	5	□□□	-2.7545E-05	□□□	-0.73
30	45	□□□	-1.2342E-04	□□□	-3.26
45	55	□□□	-2.0838E-04	□□□	-5.51
Condition Number:		21.74		d_0 (angstroms):	0.9289142

Table 10. Strain and stress tensor results for 1-18-1 at 6mm test point z=0.254mm.

D. FUTURE WORK

This master's thesis represents initial efforts on using x-ray diffraction to measure residual stresses in welded and laser peened aluminum. While these initial results have yielded important information about the residual stresses in these materials, the approach can be improved to increase the accuracy of the measurements.

A fuller accounting of the crystallographic texture in the material must be made. One way of addressing this complication is by utilizing the {h00} or {hhh} reflections for the x-ray diffraction. This change will perhaps eliminate the oscillatory nature of the strain measurements when analyzed by the d vs. $\sin^2\psi$ method. This modification can be done by utilizing a different type of radiation, for instance Cr-Kα. Cr-Kα will allow access to the lower-order reflections at higher Bragg angles, e.g. the {222} reflection at a 2θ angle of 157 degrees. In addition, the {222} reflection has a higher fundamental intensity compared with intensities of the {331} and {420} reflections, resulting in better signal to noise level in the 2θ.

Another issue that needs to be addressed in order to gather better data will be to have better control of the mounting or the specimens in the XRD. More care needs to be taken to deal with machine errors just from sample orientation. There are instrumental

errors from the alignment of the specimen in the XRD and from beam divergence if the specimen is tilted. A repeatable approach will need to be developed to assure the proper focal distance between the specimen and the XRD for each data collection run.

Future work should be focused on obtaining a true d_0 value for use in the full tensor calculations. For both the d vs. $\sin^2\square$ technique and the tensor calculations, a true d_0 value will greatly enhance the accuracy of the measured strains and calculated stresses. When a crude estimation of d_0 for the high stress standard was substituted in place of the d_0 found through the d vs. $\sin^2\square$ technique, the results became more realistic and closer to the expected range of stress values for the high stress standard. A more precise measurement of the d_0 value will give better results of both the high stress standard and specimen analysis. It was also assumed that the residual stress was bi-axial, but upon further analysis a tri-axial approach might give better insight to the stress distribution in the test specimens.

Finally, an extension of this work can be applied to looking at residual stresses onboard ships. A portable XRD unit has the potential to measure and evaluate the amount of residual stress in welds in high stress concentration areas to determine the probability of crack nucleation and potential propagation. Results from this type of residual stress investigation can be fed back into finite element models to better improve the predicted stress loadings and potential failure scenarios.

IV. CONCLUSIONS

The objectives of this master's thesis were to use XRD measurement techniques to determine the amount of compressive residual stress that laser peening can impose on metal-inert-gas (MIG) welded aluminum alloy 5083. Both a d vs. $\sin^2\square$ technique and a full tensor analysis were carried out on XRD data from three sets of specimens: 1) calibration standards, for studying the technique and calibration, 2) an as-welded specimen, which served as a control baseline, and 3) laser peened specimens, which were evaluated for the amount of imposed compressive residual stress. The laser peened specimens used two different laser peening conditions that altered the laser power density, pulse duration, and number of layers.

From XRD residual stress measurements showed that laser peening does impose compressive residual stresses at the surface and to varying depths in AA5083. The residual stresses at the surface of the laser peened specimens were two to three times more compressive than that of the control specimen in both the longitudinal and transverse directions. The residual stresses as a function of depth in the laser peened specimens were also considerably more compressive than the control; however, the analysis of the data by the d vs. $\sin^2\square$ technique revealed non-linearities and a full-tensor analysis was conducted. These non-linearities arose from the anisotropy of the plate material and the weld geometry.

A full-tensor analysis was conducted to address the texturing of the material, as it was a rolled material, and the stress gradients in the out-of-plane direction. Critical parameters for successful tensor measurements were identified, including the susceptibility of the analysis to numeric instability and the importance of an independent measurement of a strain-free lattice parameter, d_0. Some encouraging results from a highly stressed, aluminum standard demonstrate that the full tensor approach can produce tri-axial, full-tensor stress measurements.

THIS PAGE INTENTIONALLY LEFT BLANK

LIST OF REFERENCES

[1] H. R. Mattern, "Laser Peening For Mitigation Of Stress Corrosion Cracking At Welds In Marine Aluminum," M.S. thesis, Dept. Mech and Aero. Eng., Naval Postgraduate School, Monterey, CA, 2011.

[2] R. Schwarting, G. Ebel, and T. J. Dorsch, "Manufacturing Techniques and Process Challenges with CG47 Class Ship Aluminum Superstructures Modernization and Repairs," *Fleet Maintenance & Modernization Symposium 2011: Assessing current & Future Maintenance Strategies*, San Diego, CA, 2011.

[3] I. N. A. Oguocha, O. J. Adigun, and S. Yannacopoulos, "Effect of sensitization heat treatment on properties of Al-Mg alloy AA5083-H116," *Journal Of Materials Science*, 43 (2008) 4208.

[4] H. Bushfield and M. Cruder, "Sensitized Marine Aluminum Plate & ASTM Standard Specification B928-an Update," in *SNAME Section Meeting*. 2006.

[5] C. P. Cavas, "Cracks Continue to Plague U.S. Cruisers," in *Defense News*2010. p. 4.

[6] W. D. Jr. Callister, *Materials Science and Engineering: an Introduction*2007, John Wiley and Sons, Inc.: York, PA.

[7] N. E. Dowling, *Mechanical Behavior of Materials Engineering Methods for Deformation, Fracture, and Fatigue*2007, Pearson Education, Inc.: Upper Saddle River, New Jersey.

[8] S. Ganguly, V. Stelmukh, et al., "Analysis of residual stress in metal-inert-gas-welded Al-2024 using neutron and synchrotron X-ray diffraction," *Materials Science and Engineering*, A 491 (2008) 248.

[9] S. Kou, *Welding Metallurgy*2003, John Wiley & Sons, Inc.: Hoboken, New Jersey.

[10] M. N. James, D. G. Hughes, et al., "Residual stress and strain in MIG butt welds in 5083-H321 aluminum: As-welded and fatigue cycled," *International Journal of Fatigue*, 31 (2009) 28.

[11] S. Benedictus-deVries, A. Bakker, et al., "Fatigue cracked initiation behavior of welded AA5083 in a seawater environment," *Journal of Engineering Materials and Technology*, 126 (2004) 199.

[12] C. S. Montross, T. Wei, et al., "Laser shock processing and its effects on microstructure and properties of metal alloys: a review," *International Journal of Fatigue*, 24 (2002) 1021.

[13] X. An, C. A. Rodopoulos, et al., "Study of the surface nanocrystallization induced by the Esonix ultrasonic impact treatment on the near-surface of 2024-T351 aluminum alloy," *Journal of Materials Engineering and Performance*, 15(3) (2006) 355.

[14] M. Liao, W.R. Chen, and N. C. Bellinger, "Effects of ultrasonic impact treatment on fatigue behavior of naturally exfoliated aluminum alloys," *International Journal of Fatigue*, 30 (2008) 717.

[15] M. R. Hill, A. T. DeWald, et al., "Measurement of laser peening residual stresses," *Materials Science and Technology*, 21(1) (2005) 3.

[16] S. A. Matrinez, S. Sathish, et al., "Residual stress distribution on surface-treated Ti-6Al-4V by x-ray diffraction," *Society for Experimental Mechanics*, 43(2) (2003) 141.

[17] O. Hatamleh, "A comprehensive investigation on the effects of laser and shot peening on fatigue crack growth in friction stir welded AA 2195 joints," *International Journal of Fatigue*, 31 (2009) 974.

[18] K. N. Tran, M. R. Hill, and L. A. Hackel, "Laser shock peening improves fatigue life of lightweight alloys," *Welding Journal*, 85 (2006) 28.

[19] P. S. Prevey, "X-ray Diffraction Residual Stress Techniques," Metals Handbook, 9th Edition, Vol. 10, American Society for Metals, Metals Park, OH, 1986, 380.

[20] B. D. Cullity, *Elements of X-ray Diffraction*1978, Addison-Wesley Publishing Company, Inc.: Reading, Massachusetts.

[21] I. C. Noyan and J. B. Cohen, *Residual Stress Measurement by Diffraction and Interpretation*1987, Springer-Verlag New York Inc.: Germany.

[22] X. J. Xue, K. J. Kozaczek, et al., "Estimating residual stress tensor in aluminum and copper thin films and interconnects," *Advances in X-ray Analysis*, 42 (2000) 612.

[23] H. Dolle and J. B. Cohen, "Evaluation of (residual) stresses in textured cubic metals," *Metallurgical Transactions A*, 11A (1980) 831.

[24] C. M. Brakman and P. Penning, "Non-linear diffraction strain vs $\sin^2\square$ phenomena in specimens exhibiting rolling-type texture," *Acta Crystallographica*, A44 (1988) 163.

[25] H. Dolle, "The influence of multiaxial stress states, stress gradients and elastic anisotropy on the evaluation of (residual) stresses by x-rays," *Journal of Applied Crystallographica*, 12 (1979) 489.

[26] Y. Nakayama, T. Takaai, and S. Kimura, "Evaluation of surface residual stresses in cold-rolled 5083 aluminum alloy by x-ray method," *Materials Transactions*, 34(6) (1993) 496.

[27] P. Barsanescu and P. Carlescu, "Residual Stress Measurement by the Hole-Drilling Strain-Gage Method: Influence of Hole Eccentricity," Technical University, Iasi, Romania, 2007.

[28] Standard Test Method for Determining Residual Stresses by the Hole-Drilling Strain-Gage Method, ASTM E837-08e1, 2008.

[29] S. J. Leon, *Linear Algebra with Applications*2010, Pearson Education, Inc.: Upper Saddle River, New Jersey.

[30] L. N. Trefethen and D. Bau III, *Numerical Linear Algebra*1997, Society for Industrial and Applied Mathematics: Philadelphia, PA.

[31] M. A. Meyers and K. K. Chawla, *Mechanical Behavior of Materials*2009, Cambridge University Press: Cambridge, United Kingdom.

[32] O. Hatamleh, P. M. Singh, and H. Garmestani, "Stress Corrosion Behavior of Peened friction stir welded 2195 aluminum alloy joints," *Journal of Materials Engineering and Performance*, 18(A) (2009) 406.

THIS PAGE INTENTIONALLY LEFT BLANK

APPENDIX

Positive ☐ Angles			
Detector 1		Detector 2	
☐	☐	☐	☐
0	-15.5	0	15.5
1	-14.5	1	16.5
2	-13.5	2	17.5
3	-12.5	3	18.5
4	-11.5	4	19.5
5	-10.5	5	20.5
6	-9.5	6	21.5
7	-8.5	7	22.5
8	-7.5	8	23.5
9	-6.5	9	24.5
10	-5.5	10	25.5
11	-4.5	11	26.5
12	-3.5	12	27.5
13	-2.5	13	28.5
14	-1.5	14	29.5
15	-0.5	15	30.5
16	0.5	16	31.5
17	1.5	17	32.5
18	2.5	18	33.5
19	3.5	19	34.5
20	4.5	20	35.5
21	5.5	21	36.5
22	6.5	22	37.5

Negative ☐ Angles			
Detector 1		Detector 2	
☐	☐	☐	☐
0	-15.5	0	15.5
-1	-16.5	-1	14.5
-2	-17.5	-2	13.5
-3	-18.5	-3	12.5
-4	-19.5	-4	11.5
-5	-20.5	-5	10.5
-6	-21.5	-6	9.5
-7	-22.5	-7	8.5
-8	-23.5	-8	7.5
-9	-24.5	-9	6.5
-10	-25.5	-10	5.5
-11	-26.5	-11	4.5
-12	-27.5	-12	3.5
-13	-28.5	-13	2.5
-14	-29.5	-14	1.5
-15	-30.5	-15	0.5
-16	-31.5	-16	-0.5
-17	-32.5	-17	-1.5
-18	-33.5	-18	-2.5
-19	-34.5	-19	-3.5
-20	-35.5	-20	-4.5
-21	-36.5	-21	-5.5
-22	-37.5	-22	-6.5

Positive ☐ Angles			
Detector 1		Detector 2	
23	7.5	23	38.5
24	8.5	24	39.5
25	9.5	25	40.5
26	10.5	26	41.5
27	11.5	27	42.5
28	12.5	28	43.5
29	13.5	29	44.5
30	14.5	30	45.5

Negative ☐ Angles			
Detector 1		Detector 2	
-23	-38.5	-23	-7.5
-24	-39.5	-24	-8.5
-25	-40.5	-25	-9.5
-26	-41.5	-26	-10.5
-27	-42.5	-27	-11.5
-28	-43.5	-28	-12.5
-29	-44.5	-29	-13.5
-30	-45.5	-30	-14.5

Table 11. Relationship of ☐ to ☐ angles for detector 1 and detector 2 for the {331} reflection using a cobalt tube.

Detector 1	
☐	☐
-45	-29.5
-40	-24.5
-35	-19.5
-30	-14.5
-25	-9.5
-20	-4.5
-15	0.5
-10	5.5
-5	10.5
0	15.5
5	20.5
10	25.5
15	30.5
20	35.5
25	40.5
30	45.5
35	50.5
40	55.5
45	60.5

Detector 2	
☐	☐
-45	-60.5
-40	-55.5
-35	-50.5
-30	-45.5
-25	-40.5
-20	-35.5
-15	-30.5
-10	-25.5
-5	-20.5
0	-15.5
5	-10.5
10	-5.5
15	-0.5
20	4.5
25	9.5
30	14.5
35	19.5
40	24.5
45	29.5

Table 12. Relationship of ☐ to ☐ angles for detector 1 and detector 2 for the {331} reflection using a cobalt tube.

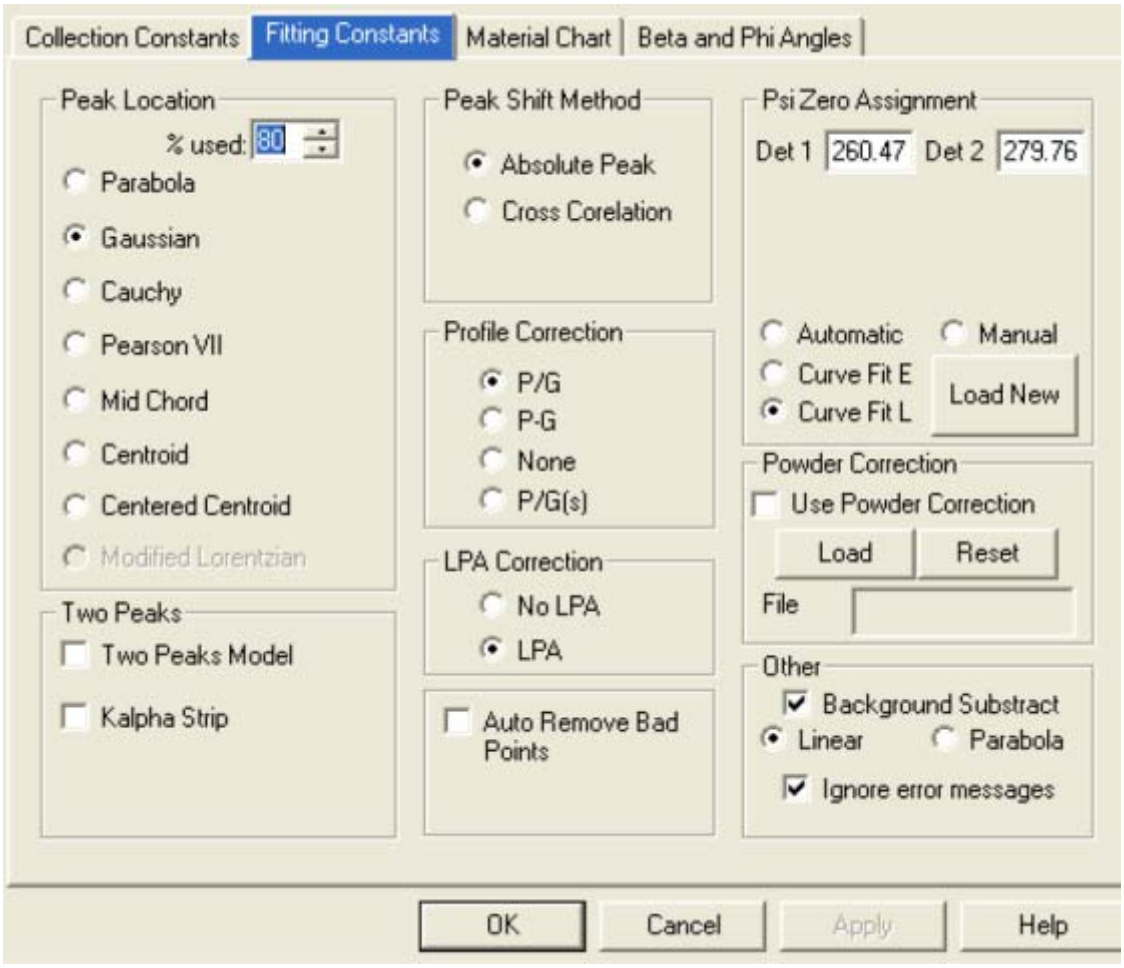

Figure 48. This is an example of the screenshot of the peak fitting constants used for experimental and calibration measurements per this work. Provided by MIC.

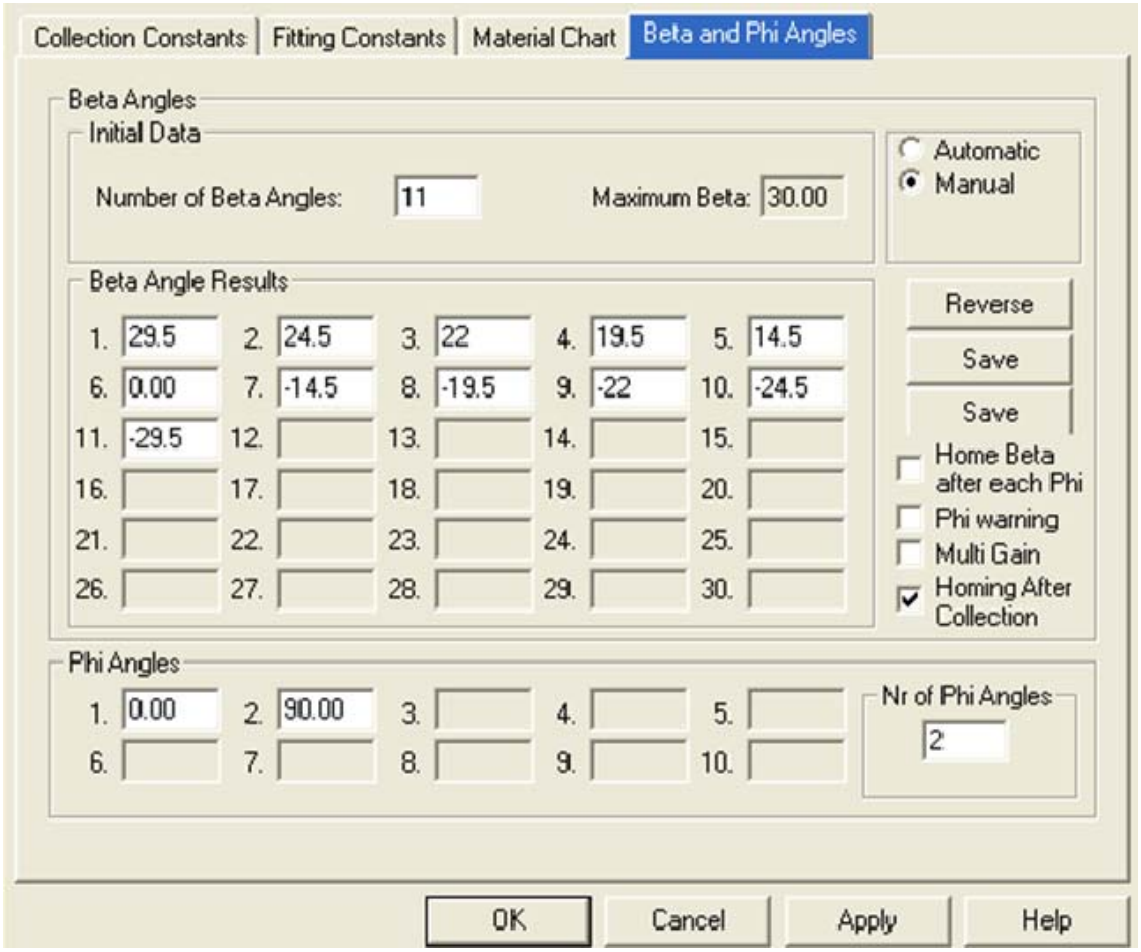

Figure 49. This is an example of a screenshot of the ☐ and ☐ angles used for experimental measurements. Provided by MIC.

	Detector 1	Detector 2
□	□	□
29.00	20.50	37.50
23.96	15.46	32.46
18.61	10.11	27.11
11.80	3.30	20.30
5.19	-3.31	13.69
0.00	-8.50	8.50
-5.19	-13.69	3.31
-11.80	-20.30	-3.30
-18.61	-27.11	-10.11
-23.96	-32.46	-15.46
-29.00	-37.50	-20.50

Table 13. □ and □ angles of detector 1 and detector 2 used for data set one.

	Detector 1	Detector 2
□	□	□
30.00	14.50	45.50
24.13	8.63	39.63
20.00	4.50	35.50
14.00	-1.50	29.50
10.50	-5.00	26.00
0.00	-15.50	15.50
-10.50	-26.00	5.00
-14.50	-29.50	1.50
-20.00	-35.50	-4.50
-24.13	-39.63	-8.63
-30.00	-45.50	-14.50

Table 14. □ and □ angles of detector 1 and detector 2 used for data set two.

Data Set 3	Detector 1	Detector 2
□	□	□
29.50	14.00	45.00
24.50	9.00	40.00
22.00	6.50	37.50
19.50	4.00	35.00
14.50	-1.00	30.00
0.00	-15.50	15.50
-14.50	-30.00	1.00
-19.50	-35.00	-4.00
-22.00	-37.50	-6.50
-24.50	-40.00	-9.00
-29.50	-45.00	-14.00

Data Set 4	Detector 1	Detector 2
□	□	□
29.50	14.00	45.00
24.50	9.00	40.00
19.50	4.00	35.00
14.50	-1.00	30.00
9.50	-6.00	25.00
0.00	-15.50	15.50
-9.50	-25.00	6.00
-15.50	-30.00	1.00
-19.50	-35.00	-4.00
-24.50	-40.00	-9.00
-29.50	-45.00	-14.00

Table 15. □ and □ angles of detector 1 and detector 2 used for data sets three and four.

(a)	Specimens at □=0 and z=surface					
Distance from Weld Toe	Control (1")		1-18-1		3-27-2	
(mm)	(MPa)	(+/-)	(MPa)	(+/-)	(MPa)	(+/-)
2	-18.27	2.86	-0.99	3.31	-22.82	3.52
4	-20.04	2.55	-46.00	2.47	-36.36	3.12
6	-12.73	1.33	-41.97	3.41	-54.39	2.33
8	-7.96	3.68	-38.86	3.22	-23.68	2.18
25						

(b)	Specimens at □=0 and z=0.0254mm					
Distance from Weld Toe	Control (1")		1-18-1		3-27-2	
(mm)	(MPa)	(+/-)	(MPa)	(+/-)	(MPa)	(+/-)
2	-33.11	6.22	13.16	5.43	-3.66	7.44
4	-25.59	5.03	4.91	5.99	-4.19	6.08
6	-28.37	3.67	-11.40	5.04	-39.81	4.63
8	-9.71	3.42	11.84	2.58	4.90	2.84

25	-33.11	2.59	-15.95	3.38	-12.01	4.38

(c)	Specimens at ☐=0 and z=0.254mm					
Distance from Weld Toe	Control (1")		1-18-1		3-27-2	
(mm)	(MPa)	(+/-)	(MPa)	(+/-)	(MPa)	(+/-)
2						
4						
6	-18.01	4.08	-55.95	4.10	-38.41	2.09
8						
25	-21.80	3.40	-71.86	4.03	-38.76	4.61

(d)	Specimens at ☐=0 and z=0.508mm					
Distance from Weld Toe	Control (1")		1-18-1		3-27-2	
(mm)	(MPa)	(+/-)	(MPa)	(+/-)	(MPa)	(+/-)
2						
4						
6	-12.73	8.97	-33.28	5.84	-11.10	5.67
8						
25	-1.88	8.47	-47.52	5.29	-32.94	2.20

Table 16. Results of measured stresses transverse to the weld centerline at ☐=0 degrees for various test locations and at various depths of (a) surface, (b) 0.0254mm, (c) 0.254mm, and (d) 0.508mm.

(a)	Specimens at ☐=90 and z=surface					
Distance from Weld Toe	Control (1")		1-18-1		3-27-2	
(mm)	(MPa)	(+/-)	(MPa)	(+/-)	(MPa)	(+/-)
2	3.42	4.46	38.76	3.47	16.05	4.91
4	2.15	3.46	-7.22	4.25	3.56	4.88
6	8.23	3.36	-14.15	5.70	-32.94	3.69
8	17.48	3.71	-18.57	4.27	6.76	2.71
25						

(b)	Specimens at ☐=90 and z=0.0254mm					
Distance from Weld Toe	Control (1")		1-18-1		3-27-2	
(mm)	(MPa)	(+/-)	(MPa)	(+/-)	(MPa)	(+/-)
2	-6.67	5.45	46.73	3.52	54.62	7.64

4	-0.25	3.79	16.36	4.98	34.57	3.39
6	-3.98	5.23	12.61	5.04	-8.31	2.98
8	12.15	5.05	26.53	5.60	40.35	2.72
25	14.36	2.90	27.56	2.82	3.32	2.57

(c)	Specimens at ☐=90 and z=0.254mm					
Distance from Weld Toe	Control (1")		1-18-1		3-27-2	
(mm)	(MPa)	(+/-)	(MPa)	(+/-)	(MPa)	(+/-)
2						
4						
6	-2.07	4.49	-37.33	5.26	-44.97	3.27
8						
25	12.31	3.95	-37.25	5.59	-28.62	3.86

(d)	Specimens at ☐=90 and z=0.508mm					
Distance from Weld Toe	Control (1")		1-18-1		3-27-2	
(mm)	(MPa)	(+/-)	(MPa)	(+/-)	(MPa)	(+/-)
2						
4						
6	8.19	4.63	-19.04	5.58	-28.75	3.47
8						
25	17.05	3.22	-30.86	4.19	4.13	3.38

Table 17. Results of measured stresses longitudinal to the weld centerline at ☐=90 degrees for various test locations and at various depths of (a) surface, (b) 0.0254mm, (c) 0.254mm, and (d) 0.508mm.

INITIAL DISTRIBUTION LIST

1. Defense Technical Information Center
   Ft. Belvoir, Virginia

2. Dudley Knox Library
   Naval Postgraduate School
   Monterey, California

3. MAE Department Chairman,
   Dr. Knox Millsaps
   Naval Postgraduate School
   Monterey, California

4. Engineering and Technology Curricular Office, Code 34
   Naval Postgraduate School
   Monterey, California

5. Professor Luke Brewer
   Naval Postgraduate School
   Monterey, California

6. Professor Sarath Menon
   Naval Postgraduate School
   Monterey, California

7. Dr. Lloyd Hackel
   Metal Improvement Company